2002

Effect of microstructural stability on the annealing behaviour of deformed aluminium single crystal

Nicole Stanford
University of Wollongong

Effect of Microstructural Stability on the Annealing Behaviour of Deformed Aluminium Single Crystals

A thesis submitted in fulfilment of the requirements for the award of the degree

Doctor of Philosophy

from

UNIVERSITY OF WOLLONGONG

by

Nicole Stanford, BE (Hons)

Department of Materials Engineering

2002

Candidates Certificate

This is to certify that the work presented in this thesis was carried out by the candidate in the laboratories of the Department of Materials Engineering at the University of Wollongong, and has not been submitted to any other university or institution for a higher degree.

.....

Nicole Ellen Stanford

Table of Contents

Acknowledgments

Firstly I would like to thank my supervisor, Prof. Druce Dunne, who gave me a lot of his time, and taught me a great deal. Experimentally, this research project would never have been completed without the help of the technical staff in the Department of Materials Engineering: Mr. Ron Kinell, Mr. Greg Tillman, Mr. Bob de Jong "The Gleeble Man", and Mr. Lee Brunckhorst (AFM and TEM guru). I would specifically like to acknowledge the input of Mr. Nick Mackie, who was a never ending source of information on electron microscopy, and also facilitated months of overnight EBSD experiments which were a vital component of this study. I would also like to thank my co-supervisor, Dr. Michael Ferry, who initiated the project, proof read my drafts, and supplied the single crystals.

I would like to make special thanks to those who supported me most when things went wrong, Lisa Wells, Gaye Kolsky, Bryan Wright and Brett Tarrant. Without the support of these special people I would surely have quit long before submission.

Abstract

High purity aluminium single crystals of the Cube orientation (001)[100], and a 45° rotated Cube orientation, (011)[01 $\bar{1}$], have been deformed in plane strain compression. Deformation was carried out between room temperature and 600°C, over a range of strains, and at strain rates of up to 50 s^{-1}. These deformed crystals were subsequently annealed in a muffle furnace for various times between 200°C and 400°C. The main objective was to compare texture development and structural evolution in the two crystal orientations in response to hot and cold deformation and subsequent annealing.

The room temperature deformation behaviour of the Cube oriented crystals over strains of 0.06 to 1.2 was investigated by slip line analysis using atomic force microscopy (AFM). AFM was used to investigate quantitatively the development of slip lines and deformation bands at strains as low as 0.2. At the higher strains of 0.7 and 1.2 the mechanisms of deformation were analysed crystallographically using electron backscattered diffraction (EBSD), microstructurally using scanning electron microscopy and topographically using AFM. Coupling of these three techniques has demonstrated the irregular and localised nature of deformation at transition bands in deformed Cube oriented crystals.

For both the Cube and rotated Cube orientations, the deformation texture was investigated using EBSD and x-ray diffraction. The Cube orientation was found to increase in microstructural stability at higher deformation temperatures. However, the

rotated Cube orientation was found to become less stable at higher deformation temperatures, a novel observation for aluminium and its dilute alloys.

Hot deformation and annealing of crystals of the $(011)[01\bar{1}]$ orientation produced a uniquely banded recrystallisation microstructure. Regularly spaced recrystallised grains grow within distinct bands confined between parallel regions of recovered subgrains. The subgrains are in fact contained within cylindrical or lath shaped volumes, and these volumes are not random, but are regularly spaced into an array. Even after full recrystallisation, the microstructure retained this banded appearance.

It is proposed that these banded microstructures are caused by periodic nucleation of recrystallisation, resulting from stored energy differentials present in the as-deformed microstructure. On annealing, nucleation of recrystallisation occurs in regularly spaced columns, but grain growth toward adjacent columns is inhibited by impingement with volumes of recovered subgrains, producing the banded microstructures that were observed. The small stored energy difference between the recrystallised grains and the volumes of recovered subgrains is considered to impede the completion of recrystallisation, and to result in the unusual banded microstructures found in hot deformed and annealed $(011)[01\bar{1}]$ crystals.

Deformation temperature was found to have a significant effect on recrystallisation texture. Annealing after cold deformation of the Cube orientation resulted in a random recrystallisation texture at all strains. Cold deformation and annealing of the $(011)[01\bar{1}]$ orientation produced a random texture at low strains, and at higher strains produced a recrystallisation texture lying at the periphery of the deformation texture. In

contrast, annealing after hot deformation produced a recrystallisation texture close to the deformation texture, irrespective of microstructural stability, strain, or crystallographic orientation.

List of Symbols

A	Area
Dc	Cylindrical diameter
E_D	Stored energy of deformation
L	Subgrain diameter
M	Mobility of a grain boundary
M`	Schmid factor
P	Driving pressure for recrystallisation
Q	Activation energy
R	Gas constant
T	Temperature
T_{def}	Deformation Temperature
t, t_0	Time
V	Volume
v	Velocity of a migrating grain boundary
Z	Zener-Hollomon parameter
ε	Strain
γ	Grain boundary energy
σ_f	Flow stress
τ, τ_c	Shear stress
θ	Angular misorientation (degrees)
Φ, φ_1, φ_2	Euler angles

List of Abbreviations

AFM	Atomic force microscopy
bcc	Body centred cubic
CRSS	Critical resolved shear stress
DB	Deformation band
EBSD	Electron backscattered diffraction
ECC	Electron channelling contrast
fcc	Face centred cubic
HAGB	High angle grain boundary
LAGB	Low angle grain boundary
ND	Normal direction
ODF	Orientation distribution function
ppm	Parts per million
RD	Rolling direction
SEM	Scanning electron microscope
SFE	Stacking fault energy
TB	Transition band
TBN	Transition band nucleation
TD	Transverse direction
TEM	Transmission electron microscope
XRD	X-ray diffraction

List of Figures

List of Tables

Part A

Literature Review

1 Plastic Deformation

1.1 Introduction

Plastic deformation is the process by which a material's shape is permanently altered. The microstructural features resulting from plastic deformation such as deformation banding and the development of substructure are of interest here. The mechanisms of slip initiation are also discussed. The current study investigates the deformation and annealing behaviour of high purity aluminium single crystals of known crystallographic orientation, and the literature review is restricted to the behaviour of high stacking fault energy (SFE), face centred cubic (fcc) metals.

1.2 Initiation of Slip

The early stages of deformation in fcc metals occurs by slip on the {111} plane in the <100> direction. The {111} family of planes contains four independent and crystallographically identical planes. Within each of these planes there are three <110> directions, resulting in a total of 12 equivalent slip systems, all of which may take part in the slip process. Slip on these systems is termed "octahedral" or "prismatic" slip due to the shape of the 8 sided figure that is formed by the intersection of the {111} family of planes[1-3]. Under certain conditions, such as high strain and high temperature, slip may be initiated on other systems, so called "non-octahedral" slip, and this is further discussed where relevant.

Of the possible slip systems in an fcc structure, the system that yields first is oriented to have the highest shear stress acting along its slip direction. The shear stress that acts on a plane can be calculated using simple geometry as follows (Fig. 1.1)[1, 3]:

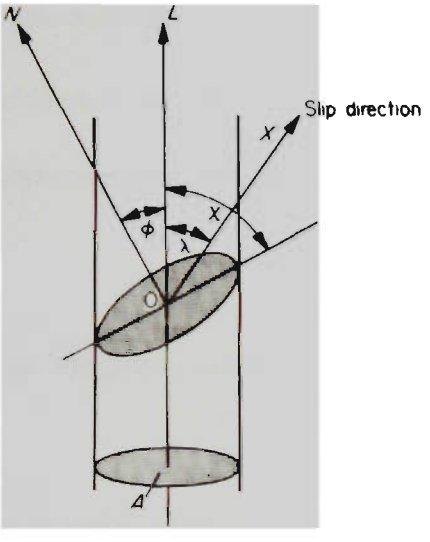

Figure 1.1 Resolved shear stress on a slip system[1].

In tension, a cross sectional area, A, is subject to a tensile load, L, resulting in a tensile stress σ_t. The tensile stress on the slip plane is

$$\frac{L}{A}\sin\chi = \sigma_t \sin\chi \tag{1.1}$$

where the shear stress acting on the slip plane can be resolved in the slip direction to give the *resolved shear stress* which acts on the slip system

$$\tau = \sigma_t \sin\chi.\cos\lambda = \sigma_t \cos\Phi.\cos\lambda \tag{1.2}$$

When the resolved shear stress reaches a critical value, the *critical* resolved shear stress (CRSS), slip will be initiated on the system.

The shear stress on the slip plane is at a maximum when χ and λ are both 45°, and corresponds to ½ σ_t. When the angle that the slip plane makes with the tensile axis is known, $\sin\chi.\cos\lambda$ can be calculated, and this parameter is known as the Schmid factor. Slip is initiated first on the plane with the highest Schmid factor[1-3].

1.3 Lattice Rotations in Single Crystals

Each slip movement is a small shear in the slip direction on the slip plane, and these shears result in a rotation of the crystal with respect to fixed axes such as the tensile axis or rolling direction (Fig. 1.2). Crystal rotations during deformation cause "geometric softening", the crystal rotates to become more favourable to slip as deformation proceeds. This rotation may also cause other slip systems to become favourable, leading to simultaneous slip on multiple slip planes. Crystal rotation in response to slip causes many grains within a polycrystal to become aligned during deformation, producing a preferred orientation or deformation texture[3]. Crystal rotations can be mathematically predicted (as in section 1.5) or may be tracked on a stereographic projection.

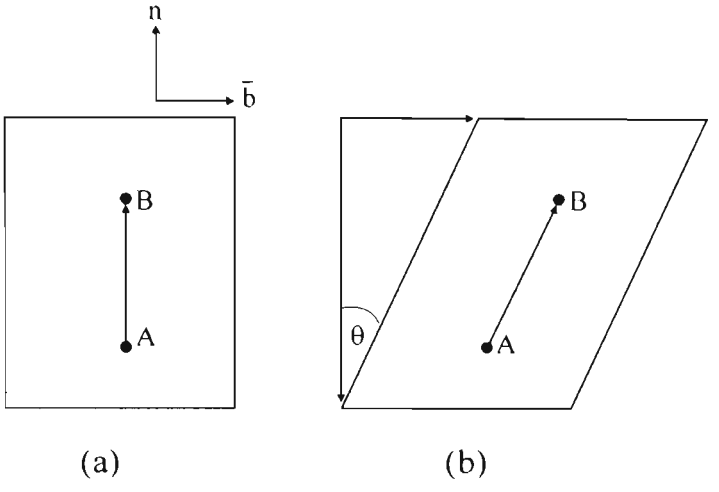

Figure 1.2 Schematic diagram of the effect of single slip on direction AB (a) before slip and (b) after slip. n shows the slip plane normal, b represents the Burgers vector[3].

1.4 Slip on Multiple Systems

In fcc materials, as in most cubic structures, there are multiple slip systems that may operate under an applied load. It is possible for these systems to be oriented such that slip is equally likely to occur on two separate systems. Alternatively, the rotation of a crystal due to single slip may cause the resolved shear stress on two slip planes to become equal. In these instances, slip is able to occur on two planes simultaneously, and this is referred to as duplex slip. When duplex slip occurs, the rotation of the crystal structure is no longer toward the tensile (or away from the compressive) axis. In tension, the crystal will rotate toward the vector sum of the two Burgers vectors of the slipping planes, whilst in compression the crystal will rotate toward the vector sum of the plane normals[2, 3].

Due to the multiple slip systems available in a cubic structure, there are certain loading conditions under which slip may occur on three or more systems simultaneously (during polycrystalline deformation this is usually the case)[2, 3].

To accommodate applied strain in many directions, such as experienced by a single grain constrained by its neighbours in a polycrystalline aggregate, slip must be able to accommodate movement in all directions to prevent fracture, and to ensure ductility[2, 3]. Taylor[4] surmised that to describe any increment of strain, 6 independent components must be defined. Due to constancy of volume, the 6^{th} and final component is determined by the first 5, so deformation of a metal crystal may be completely described by 5 independent components of strain. If each active slip system can be said to contribute a small amount to the total strain in the body, then the summation of these contributions should equal the total strain. Since only 5 independent systems can cause any combination of strains, then only 5 slip systems are required to cause any shape change.

1.5 Theories of Polycrystalline Plasticity

The theories of polycrystalline plasticity predict the active slip systems in a polycrystalline aggregate under an applied strain. These also predict the crystal rotations that occur during deformation, and can be used to predict the deformation textures that develop.

1.5.1 Full Constraints

Commonly referred to as the Taylor theory[4], the full constraints model assumes that the strain undergone by a single grain is identical to the strain of the bulk specimen. The set of slip systems that will operate is predicted by calculating the combination of slip systems that require the least work.

Initially, Taylor analysed the deformation of a single crystal in tension. From the 12 possible slip systems, the virtual work done during slip is:

$$S.s = P.x \tag{1.3}$$

Where S is the shear strength, and s the amount of slip corresponding to extension x from force P. The shear strength for all systems (the CRSS, τ_c) is identical, as is P. Furthermore, for a prescribed extension, x, slip will occur on the plane for which S is a minimum. If work (w) may be defined as force multiplied by distance, then the work done by the system during an increment of shear strain (γ) may be defined by[3] :

$$\delta w = \tau_c \Sigma \delta\gamma \tag{1.4}$$

To determine which combination of 5 slip systems will operate in response to the applied load, the above calculation is repeated for every combination of 5 from the 12 possible slip systems to determine which summation results in the least work or energy dissipation. For each orientation at regular intervals, Taylor determined which systems operate and the crystal rotations resulting from slip after an applied strain of 2.37%. These were plotted, and the extent of each rotation shown in rectangular co-ordinates

(Fig.1.3). The beginning of the arrow indicates the start point, and the arrow head the end orientation. Two arrows radiating from one point indicate that two sets of 5 systems result in an equal likelihood of occurring.

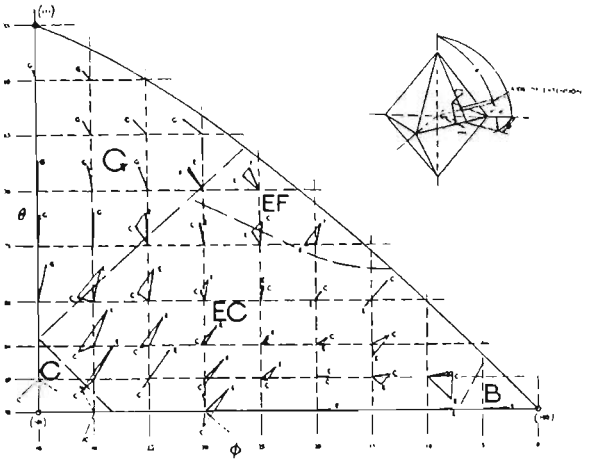

Figure 1.3 Rotation of crystal axes in aggregate during a 2.37% extension[4]

In each region, the effect of the slip system combination on the final rotation can be seen. Section G rotates so that the [111] axis tends to align with the tensile axis. Grains close to the [100] orientation will rotate until a cubic axis is parallel to the specimen axis. Taylor concluded that crystals within an aggregate would rotate toward either the [111] or [100] axis, but not toward [101]. In compression the reverse rotations will occur, with the crystal axis of all grains rotating toward [101].

Bishop and Hill[5, 6] attempted to predict the stress (σ_{ij}) imposed on a crystal by an arbitrary element of strain, $\delta_{ij}\varepsilon$. They proposed that the stress required to cause a given strain increment is one that causes maximum work on the system, allowing determination of which particular stress state will cause a given strain, along with the corresponding set of slip systems. This is determined by evaluating which stress and strain increments maximise the work done:

$$\delta w = \Sigma \sigma_{ij} \delta\varepsilon_{ij} \tag{1.5}$$

Curiously, Bishop and Hill's method produces the same value of work done as Taylor's theory, and both predict identical slip system combinations for a given stress state. However, unlike the Taylor theory (which requires 384 calculations) Bishop and Hill's method requires only 56 stress state calculations to determine the active slip systems. These stress states have been given standard abbreviations by Bishop and Hill, and the "Bishop Hill notation" is often quoted in literature to describe a given combination of slip plane and direction (Table 1.1)[3].

Plane	a = (111)			b = $(\bar{1}\bar{1}1)$			c = $(\bar{1}11)$			d = $(1\bar{1}1)$		
Direction	$01\bar{1}$	$\bar{1}01$	$1\bar{1}0$	$0\bar{1}\bar{1}$	101	$\bar{1}10$	$01\bar{1}$	101	$\bar{1}\bar{1}0$	$0\bar{1}\bar{1}$	$\bar{1}01$	110
System	a I	a II	a III	b I	b II	b III	c I	c II	c III	d I	d II	d III

Table 1.1 Bishop-Hill notation for slip system designation[2].

Dillamore *et al.*[7] applied Bishop and Hill's work to predict the rotations of crystals with starting orientations of <111> and <110> transverse directions under plane strain compression (rolling). The difference between strain increments determines the crystal rotation, and this is clearly dependant on the choice of slip system. Since the transverse direction is constrained, the number of independent slip systems required to impose a shape change is reduced to 4, but even with this reduction in operative slip systems, slip system selection is still ambiguous. It is possible for two sets of shears to satisfy the same imposed strain, but give rotations of opposite sign. These workers account for the ambiguities by assuming that the orientations that rotate most rapidly dominate the texture development. Bishop and Hill's method was then applied to determine which

systems will operate, and in what proportions. The mathematical derivation for the rate of rotation of crystals will not be described here, but yields the following relationship:

$$M`w = d\theta/d\varepsilon \qquad (1.6)$$

where M` is the Schmidt factor, ε the true strain, and θ the rotation angle in radians.

These rotation rates were plotted as a function of θ, the angular distance from (110) [001] to a maximum of $\pi/2$ at (001)[$\bar{1}\,\bar{1}$0] (Fig. 1.4). This plot shows that the stable orientations lie 8°14` from (112)[$\bar{1}\,\bar{1}$1] for a <110> transverse direction, and at {110}<112> for a [111] transverse direction.

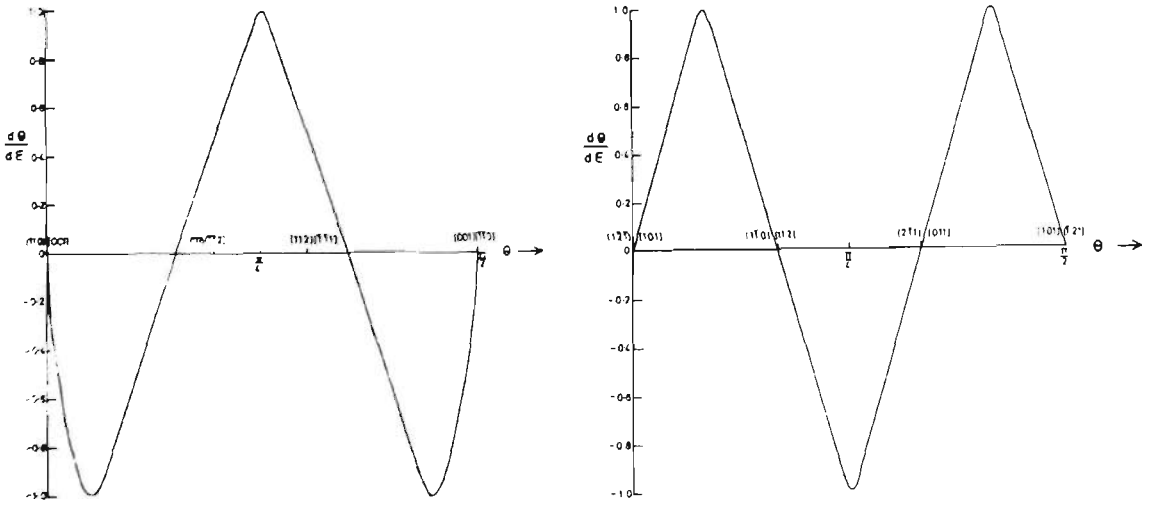

Figure 1.4 $d\theta/d\varepsilon$ for fcc crystals having [$\bar{1}\,\bar{1}$1] and [$\bar{1}\,\bar{1}$0] transverse directions[7].

The full constraints models, however, have some fundamental shortcomings in their basic assumptions. Leffers[8] states that the internal stresses within a grain are not only the result of applied stress, but also due to the interaction of adjacent grains which must,

to maintain contiguity, remain joined by a common grain boundary. The following sections on relaxed constraints describe the various ways in which different workers have attempted to more accurately predict crystal rotation.

1.5.2 Zero Constraints

Originally proposed by Sachs[9], the no constraints model assumes that each grain deforms by slip independently of its neighbouring grains, and slip is predicted to occur on the systems which have exceeded the critical resolved shear stress, τ_c. A schematic illustration of the difference between the zero constraints and full constraints models is shown in Fig. 1.5[10].

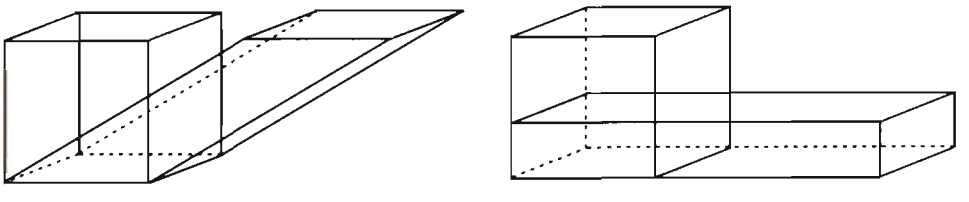

(a) Sachs - single slip (b) Taylor - multiple slip

Figure 1.5 Shape change of a cubic grain deformed by homogenous slip (a) shear due to single slip as assumed by Sachs model (b) plane strain compression due to multiple slip as assumed by Taylor model[10].

In coarse grained metals, the centre of the grain deforms in an unconstrained manner, and this behaviour is best described by the Sachs model. Deformation occurring at grain boundaries and other obstacles is best approximated by the fully constrained Taylor theory[11, 12]. This implies, as is known experimentally, that deformation is not homogenous across a single grain, and that the differences in slip activity throughout the

grain may cause deformation heterogeneities such as those described in more detail in the following sections.

1.5.3 Relaxed Constraints

The modern theory of polycrystalline plasticity acknowledges that the centre and the boundary of a grain will deform differently. Knocks and Canova[12] postulate that the number of slip systems that are required to operate is only as many as the number of constraints (in strain). Consequently, under some conditions such as plane strain compression, only 4 systems are required to satisfy the continuity of shape change condition. In some instances, only 3 or even 2 systems are sufficient, but these extreme cases generally only occur in the grain centre (Fig. 1.6a and b).

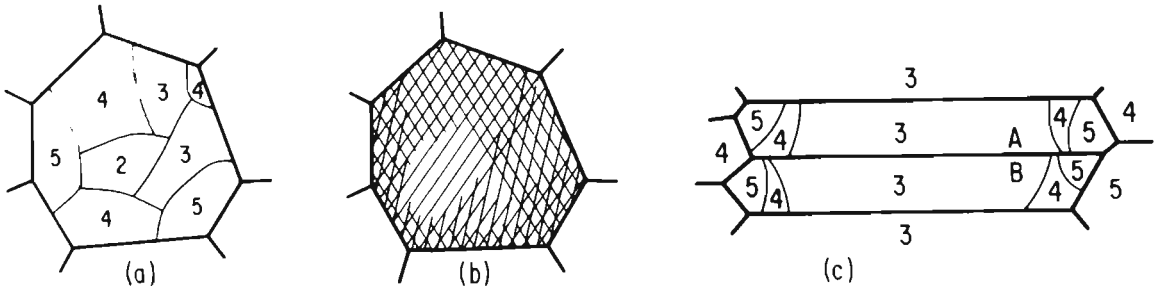

Figure 1.6 (a) Schematic diagram of the number of slip systems operating within one grain; (b) expected slip line traces produced on a polished face; (c) schematic of grains after compression. Numbers indicate number of slip systems expected in various regions of a randomly oriented grain[12].

Knocks and Canova[12] have demonstrated this model using a pair of grains (A and B in Fig.1.6c) that have been deformed in plane strain compression. Across the grain

boundary certain strains must remain continuous under any applied load, and are as follows:

$$\varepsilon_{yy} = \varepsilon_{yy} \qquad \varepsilon_{zz} = \varepsilon_{zz} \qquad \varepsilon_{yz} = \varepsilon_{yz} \tag{1.7}$$

Since compression limits $\varepsilon_{xx}<0$, and lateral spreading is prevented by roll friction or a channel die, then $\varepsilon_{yy} = 0$ and $\varepsilon_{zz} = -\varepsilon_{xx}$ (by constancy of volume). The strain ε_{yz} averages to a value of zero due to symmetry. The constraints can be summarised by:

$$\varepsilon_{yy} = 0 \qquad \varepsilon_{zz} = -\varepsilon_{xx} \qquad \varepsilon_{yz} = 0 \tag{1.8}$$

These three conditions are the only three constraints on the grain, requiring only three slip systems. Since there are only three constraints compared to the five applied by Taylor, the model is described as the partial or relaxed constraints model.

1.6 Deformation Microstructures

Plastic deformation is a complex process. Initiation of slip is quickly followed by the multiplication of dislocations from various sources producing an increase in stored energy through dislocation density. To decrease the internal energy of the system, dislocations tend to congregate into tangles which, with continuing deformation, form into walls of dislocations, surrounding a relatively dislocation free interior. This produces a substructure within the grains of the metal, and the dislocation boundaries are referred to as low angle grain boundaries (LAGB) or as subgrain boundaries. These

subgrains have a small boundary misorientation, usually ~2°, and whilst the material is deforming, the cell structure remains equiaxed. The formation of these cells is a dynamic process which continuously develops throughout deformation[1, 11].

1.7 Deformation Inhomogeneities

Deformation throughout a grain in a polycrystalline aggregate is not homogenous, it is influenced by the behaviour of its neighbouring grains. As a consequence, inhomogenous flow within a grain may occur, resulting in what are referred to as deformation inhomogeneities. The following sections describe these deformation structures and their relevance to texture development.

1.7.1 Deformation Bands

Barrett[13] first reported that the surface of deformed polycrystals had a banded appearance, and he termed these *deformation bands* (Fig. 1.7). These bands are regions of differing crystal orientation, a result of the operation of different sets of slip systems in adjacent areas within a grain. Deformation banding causes a spread in the deformation texture of a material, and may occur under many deformation conditions such as rolling, drawing and tension. Chin *et al.*[14] has classified these bands into two types, and the first is a consequence of the multiplicity of slip. Taylor[4] first described the ambiguity resulting when more than one set of slip systems produces the same work for a given strain. When this occurs, one set of slip systems may operate adjacent to another different set, resulting in regions rotated away from one another. Hence, operation of a number of slip systems in different areas of a grain, each with the same

homogenous strain, may result in the formation of the first type of deformation banding[11, 14-16].

The second type of deformation banding occurs due to the inhomogenous deformation that occurs within a grain. Unlike the Taylor theory, which assumed that deformation occurs homogenously throughout each grain, deformation within a grain of a real material occurs under the influence of the flow behaviour of the surrounding grains. Consequently each portion of a grain may be under a different applied strain, and in response may deform in a different manner. Chin *et al.*[14] propose that if the work to accomplish a shape change by deformation banding is smaller than the work by slip alone. then banding will occur within the grain.

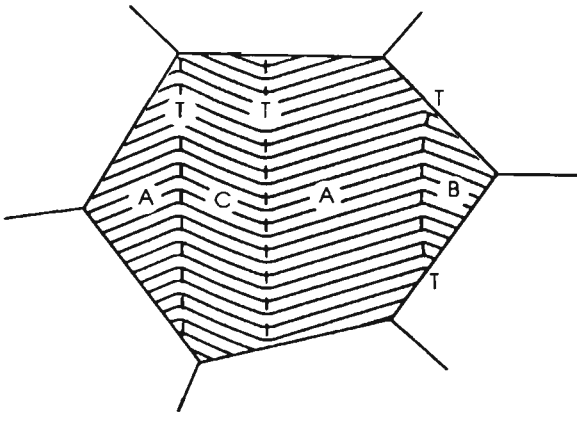

Figure 1.7 Schematic illustration of deformation banding, T represents transition band. A represents regions of same crystallographic orientation separated by deformation band C[11].

Deformation bands are known to become more prolific at lower deformation temperatures, with bands becoming finer and having a larger misorientation. Higher strain rates promote deformation banding, and reduce the total strain required to induce banding[17, 18].

Smallman and Lee[19] have observed an average of 25 deformation bands per grain in coarse grained copper after 85% reduction. When this flat section of 25 grains is extrapolated to the 3 dimensional grain, up to 600 deformation bands can reside within a single grain. Deformation banding is more prevalent in metals that have a larger grain size[20].

Deformation bands have been observed[21] to subdivide into secondary and even tertiary bands inclined at a different angle to the parent band. The microstructure within deformation bands consists of a series of dislocation cells or subgrains, the specific morphology of which is dependant on the characteristics of the deformation band. Adjacent bands may be significantly different in their structure[22].

Deformation banding has been studied by Dillamore and Katoh[23], who propose that deformation bands form by diverging crystallographic rotations under applied strain. Their theory of deformation banding and its impact on the formation of recrystallisation textures is discussed in more detail where relevant (section 2.8).

1.7.2 Transition Bands

Separating deformation bands from the remainder of the grain is a region of high orientation gradient known as a transition band. Walter and Koch[24] conducted an extensive study of deformed silicon-iron single crystals and characterised the microstructure of the resulting deformation and transition bands. They observed transition bands 2-3 μm wide which contained a series of elongated subgrains, each running parallel to the transition band. The LAGB separating these subgrains had an

average misorientation of ~2°, and the orientation change between deformation bands of ~40° occurred by successive 2° rotations across parallel boundaries. Further study[25] has shown that in some instances a large orientation change of 50° or more may be accommodated over a volume only 2 subgrains wide. For example, Hjelen *et al.*[25] have observed a transition band in commercial purity Al in which deformation bands of Copper $(112)[11\bar{1}]$ and Cube (100)[001] texture components have been separated by only one subgrain, whilst other bands have a more gradual orientation change across many successive boundaries. It is commonly found that transition bands contain subgrains that are elongated parallel to the transition band, and that these subgrains have a size advantage over those not lying within the transition region[11, 23, 26].

1.7.3 Microbands

Microbands are long, thin, plate-like cells surrounded by walls of dislocations. The cell interior has a relatively high dislocation density also. They exist within a single grain, and are ~0.2 μm in width. Microbands have been reported to form at strains as low as 0.02 in single crystals of copper, but in polycrystalline alloys it is more usual that they form above strains of 0.1[11]. Microbands are known to form on the {111} planes that are oriented to have the greatest resolved shear stress, around 35° to the rolling direction. On further straining the rotation of the grain in response to deformation causes the microbands to rotate also, and at high strain they can be found parallel to the rolling direction. After formation, microbands do not evolve further. Instead, more bands form resulting in clusters or families. These bands become smaller as the

deformation increases, until the strain reaches a critical point after which they no longer form[27, 28].

1.7.4 Shear Bands

Shear bands are a macroscopic phenomenon that can be seen on the surface of previously polished edges of rolled metals. They are caused by plastic instability during rolling, and occur at rolling reductions above 65% (true strain of 1.05). Shear bands are not crystallographic in nature, usually forming at an angle of ±35° to the rolling direction, and parallel to the transverse direction. Alternate bands may form with the opposite rotation to the rolling direction, causing a herring-bone structure. They form in fcc and bcc structures, and occur in both high and low SFE alloys. For >90% reduction (true strain of 2.3) shear bands become the dominant mode of deformation, contributing significantly to the elongation of the material[27, 29, 30].

Shear bands have a considerable orientation change to the remainder of the matrix, and where they cross grain boundaries the shear band remains undeviated. Shear bands begin as a cluster of parallel microbands, and form only at large reductions when crystallographic slip is inhibited. The constant 35° inclination to the rolling direction (regardless of crystal structure or starting microstructure) is an indication that shear band formation is dictated by the deformation geometry and not crystallography[11, 27].

In low SFE materials such as 70:30 brass, shear bands represent a majority of the deformation between 50 and 90% reduction (true strains of 0.7 to 2.3). However, in high

SFE alloys such as copper, shear banding does not represent the dominant deformation mode[11, 27].

1.8 Deformation Textures in fcc Metals

In previous sections it has been described that during plastic deformation a crystal will rotate to orient itself in a certain direction with respect to the applied load. A polycrystalline material that begins with a random orientation spread can rapidly acquire a preferred orientation through rolling, drawing or tension. Since the present study is concerned with the deformation textures produced during plane strain compression, the textures formed under these deformation conditions will be the focus of the following discussion, however it is sufficient to state that the mode of deformation will vastly alter the deformation texture that develops[1].

When discussing rolling textures, it is convenient to discuss the orientation of the component grains with respect to two references, the rolling direction and the rolling plane. The discrete crystallographic orientations contained in rolling textures are thus defined as (hkl) [uvw], where (hkl) lies in the rolling plane, and the [uvw] direction runs parallel to the rolling direction[1, 31].

Crystal rotations resulting in a preferred orientation are highly dependant on parameters such as initial orientation, SFE, composition and temperature, and each of these parameters has a significant effect on the resultant deformation texture[1].

1.8.1 Cold Rolling Textures

The pure metal or *copper texture* has long been observed in Al, copper and other high SFE fcc metals [16, 32, 33] (Fig.1.8). Some of the discrete orientations present in this texture are listed in Table 1.2. Also listed against these components are the 3 angles which describe their orientation in 3 dimensional space φ_1, Φ, and φ_2. These are known as Euler angles, and Miller indices can be easily converted into Euler angles[34].

When the texture of a metal is described in terms of its Euler angles, these angles can be plotted graphically against coordinate axes to produce a region of 3 dimensional space in which the texture components reside. This 3 dimensional texture is displayed by a series of sections parallel to one of the axes (usually φ_2) forming an orientation distribution function (ODF, Fig. 1.9) [32, 34].

When viewed in 3-D Euler space, the copper texture has intensity maxima along a tube known as the β fibre, and many of the orientations which lie in this fibre are known to be stable rolling orientations (Fig. 1.10)[11, 32, 33].

Component	{hkl}	<uvw>	φ_1	Φ	φ_2
Copper	112	111	90	35	45
S	123	634	59	37	63
Goss	011	100	0	45	90
Brass	011	211	35	45	90
Dillamore	4 4 11	11 11 8	90	27	45
Cube	001	100	0	0	0

Table 1.2 Texture components present in cold rolled fcc metals[11].

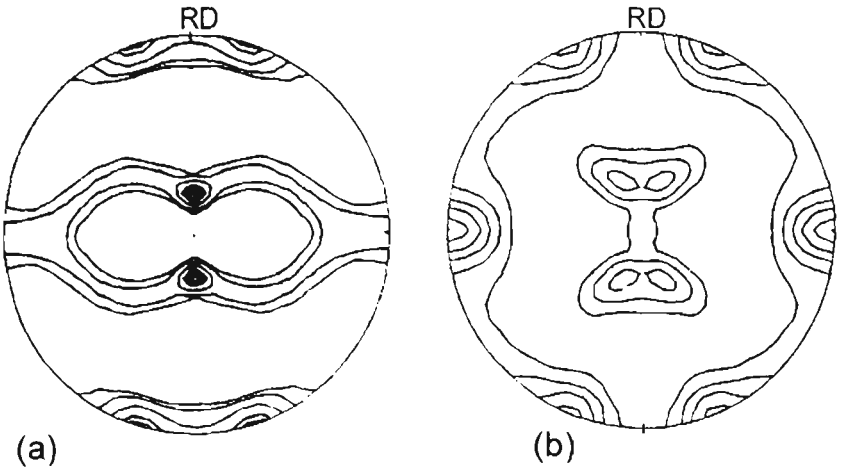

Figure 1.8 (111) pole figures for (a) copper and (b) brass texture[33].

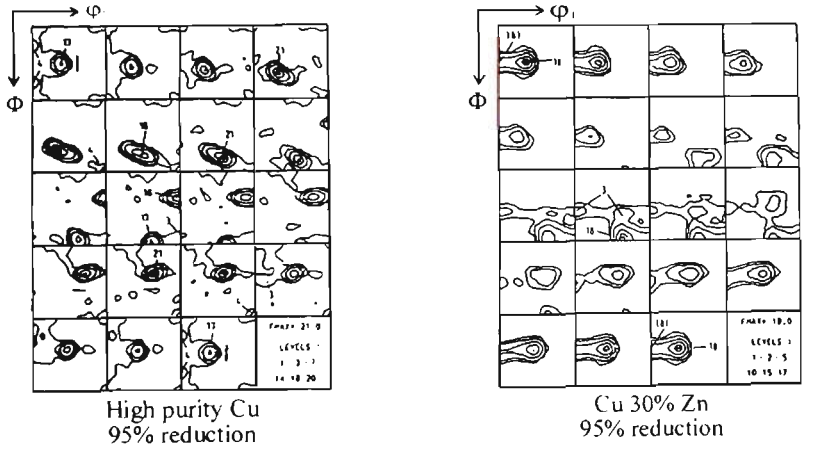

Figure 1.9 Orientation distribution function (ODF) for (a) copper and (b) brass texture[33].

The alloy or *brass texture* (Fig. 1.8b) is observed in fcc metals of low SFE such as 70:30 brass. When viewed in 3-D Euler space the brass texture has a more dominant α fibre, and also has 2 more fibres not present in the copper texture, the τ and γ fibres (Fig. 1.10b)[11, 32, 33].

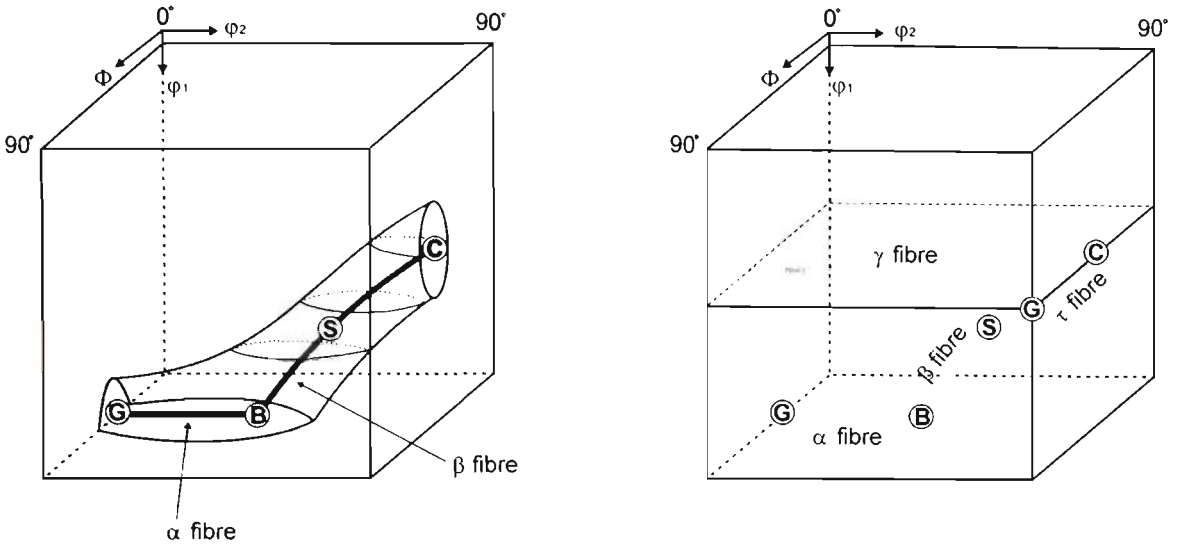

Figure 1.10 Schematic illustration of fibres in 3 dimensional Euler space (a) α and β fibres (b) τ and γ fibres[33].

1.8.2 Hot Rolling Textures

The microstructure produced after hot deformation will depend on the deformation conditions, particularly the temperature and the strain rate. These can be combined into a single parameter, the Zener-Hollomon parameter[11] :

$$Z = \dot{\varepsilon} \exp \frac{Q}{RT} \tag{1.9}$$

Preferred orientations that develop during high temperature rolling are complicated by the restoration processes such as recrystallisation that occur between rolling passes. However, hot rolling generally produces a weaker texture than cold rolling. It is known to stabilise the Cube orientation, which can be retained up to 4 times random intensity, and is also associated with an increase in the Brass and Goss orientations (Fig. 1.11)[35].

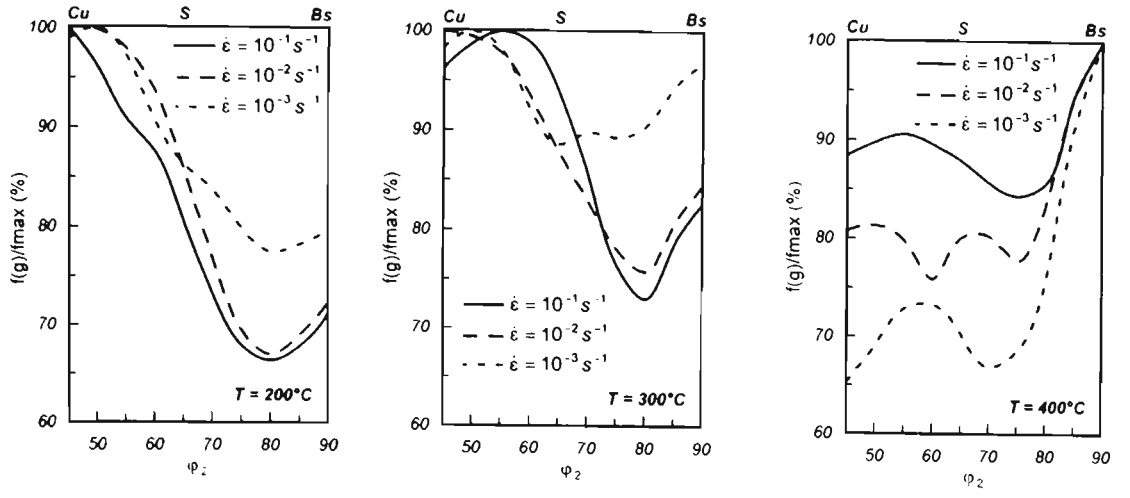

(a) (b) (c)

Figure 1.11 Relative intensities of the β fibre components at (a) 200°C (b) 300°C (c) 400°C[35].

1.8.3 Cube Stability

It has been found[36-38] that during hot deformation of polycrystalline Al alloys the Cube orientation is stable up to high strains. This reported stability has been investigated a number of times through the plane strain compression of Cube oriented single crystals[18, 35, 39].

Low strain rate experiments have been completed by Maurice and Driver[18], and Huang *et al.*[39] have investigated high strain rates (50 s^{-1}). Maurice and Driver state that there is a strain rate dependency on the Cube stability, citing that at 300°C the Cube orientation is stable at 10^{-3} s^{-1} but unstable at 10^{-1} s^{-1}. Furthermore, these workers found that there is a strain insensitive transition between stability and instability, occurring at a constant value of ln Z ~ 28 (Fig. 1.12a). However, closer inspection of Maurice and Drivers'[18] plot does suggest that the transition may be more accurately plotted as a logarithmic relationship with asymptotes at a true strain of ~0.3 and ln Z ~28.

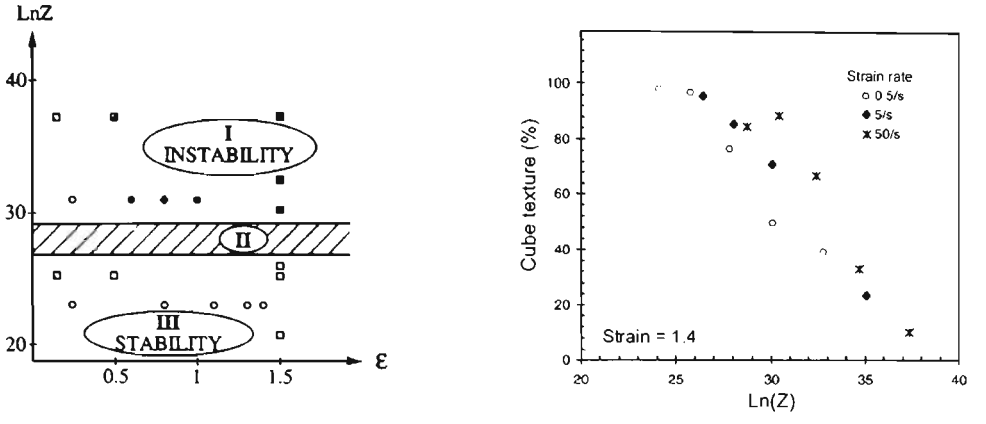

Figure 1.12 (a) Cube stability diagram as a function of the Zener-Hollomon parameter and applied strain. Open circles represent stable data points, closed circles represent unstable[18]. (b) Cube stability as a function of the Zener-Hollomon parameter[39].

Reassessment of this data also shows that the sensitivity of the stability to strain rate is higher at lower temperatures, ie, at high temperatures the Cube orientation is stable at all strain rates. Lowering the temperature decreases stability and also increases the sensitivity to strain rate. The rapid change in strain rate sensitivity is likely to be one reason for the inability of Z to describe the retention of the Cube orientation during high temperature deformation. These complexities in describing this behaviour are also a result of both the unpredictable nature of deformation banding, along with the activation of non-octahedral slip at high temperatures[18, 35].

Huang *et al.*[39] have deformed single crystals of the Cube orientation over a range of high temperatures and at high strain rates to a strain of 1.4. These workers publish the Cube stability as the percentage of material within 15° of ideal Cube orientation (Fig. 1.12b). The relationship between Cube stability and the Zener-Hollomon parameter was

found to be unpredictable. Experiments by Vatne *et al.*[38] on polycrystalline aluminium have also shown that Cube stability cannot be described by Z.

Maurice and Driver[18] propose that the stability of the Cube orientation at high temperatures is the result of the activation of slip on the $\{110\}<1\bar{1}0>$ system. Slip on $\{110\}$ will lead to rotation toward the Cube orientation, and any near Cube orientation (particularly around the transverse direction) which exists before deformation will be rotated toward ideal Cube when deformed under these conditions. The implication of this model is that deformation at high temperatures may actually increase the fraction of Cube orientation, rather than just allowing cube texture to survive the deformation process.

1.8.4 Non-Octahedral Slip

The activation of non-octahedral slip systems in fcc metals of various SFE's has been well characterised[40-42]. It is known to be a thermally activated process[40-42], and its significance in the current study is the supposition by Maurice and Driver [18] that non-octahedral slip is a major contributor to the stability of the Cube orientation at high temperatures.

The operation of non-prismatic slip systems is usually observed through optical microscopy of slip line intersections with the polished face of crystals of known orientation [18, 41, 42]. However, this technique is generally only useful at low strains, less than ~0.15 true strain, due to the complications of crystallographic rotation, deformation banding and a loss in clarity of slip lines, as has been observed in the

current study. Some high strain analysis of slip activity has been carried out using TEM to determine the planes on which cell or subgrain boundaries are formed[40, 42].

Non-octahedral slip is thermally activated [40-42]. It has only rarely been observed at room temperature[43]. Non-octahedral slip has been observed by Le Hazif *et al.* [42] during uniaxial compression of Al, Cu, Ni and Au in the <001> direction. Their observations showed clearly the activity of {111} planes at low temperatures, and found {011} traces at $>0.6T_m$. Anongba *et al.* [40] have found the stress required to initiate non-octahedral slip in Cu decreased with increasing temperature, and these behavioural changes have been found repeatedly to occur in conjunction with changes in the stress strain curve[40, 42, 44].

Most research shows non-octahedral slip does not occur from the onset of deformation. Le Hazif *et al.*[42] found it to begin only after the onset of stage II work hardening, after a strain of ~0.03. Anongba *et al.* observed non-octahedral slip in Cu single crystals to require stage III work hardening[40].

Le Hazif *et al.*[42] proposed that a small amount of strain allows the cross slip of dislocations from {111} to {011}, activating non-octahedral systems. For this to be the case, initial deformation would always produce octahedral slip first, and these slip traces would be retained after initiation of non-octahedral slip on further deformation. Although Maurice and Driver[18] have observed the slip traces of both octahedral and non-octahedral slip together in Al at 300°C, they found no evidence of octahedral slip at 400°C, with all visible slip lines being traces of {011}.

It is unclear from the currently available data whether slip begins on {111}, followed closely by {011} due to work hardening (such as described by Le Hazif *et al.*), or if non-octahedral slip is the primary deformation mode from the very beginning of deformation when enough thermal energy is supplied.

2 Restoration Processes

2.1 Introduction

Primary recrystallisation is considered to be a discontinuous process : it involves both nucleation and growth. The nucleation event is preceded by an incubation period during which no recrystallisation occurs, and after which the fraction of recrystallised material increases in a sigmoidal fashion. The driving force for recrystallisation is a reduction in the stored energy of deformation, and the driving pressure for migration of grain boundaries is provided by the dislocation density[11, 45].

Recovery and recrystallisation are competing processes, and extensive recovery may inhibit recrystallisation altogether, whilst recrystallisation may occur with minimal prior recovery. Recrystallisation has been described as a cannibalistic process in which new grains nucleate and grow to consume the deformed matrix. This process is driven by a reduction in internal energy, and is also accompanied by an energy release. Recrystallisation is said to be complete when the growing grains impinge on one another, and after this point the grains may continue to consume each other in a process known as grain growth[11, 45]. The aforementioned restoration processes that constitute the annealing phenomenon may be further described as either continuous or discontinuous. Discontinuous processes are composed of both a nucleation and a growth event, resulting in a heterogeneous growth pattern, whilst continuous processes are those in which microstructural changes such as growth occur uniformly, with no identifiable nucleation or growth event[11]. The following discussion describes in more detail those areas of the annealing process which are relevant to the current study.

2.2 Recovery

Recovery is a continuous process by which the dislocations within a material re-arrange to form a well defined substructure, and is driven by a reduction in the stored energy of deformation. During recovery, properties such as hardness, conductivity and yield stress are partially or fully restored, and this occurs by the production of well defined subgrain boundaries (Fig. 2.1)[11, 46, 47].

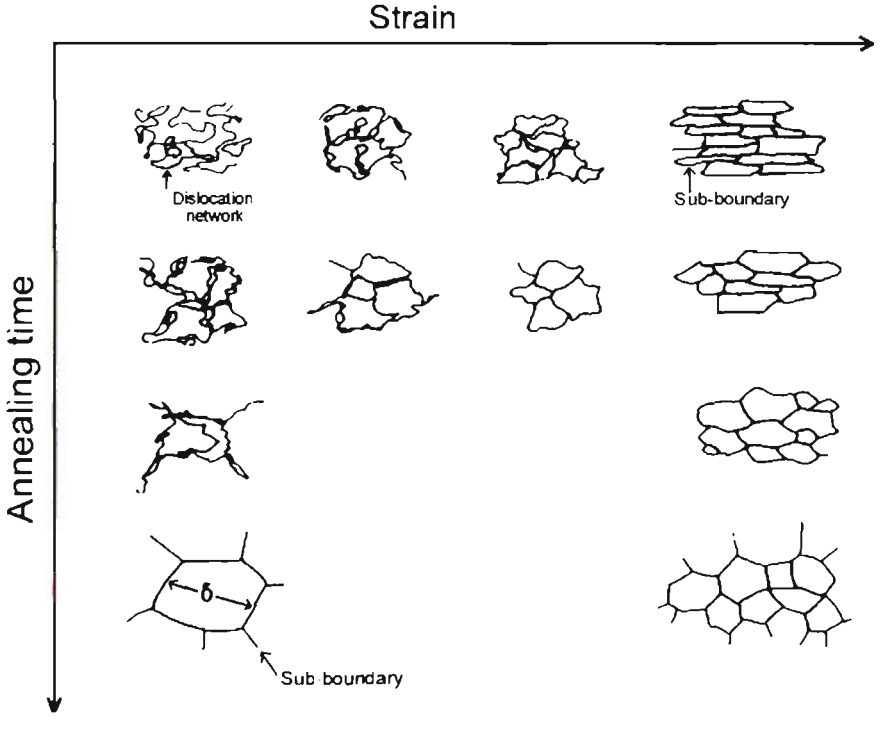

Figure 2.1 Schematic diagram of substructure evolution with strain and annealing[47].

Quantification and modelling of changes that occur during recovery are centred around the development and growth of subgrains, since it is these microstructural changes which produce the macroscopically measured changes in flow stress and hardness etc.

Subgrain growth is analogous to grain growth[48], and experimental observations of the kinetics of subgrain growth show a similar parabolic rate[11]:

$$L^2 - L_0^2 = ct \tag{2.1}$$

where c is a temperature dependant rate constant and L_0 is the subgrain size at time (t)=0.

Experimentally it has been observed[11, 49] that subgrain growth (recovery) in deformed *single crystals* results in a decrease in misorientation between subgrains, and corresponds to a decrease in the spread of misorientations in the microstructure. Subgrain growth allows inconsistencies to be eliminated, reducing the misorientation between subgrains. The stored energy is reduced by both increasing the subgrain size and reducing the misorientation spread.

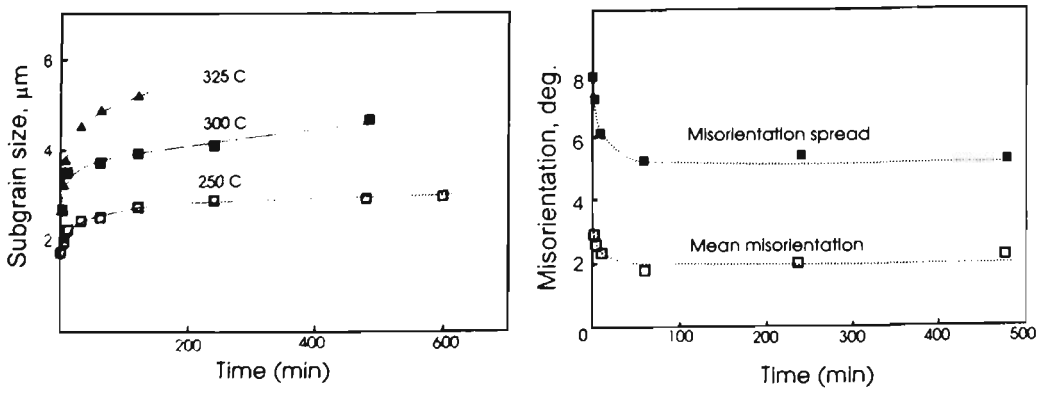

Figure 2.2 Effect of recovery on subgrain size and misorientation in 99.995% Al deformed 20% by cold rolling[11].

The extent and kinetics of recovery are related to the materials SFE. High SFE metals, which exhibit extensive dislocation motion, readily form subgrains that are surrounded

by sharp boundaries. Moderate to low SFE metals may not form sharp sub-boundaries, and may retain a crude cell structure surrounded by dislocation tangles[50]. Annealing of high SFE metals produces a significant decrease in hardness before the onset of recrystallisation, whereas low SFE metals exhibit a sudden and rapid drop in hardness associated almost exclusively with recrystallisation[46, 47].

Solutes may affect the recovery process by changing the SFE in the manner discussed, or by dislocation pinning. Solute drag on dislocations can reduce the propensity for a metal to produce cells during deformation due to the inability of dislocations to migrate. This increases the stored energy, resulting in more rapid and extensive recovery on annealing[11].

2.3 Nucleation of Recrystallisation

Nucleation of recrystallisation occurs through the growth of pre-existing nuclei that form in the microstructure during deformation. This preformed nucleus is usually a subgrain, and the transition from subgrain to recrystallised grain occurs through the discontinuous growth of the subgrain into the deformed matrix[11]. However, approximately 1 in 1 million[51] subgrains grow into a recrystallised grain, the selection of nuclei is still somewhat unpredictable.

Through observation, nuclei are known to have certain characteristics. Growth of the nucleus must produce a high angle grain boundary, which means that a successful nucleus must exist in an orientation gradient, where further growth increases the misorientation across the boundary, imparting an increase in mobility. The other

requirement for nucleation is a high stored energy, a factor usually associated with the orientation gradient, which itself requires a high dislocation density[51, 52].

Given these factors, those sites which nucleate recrystallised grains include grain boundaries, transition bands, shear bands and the deformation zones that surround large second phase particles. These sites are energetically favourable, and usually exist within an orientation gradient[11, 51].

2.4 Dynamic Recovery and Recrystallisation

Dynamic recovery is a restoration process that occurs during hot working, and is a process by which the dislocations within the metal form into a well defined substructure. Initial rapid work hardening increases flow stress and dislocation density. Dynamic recovery occurs simultaneously with work hardening. At a critical strain, ε_m, the rates of work hardening and dynamic recovery reach equilibrium, and this is characterised by achieving a steady state flow stress which does not rise with further imposed strain (Fig. 2.3a). The substructure also reaches a point of equilibrium, and through continued deformation the subgrains remain equiaxed (and may continue to grow) whilst the original grains change shape with further deformation. This behaviour is prevalent in high SFE metals, which experience extensive dislocation motion[11, 53].

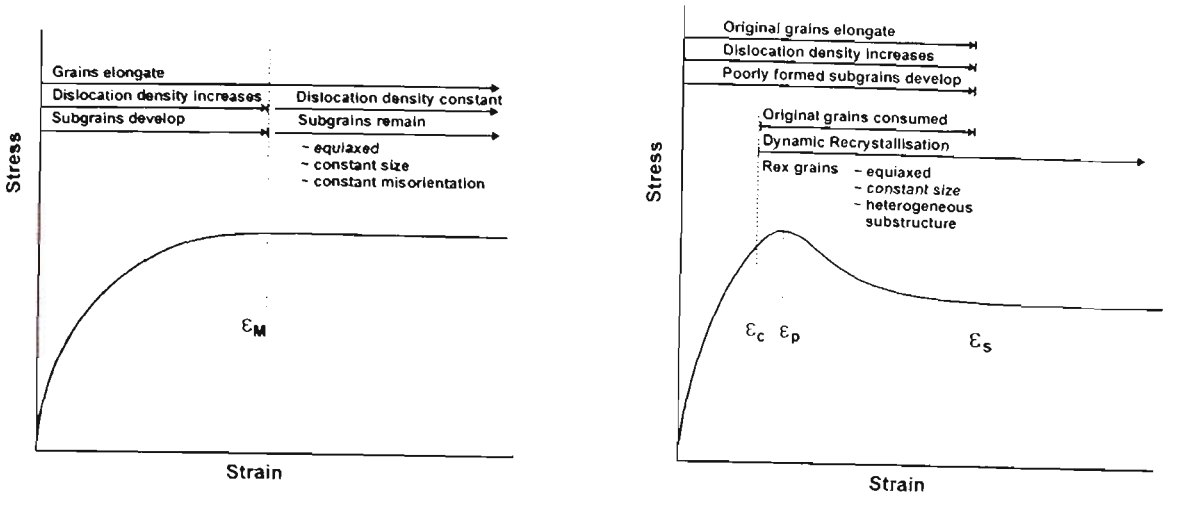

Figure 2.3 Schematic stress-strain curves and microstructural changes which result from (a) dynamic recovery and (b) dynamic recrystallisation[53].

As the Zener-Hollomon parameter (Z) increases so will the flow stress. This relationship has also been linked to the subgrain size, which is inversely proportional to the flow stress, hence deformation at higher temperatures and/or lower strain rates will result in a larger subgrain size after dynamic recovery[11].

For metals of lower SFE the process of dynamic recovery is sluggish, subgrain boundaries are poorly developed and the flow stress increases with strain up to a critical point, ε_c, after which the stored energy is high enough that dynamic recrystallisation occurs. Nucleation of recrystallised grains occurs at grain boundaries to give a necklace structure (Fig.2.4). The interface between these new grains and the deformed matrix nucleate again until a cascade effect recrystallises the entire structure. Before recrystallisation is complete, the original recrystallised grains will have been sufficiently deformed to nucleate again, and simultaneous nucleation, growth and deformation is able to occur. Deformation of the recrystallised structure lowers the flow stress, resulting in a peak at ε_p, followed by the formation of a steady state flow stress

(at ε_s) in which the deformation and recrystallisation processes are in a state of dynamic equilibrium (Fig. 2.3b)[53].

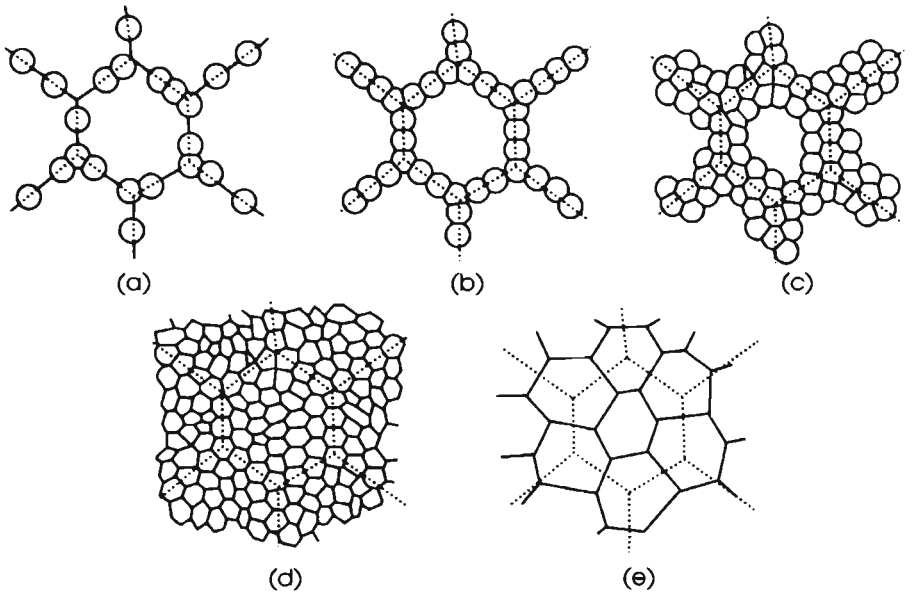

Figure 2.4 (a-d) Development of microstructure during dynamic recrystallisation in an alloy with a large initial grain size, and (e) small initial grain size[11].

As with dynamic recovery, the microstructure formed during dynamic recrystallisation depends on the deformation conditions. The critical strain ε_c, decreases with decreasing Z, and the size of the dynamically recrystallised grains increases with decreasing Z. The dynamic nature of this process prevents grain growth, allowing the recrystallised grain size to remain unchanged throughout deformation. The recrystallised grain size is also independent of the starting grain size, although a smaller grain size raises the kinetics of the process due to an increase in the grain boundary area (where nucleation occurs). Although it is known that increasing the temperature and decreasing the strain rate of deformation (lowering Z) lowers the flow stress, it may also cause multiple peaks in the flow curve obtained during dynamic recrystallisation, and this is associated with grain coarsening. The multiple peaks dissipate at the conclusion of the coarsening[11, 51].

2.5 Grain Boundary Mobility

Three investigations[39, 49, 54] have described quantitatively the mobility of boundaries from low to high misorientations in an Al- 0.05% Si alloy, which is the same alloy used in the current study. The velocity, v, of a moving boundary is given by:

$$v = MP \tag{2.3}$$

where P is the driving pressure derived from the stored energy of deformation, and the mobility (M) has a temperature dependence of the form:

$$M = M_0 \exp[-Q/RT] \tag{2.4}$$

where M_0 is a constant, T is the absolute temperature, Q the activation energy for boundary migration and R is the gas constant.

In the deformed matrix, it has been assumed that stored energy is the result of subgrain boundary energy only, and that there are negligible dislocations within subgrains. This stored energy, E_D, which is analogous to the driving pressure (P) for boundary migration is given by[54]:

$$P = E_D = \frac{\gamma_m \frac{\theta}{\theta_m}\left(1 - \ln\frac{\theta}{\theta_m}\right)}{\bar{L}} \tag{2.5}$$

where γ is the boundary energy, γ_m the boundary energy when the boundary becomes high angle, θ the boundary misorientation, θ_m the misorientation at which the boundary is considered high angle, and $\overline{L}$ is the experimentally measured subgrain diameter. This equation allows calculation of the stored energy through measurement of subgrain size.

Investigation of high angle grain boundary motion has been carried out through artificial nucleation of recrystallised grains at the surface of a deformed matrix containing no high angle grain boundaries prior to nucleation. The growth rate of recrystallised grains was measured *in situ*, and the well documented 40° misorientation growth maxima confirmed for this alloy (Fig. 2.5).

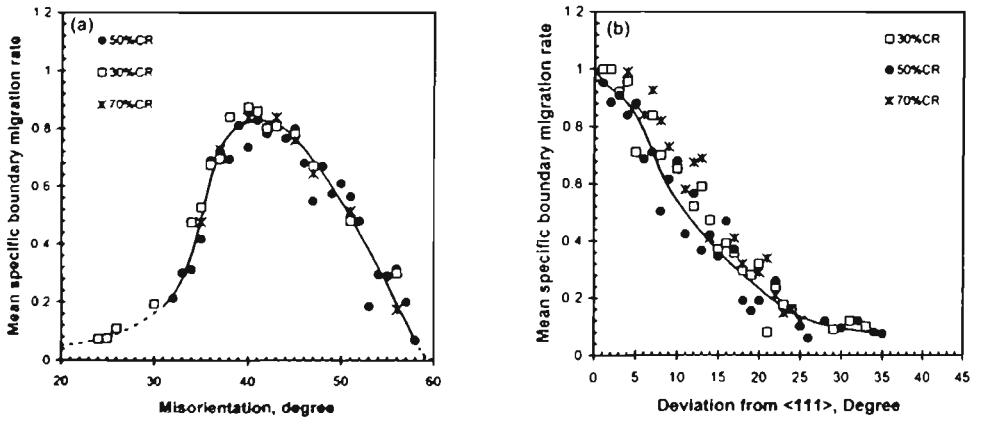

Figure 2.5 Effect of crystallographic misorientation on grain boundary velocity measured in an Al 0.05% Si alloy[54].

Knowing the boundaries velocity and misorientation, grain boundary mobility can be calculated using Eqn. 2.3 above, and yields a temperature dependence as shown in Fig. 2.6.

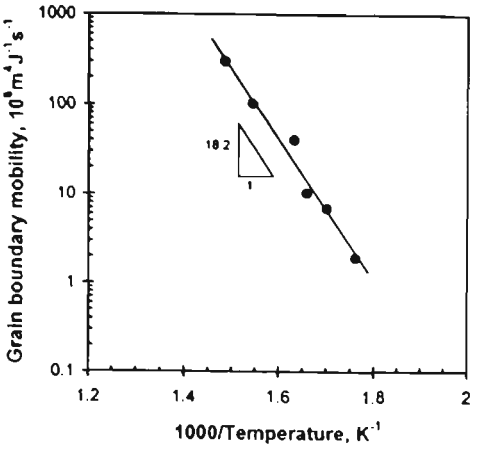

Figure 2.6 Temperature dependence of the grain boundary mobility measured in an Al 0.05% Si alloy[54].

Moderate to low angle grain boundary mobility has been investigated through the deformation and annealing of single crystals. In this case, where velocity is not measured *in situ*, the mobility has been calculated using the relationship[39]:

$$M_\theta = \frac{\left(L_e^2 - L_{eo}^2\right)}{1.34\theta t} \tag{2.6}$$

Where M_θ is the mobility of a boundary of misorientation θ, L_e is the equivalent circle subgrain diameter, and t time.

These measured data have been summarised by the authors to show quantitatively the mobility of boundaries in this alloy with orientation. Of interest to the current study is the plateau of mobility which begins at ~7° misorientation at 300°C.

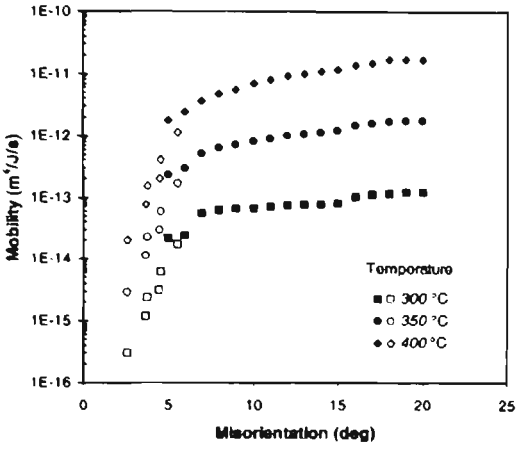

Figure 2.7 Effect of misorientation and temperature on boundary mobility measured in an Al 0.05% Si alloy [39].

2.6 Orientation Pinning

Juul Jensen[55] first used the term "Orientation Pinning" to describe the behaviour of a growing recrystallisation front into an area of similar orientation. Comprehensive mobility studies have shown that the mobility of a boundary can become almost negligible when confronted with a very similar orientation in its growth path. An example of the effect is shown schematically in Fig. 2.8, where a nucleus is shown grey, and similarly oriented subgrains are also grey. In this case, growth is favoured toward the lower left of the nucleus, and the orientation pinning significantly affects the grain shape.

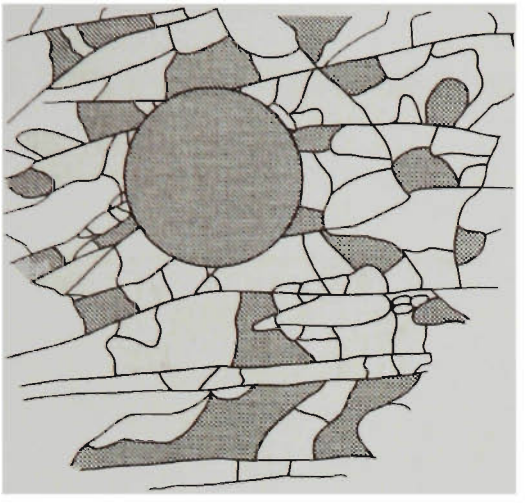

Figure 2.8 Schematic diagram of orientation pinning. Theoretical circular nucleus is shown in grey, with similarly oriented regions also shown grey [55].

Since like orientations pin, nuclei of the rolling texture or β fibre components have little chance to grow due to the high probability of encountering similar orientations in the deformed matrix. Likewise, nuclei that do not lie in the deformation texture have a high chance of becoming a recrystallised grain. Juul Jensen[55] showed through statistical analysis that nuclei of random and rolling texture components were 3 times more likely to be surrounded by low angle grain boundaries than Cube oriented nuclei.

Doherty *et al.* [52] proposed that narrowly spaced bands of similar orientation limit the size of recrystallisation nuclei to the thickness of these bands. They offer a condition for the orientation pinning of nuclei of a certain orientation, it will not appear in the recrystallisation texture if :

$$\lambda v << d_r \tag{2.7}$$

where d_r is the size of a recrystallised grain with an orientation not lying in the main deformation texture or β fibre, and λ_v is the spacing between variants of the same orientation.

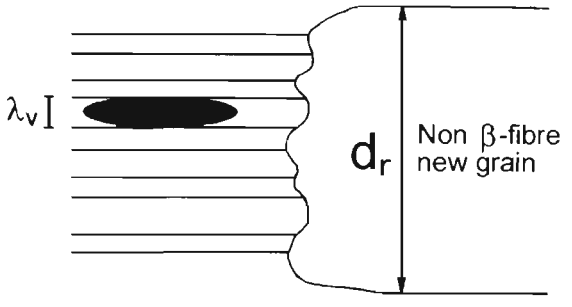

Figure 2.9 Schematic diagram of a large recrystallised grain (d_r) growing into a region composed of layers of similar orientation. Black nucleus is shown originating from the rolling texture with a maximum size of λ_v [52].

The generation of transient recrystallisation textures that appear in the partially recrystallised state, but are consumed to be absent in the fully recrystallised state are thought to be the product of this orientation pinning[52].

Vatne *et al.*[56] have mathematically investigated this orientation pinning, viewing it as both a drag mechanism where similarly oriented regions grow more slowly, and also as a pinning mechanism analogous to Zener particle pinning in which the boundary bows between pinning points and eventually "unzips". Although the authors find the Zener pinning mechanism to be more descriptive mathematically of the phenomenon, they also conclude it to have minimal effect on the recrystallisation texture.

2.7 Theories of Recrystallisation Texture Development

Oriented growth, which assumes that the grains which grow fastest will determine the dominant orientations in the texture, was first proposed after the discovery that grains of certain orientations grow faster than others, specifically, those grains rotated ~40° from the <111> direction of the surrounding matrix were found to have the greatest growth rate[57]. Since this time there have been many investigations into the orientation relationship of the mobility of grain boundaries, and it is now generally accepted that the grain boundary mobility is not only a function of the misorientation, but also of the structure of the boundary. For example, the 40° <111> twist boundary is known to have a lower mobility than the corresponding orthogonal tilt boundary, and as a consequence such grains are elongated along the direction of greatest mobility, and form aspect ratios as high as 50 :1[11, 25].

There are 8 possible rotations a recrystallised grain may take to be oriented 40° about <111> from the deformed matrix. In some circumstances all 8 variants have been found growing into the deformed matrix, but it has also been reported that not all poles respond equally. The oriented growth theory cannot predict which rotation will dominate the recrystallisation texture, demonstrating that the development of recrystallisation textures is more complex than simply determining maximum growth conditions[11, 58-60].

It has also been noted[11] that those experiments which quote a 40° rotation relationship do in fact contain a scatter of approximately 28°, which is clearly too large a spread when investigating a 40° relationship. Further doubt for the oriented growth theory

exists in the microstructure of recrystallised metals, which contain equiaxed grain structures. Since tilt boundaries migrate faster than twist boundaries, a recrystallised structure produced by oriented growth would be expected to be composed of elongated grains resulting from rapidly migrating boundaries of certain types. Furthermore, sharp orientation gradients that result from inhomogeneities such as shear and deformation bands prevent an orientation relationship to be derived, nor maintained through a large distance[11]. Hjelen *et al.*[25] conducted TEM step scans on an Al substructure and frequently found misorientations of up to 35°, with an average misorientation of 5-10°, clearly demonstrating that an orientation relationship cannot be maintained over large distances.

Although it is accepted that some orientations, and certain boundary types can grow into a deformed matrix faster than others, it is not the only factor which determines the recrystallisation texture, and for these reasons the oriented growth theory is not considered the sole factor determining recrystallisation textures[11].

The *oriented nucleation* theory predicts that nuclei of certain orientations are more likely to form a recrystallised grain, and that the recrystallisation texture is determined by these nucleation events. The theories of oriented nucleation have been classified by Smallman and Lee[19] into two broad groups. The first assumes that nuclei of new orientations are formed by twinning or subgrain coalescence, but the more accepted theories predict that the orientation of a nuclei is the same as the structure from which it grew, and this forms the basis of modern oriented nucleation theory. These viable nuclei are more likely to form in regions where further growth is favourable, for example in large orientation gradients or in microstructural inhomogeneities.

There is much experimental evidence of the existence of oriented nucleation, particularly in microstructural inhomogeneities. Ridha and Hutchinson[26] found the nucleation of Cube texture in copper occurred at the centre of transition bands, in the presence of a large orientation gradient. The subgrains in the centre of the band were found to be elongated and had a substantial size advantage over other orientations, and these workers concluded that the Cube recrystallisation texture originates from the growth of Cube oriented nuclei. Hjelen *et al.*[25] conducted an extensive study on the origin of various recrystallisation texture components in Al, and they too conclude that the Cube texture originates in transition bands, and also that the Goss orientation grows from transition regions between Brass and Goss orientations. Shear bands were found to be potent sites for nucleation of the S orientation from subgrains of the same orientation.

Given the logical nature of both arguments, the theory termed "microgrowth selection" is a combination of both the oriented nucleation and oriented growth theories, whereby nuclei of orientations which already exist in the structure can grow into recrystallised grains if they have a high growth potential. The recrystallisation texture is therefore a product of both the growth of nuclei which exist in the structure and also those grains which grow the fastest.

2.8 Recrystallisation Texture in fcc Metals

Cube texture, in which a cube plane of the unit cell is parallel to the rolling sheet, and a cube edge lies in the rolling direction, is an extremely well studied phenomenon. It is a

recrystallisation texture produced after high strain deformation and annealing of metals with a moderate to high SFE, and has been observed in many fcc materials such as copper, aluminium and nickel. An extremely sharp Cube texture can be obtained after deformation and annealing of these materials, and the interest in its behaviour is because of its importance in the aluminium can-making industry[11, 16, 61, 62].

The formation of the Cube texture in Al has been extensively studied. Low reduction (small strain) followed by recrystallisation anneal can be used to almost completely eliminate the Cube texture from Al sheet. Low reductions allow orientations other than Cube to nucleate and grow, and the Cube texture can be reduced to as low as 10%. To promote formation of strong Cube texture, reductions >80% are required. Rapid heating allows complete recrystallisation and consumption of the dominant rolling texture components, promoting the formation of Cube texture. Slow heating rates allow extensive recovery to occur prior to recrystallisation and may result in retained rolling texture components [63].

The recrystallisation texture is also sensitive to composition. The composition will affect the deformation structure, and the propensity for inhomogeneities such as shear bands to occur, which act as nucleation sites during subsequent annealing. The presence of a solute will also affect the recovery rate due to formation of dislocation atmospheres which inhibit both dislocation and grain boundary mobility. For example, addition of Mg inhibits the recovery process, promotes recrystallisation and hence the Cube texture. However, the presence of Fe may reduce the Cube texture component[63]. In general, a metal that can be deformed to produce the copper rolling texture will have a recrystallisation texture dominated by the Cube texture. A deformation texture closer to

the brass or alloy texture will be less dominated by the Cube component, and can produce orientation peaks at other orientations such as S[64].

During hot deformation, prior Cube oriented grains are elongated in the rolling direction, producing bands of Cube material. Subsequently the deformation texture after hot rolling contains a higher portion of the Cube texture than cold rolled material. Post-deformation annealing can produce the Cube texture from these bands, but it is also highly sensitive to composition [36-38, 61, 65, 66].

2.9 Theories of Cube Texture Formation

Dillamore and Katoh[23] analysed the theoretical rotation paths of crystals with a ND (010) during formation of deformation bands. They found that portions of crystal could diverge in opposite directions about the ND, retaining between them a region of material which is of the original (Cube) orientation. This early theory which predicts divergence about the ND has since been shown to be partially correct. Deformation banding in Cube oriented crystals does occur by divergent rotations, but these rotations occur almost exclusively about the TD[67-69]. This mechanism of deformation banding produces a transition band that is a highly potent site for the nucleation of recrystallisation. These predictions are in agreement with observations of Cube texture development in a number of materials[11].

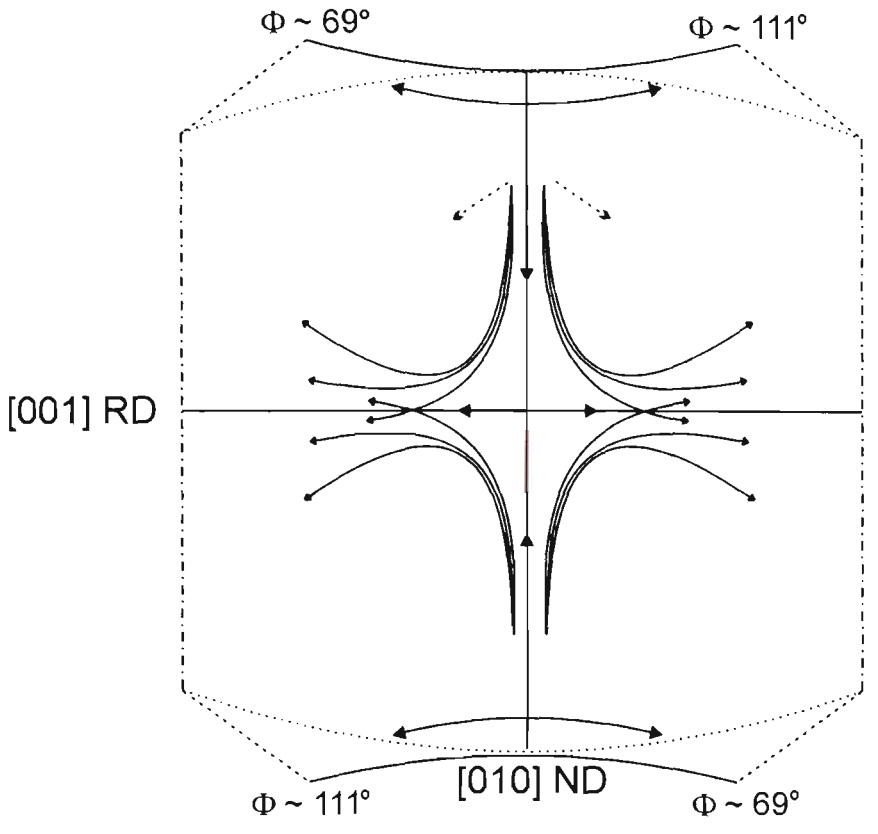

Figure 2.10 Projection onto the plane Φ=90° of the orientations surrounding the Cube texture in an fcc lattice. Arrows indicate the probable slip rotations within this volume[23].

Transition band nucleation has been observed a number of times. Ridha and Hutchinson[26] observed recrystallisation to occur at transition bands in tough pitch copper by bulging of the dislocation cells along the length of the band. Hjelen *et al.*[25] found transition bands formed in commercial purity Al which contained the Cube orientation, and that these orientations are most likely to form within a Copper texture or an ND rotated Copper texture component.

3 Monocrystalline Behaviour

3.1 Deformation Behaviour of Single Crystals

To better understand the mechanisms behind the formation of preferred orientation during deformation of polycrystalline metals there have been a number of studies that investigate the deformation behaviour of single crystals. Much of the reported data are centred on the deformation texture produced by room temperature compression of single crystals of orientations that are of industrial interest. For example, those orientations which compose the β fibre have been studied extensively[35, 70-75]. In particular, the Cube orientation has received much attention due to its presence in the recrystallisation texture of Al, and possibly due to its symmetric nature in reference to the rolling geometry.

The deformation behaviour of an orientation is generally described as stable or unstable[76]. A stable orientation is one which, on deformation, maintains a small spread in orientation. The Goss orientation, (011) [100], which is aligned such that slip occurs equally on 4 slip systems, is stable in room temperature rolling up to 90% reduction[72, 74, 77-79]. Hot deformation of this orientation has only been reported once[49], and no significant effect of temperature on the deformation texture or microstructure was found, other than the usual subgrain coarsening which occurs during hot deformation. Another highly stable orientation is the Brass orientation, $(011)[2\bar{1}1]$, which has been reported to produce only 5° orientation spread after room temperature deformation to strains of 1.5[35, 70, 72-74]. Theyssier *et al.*[73] found evidence of non-

octahedral slip in this orientation when deformed at 400°C, but reported this deformation mechanism to have little or no effect on the deformation texture.

Another orientation present in the β fibre is the Copper orientation, $(1\,1\,2)[1\,1\,\bar{1}]$. It has been studied a number of times in plane strain compression, and is reported to be stable[70], but has some tendency to rotate toward the Dillamore orientation[71, 73]. The microstructure produced by the Copper orientation is extremely different to that of the Goss and Brass orientations. The Copper orientation produces extreme localised shear which occurs at ~40° to the rolling plane, and results in highly developed dislocation networks within and surrounding these bands, whilst the remainder of the material deforms relatively homogenously (Fig. 3.1)[71].

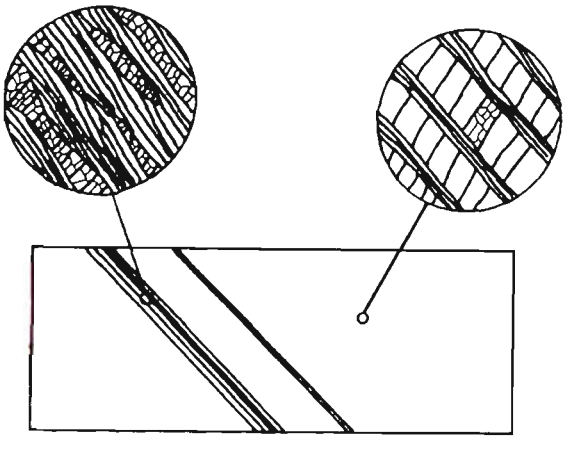

Figure 3.1 Schematic diagram of dense dislocation walls formed during plane strain compression of a single crystal of the Copper orientation[80].

Unstable orientations are those that produce a large spread in texture when deformed. This can be the result of deformation banding, or the orientation may produce a more complex texture comprising rotations about multiple axes.

An orientation which produces extensive deformation banding is 45° ND rotated Cube, (100) [011]. During plane strain compression this orientation produces bands in the rolling plane which rotate alternately about the TD, producing a structure of alternately layered bands of complementary $\{112\}<11\bar{1}>$ orientations which are retained on further straining (the slightly different Dillamore orientation has also been reported)[18, 35, 67, 79, 81]. The deformation temperature does not affect the deformation texture significantly in this orientation, and affects the microstructure only by increasing the width of the deformation bands[35].

Room temperature deformation of the Cube orientation, (001) [100], has been extensively studied. It is known to break up into deformation bands which lie in the ND-RD plane, and which rotate divergently about the TD. After ~60% reduction significant RD rotations lead to many alternate bands and a complex and diffuse deformation texture[18, 22, 35, 39, 67-69, 79, 81, 82]. High temperature deformation has revealed that at and above 400°C the Cube orientation is stable to high strains due to the initiation of non-octahedral slip[18, 35]. The transition from stable to unstable deformation behaviour has not been systematically studied, but has been addressed briefly by Maurice and Driver[18]. This high temperature stability has been reported to occur in other orientations during axial compression by Mecif *et al.* [76] (Fig. 3.2).

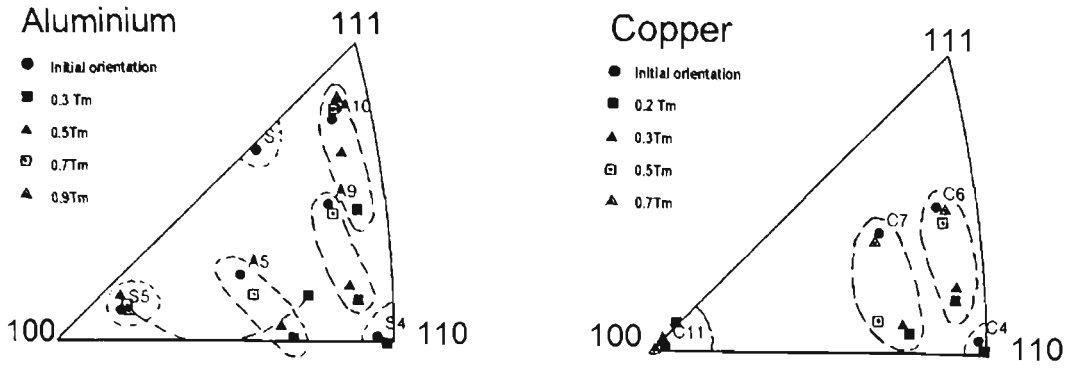

Figure 3.2 Microstructural stability during high temperature uniaxial compression of copper and aluminium single crystals of various orientations[76].

A rotated Cube component that has not been extensively studied is the $(011)[01\bar{1}]$ orientation, which is a TD rotated Cube orientation. The small amount of data available on the $(011)[01\bar{1}]$ orientation has shown its behaviour to be unpredictable. Deformation of this orientation has been reported to produce a stable end orientation[81, 83], a symmetrical rolling type texture[72, 84], and also a fibre texture[85]. It has been used to examine the effect of sundry variables on the formation of deformation bands[72], and has also been described as the perfect opposite to a banded structure[85]. No literature was found that investigated the high temperature plane strain compression of this rotated Cube orientation.

From the currently available data on the subject, deformation texture formation in single crystals can be summarised as follows. Certain orientations, specifically those in the β fibre, exhibit orientation stability up to high strains. High temperature deformation of these orientations may induce non-octahedral slip which appears to have little effect on the deformation texture or stability. Orientations that are unstable at room temperature may remain so at high temperatures, but some can achieve stability through initiation of

non-octahedral slip. These are summarised in Fig. 3.3. The stability of an orientation is not necessarily a function of the symmetry between slip system and rolling geometry, and this may account for the varied effect of non-octahedral slip on texture development.

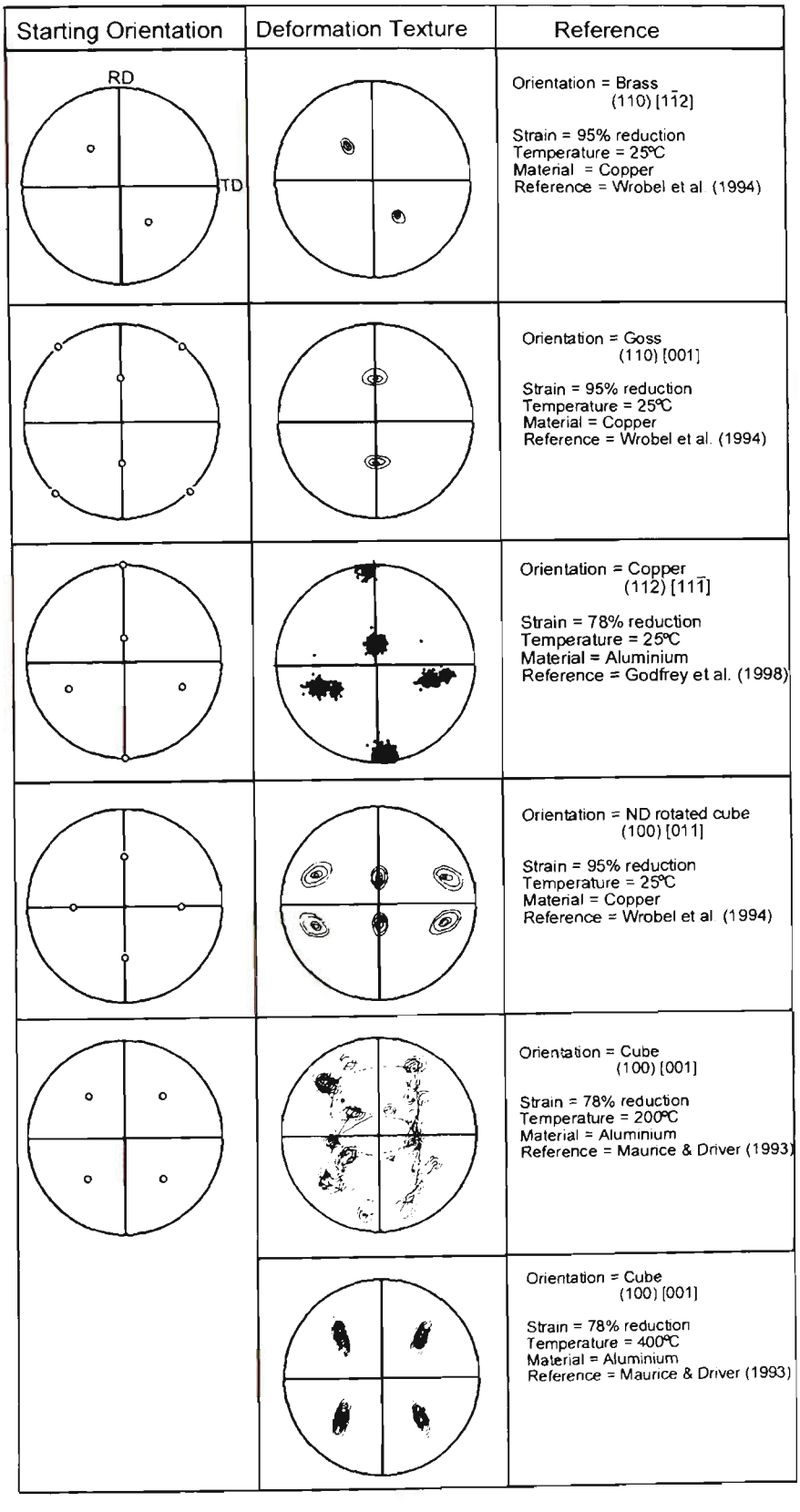

Figure 3.3 (111) pole figures summarising the deformation behaviour of aluminium single crystals of various orientations.

3.2 Annealing Behaviour of Single Crystals

Although the deformation behaviour of monocrystalline Al has been reasonably well elucidated, the annealing behaviour of deformed single crystals is less well understood. Many early post deformation recrystallisation studies of single crystals are of little interest due to the artificial nucleation of recrystallised grains in the deformation field induced by sectioning and polishing. These studies produce large recrystallised grains that dominate the recrystallisation texture, and invariably have an orientation which is rotated by 40° about the <1 1 1> direction of the deformed matrix[58].

More modern studies which electrochemically remove these artificial nucleation sites before annealing have revealed some interesting annealing phenomena. Kamijo *et al.*[86, 87] rolled Al single crystals of stable S orientation between 90 and 99% reduction. Small amounts of Cube oriented material were developed in bands of sub-surface shearing, but these did not significantly affect the deformation texture. Post deformation annealing at 500°C produced a sharp Cube texture, being better developed after higher reductions. Nucleation of recrystallisation occurred in these sub-surface bands, rarely occurring in the sample centre, resulting in the observed strong Cube texture. A study[80] of the Copper orientation reported a recrystallisation texture component of {0 4 1}<6 1 4>. These grains originate in the intense shear bands developed in this orientation during deformation (as described above) and produces parallel bands of small recrystallised grains across the sample width.

In contrast to the inhomogenous nature of the deformed state of these two examples, the Goss orientation produces a homogenous substructure throughout the sample width, and

has no obviously potent sites for nucleation of recrystallisation. Annealing of this orientation produces discontinuous growth of subgrains that lie at the outer edge of the deformation texture[77]. Annealing at higher temperatures (450°C) can produce a fully recrystallised structure consisting of large grains a few hundred microns in diameter with a weak recrystallisation texture[88]. The large grain size is probably the result of very few viable nucleation events, and the texture evolution is consistent with the observation by Ferry and Humphreys[77] that growing subgrains exist on the edge of the deformation texture.

Annealing of the other stable orientation, the Brass orientation, is inconclusive. It has been reported once to produce a weak texture after extensive annealing times (30 minutes at 450°C) but since this orientation is highly stable, this texture may be dominated by a few large grains that have artificially nucleated at the surface. No microstructural evidence that nucleation occurred in the bulk was provided in the report[88].

Annealing of the Cube orientation has been reported by Huang *et al.*[39], but this study focussed on the mobility of subgrains, and did not produce a fully recrystallised microstructure. Cold deformed Cube crystals have been annealed by Engler *et al.*[88] who reported the recrystallisation texture to be close to the recrystallisation texture of polycrystalline Al, consisting of a broad spectrum of orientations and retaining a significant portion of the Cube texture. It is interesting to note that after 92% cold reduction, subsequent annealing produced Cube texture of only ~2 times random intensity. If the expected transition band nucleation were to be active the Cube texture

would be expected to much stronger, since a layer of Cube nuclei running in the RD exists every ~100 μm[89].

Since we have some understanding of the annealing behaviour of stable orientations, annealing of the Cube orientation appears to be the extent of our knowledge on the annealing of unstable orientations. Furthermore, annealing of hot deformed single crystals has rarely been reported, so the effect of deformation temperature on the annealing texture of deformed single crystals remains unknown.

3.3 Summary and Scope of Thesis

Reported investigations of the deformation and annealing behaviour of high SFE fcc single crystals have been summarised. There has been relatively little investigation of the recrystallisation of deformed single crystals, considering the wealth of information available on this topic in polycrystalline behaviour. There are also many deformation conditions to be considered. Each orientation can be deformed under a wide range of conditions depending on the variables: temperature, strain, strain rate, composition, and the presence of second phase particles.

The current study was designed to investigate the behaviour of aluminium through deformation and annealing of single crystals of known orientations. The importance of the Cube orientation has been discussed (sections 2.8 - 2.9), and this orientation has been further investigated through the application of a relatively new technique, atomic force microscopy (AFM). AFM has been used previously to investigate slip line evolution on single crystals of intermetallic metals[90-92], ductile alloys[93] and ionic

crystals[94-96]. The technique allows the quantification of the exact height of slip steps and has a resolution in the nanometre range[97, 98]. AFM has been used in this work to investigate the slip behaviour of the Cube orientation at room temperature over a range of strains.

The high temperature behaviour of the Cube orientation has also been investigated, and extended to include the stability of the Cube orientation at the high strain rates used in industrial rolling ~50 s^{-1}. These conditions have been analysed previously by Huang *et al.*[39], who used a strain of 1.4 and a deformation setup which allowed lateral spread of the sample. The current study repeats the experiment using a channel die which more closely simulates plane strain compression.

Although much literature is available on the deformation behaviour of the Cube orientation, as well as those sites which nucleate the Cube orientation, little data exists on the annealing behaviour of a deformed crystal of the Cube orientation. The current study was also designed to fill this gap.

A second orientation, $(011)[01\bar{1}]$, has been chosen for investigation for a number of reasons. Firstly, literature on the cold deformation behaviour of this orientation is contradictory, mainly due to an extreme sensitivity of deformation texture evolution to the precise orientation[85], and there appears to be no information on its high temperature deformation behaviour. More importantly, this orientation has a unique deformation structure which is vastly different to that formed in the Cube orientation.

These crystal orientations have been used to investigate the effects of microstructural stability and deformation temperature on both the deformation and annealing response of aluminium single crystals. The analysis employed a large spectrum of experimental techniques from optical microscopy of slip line traces to the coupling of AFM and EBSD to fully characterise the deformation and annealing behaviours of these crystal orientations.

Part B

Experimental

4 Experimental Method

4.1 Introduction

The current experiments were designed to investigate in detail the deformation behaviour of single crystals of various crystallographic orientations, along with their recrystallisation behaviour. The study is confined to a single high purity Al 0.05% Si alloy under plane strain compression in order to simulate the deformation conditions experienced during rolling.

4.2 Material Preparation

A high purity Al 0.05% Si alloy was used to produce, by the modified Bridgman method, an <001> oriented single crystal of 15mm diameter. The crystal was analysed to determine its orientation, and sectioned using a SiC blade to produce two rods, one with the Cube orientation (001)[100], and the other with the rotated Cube orientation $(011)[01\bar{1}]$ (Fig. 4.1). Rods were then sliced at intervals to produce samples of identical orientation with approximate dimensions 8x10x10mm.

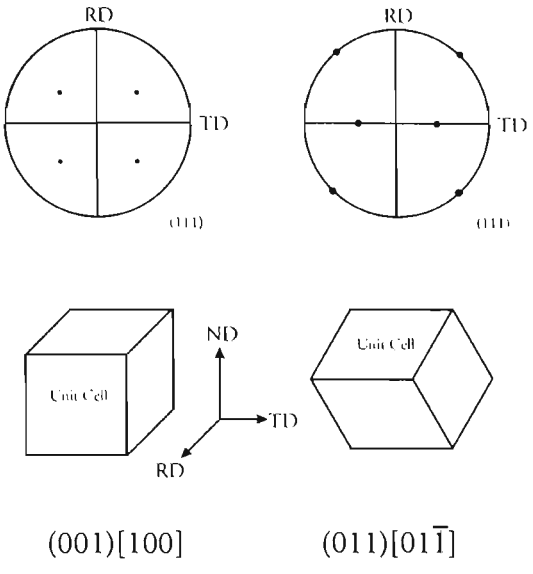

Figure 4.1 (111) pole figures for the Cube (001)[100] and rotated Cube (011)[01$\bar{1}$] orientations along with schematic diagrams representing the relationship between the unit cell and rolling geometry.

4.2.1 Electro-polishing

After mechanical grinding and polishing to 1 μm diamond paste electro-polishing was used to remove the deformation induced by sectioning and mechanical polishing. Electro-polishing was carried out in a solution of 20% nitric acid in methanol maintained at -30°C by a methanol cooling bath. A voltage of 20-25 V was applied between the sample and a stainless steel cathode which supplied a current of approximately 800 mA for a sample with an approximate area of 25 mm^2 for 40 seconds. The polishing time and voltage were extended when the entire sample was to be polished prior to annealing.

4.3 Deformation

Samples were deformed over a range of temperatures, strains and strain rates for a number of specific purposes. All deformation was carried out in a channel die which produces plane strain compression by preventing the lateral spread of samples in the transverse direction (TD), which simulates the conditions experienced during rolling. The advantage of such deformation over actual rolling is the exact control and measurement of temperature throughout deformation, along with precise strain rate measurement. These conditions are shown schematically below. To maintain convention, the rolling, transverse and normal directions are labelled as in rolling, and are hereafter given the abbreviations of RD, TD and ND respectively (Fig. 4.2).

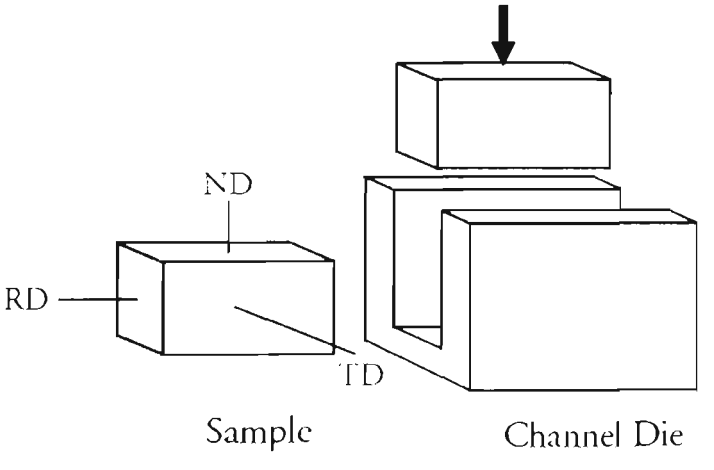

Figure 4.2 Schematic diagram of channel die setup, surface used for AFM analysis shown as grey face.

4.3.1 Cold Deformation

Cold compression was carried out in a channel die using an Instron 4302 Tensile Tester at a rate of 10 mm min^{-1}, producing samples deformed between true strains of 0.06 and 1.20. To reduce the effect of friction, samples were surrounded by graphite for lubrication, and for those samples deformed to large reductions, lubricant was reapplied after strains of ~0.2.

4.3.2 Hot Deformation

High temperature deformation was carried out in a Gleeble 3500 Thermal and Mechanical Simulator, using the Hydra Wedge attachment that allows compression to very high temperatures and high strain rates. The normal plane strain compression dies which are designed to fit the Gleeble were considered inappropriate for such precise experiments, since they produce a 'dead zone' where little deformation occurs, and allows significant lateral spread for such soft materials. Consequently, the small deformation chamber whose maximum width is 60 mm, was fitted with a specially designed channel die which was disassembled between each test to allow retrieval of the last sample, and installation of another (Fig. 4.3).

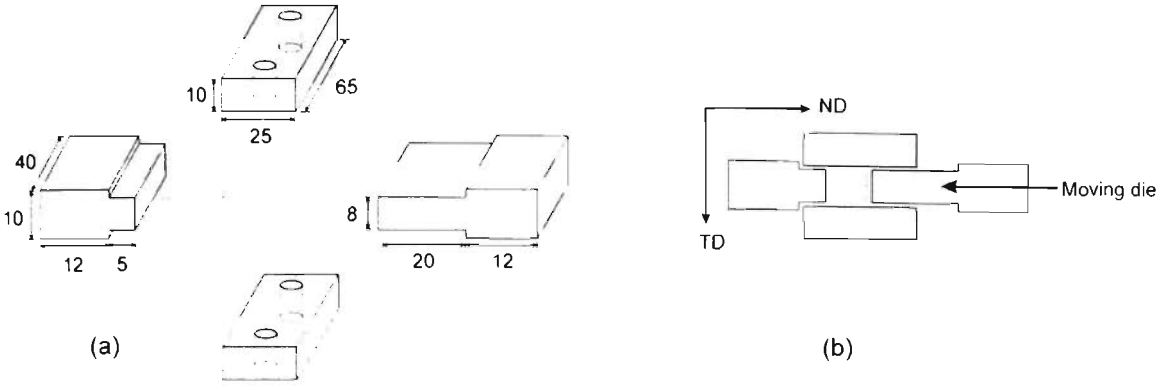

Figure 4.3 (a) Schematic illustration of disassembled die and (b) assembled view of the channel die used during hot deformation. Grey rectangle represents sample, all measurements in mm.

Before each test, the channel die was fitted with graphite sheet on all faces, and a k type thermocouple spot welded to the sample. The channel die was then assembled with the sample *in situ*, and the anvils driven together carefully to avoid deformation of the soft sample before actual testing began, whilst maintaining enough contact between them to allow conduction through the entire assembly for resistance heating. The air ram pressure was reduced to 0.7 kN before each test, and the thermal expansion coefficient for the dies and sample over-estimated to continually reduce pressure on the sample as it heats and softens. The standard operating code was modified for each test and an example is shown in Appendix A. The two major changes were that the initialising stage was carried out under a force of 100 kgf instead of the default 250 kgf, and the quench sequence was extended to continue passing air over the sample after the quench tanks were empty.

Samples were heated at 5°C s^{-1} and the temperature equilibrated for 60 seconds before deformation, followed by immediate cold water quenching. Quenching was complete within 12 seconds of testing, and the temperature was recorded for the heating cycle,

deformation and quench cycle. Deformation was carried out between room temperature and 600°C and at strain rates between 0.005 and 50 s^{-1}.

4.4 Annealing

Selected samples were annealed in a muffle furnace at temperatures between 200 and 400°C. Prior to annealing all samples were ground and electro-polished on every face to prevent preferential recrystallisation at the surface, since this behaviour is not a true representation of the bulk of the material. After completion of the heat treatment, samples were cold water quenched and sectioned for microscopic analysis.

4.5 Microscopy

All samples were viewed in a Leica 440 Stereoscan Scanning Electron Microscope (SEM) using a technique called electron channelling contrast (ECC). This technique reveals both the grain and subgrain structure of a sample, which appear lighter or darker as a result of their varying crystallographic orientations[99]. This technique is also known as orientation contrast. Imaging was carried out using a large area backscattered detector at an accelerating voltage of 12 kV, probe current of 5-20 nA, and a working distance of 12-15 mm.

The samples that were produced for viewing of slip lines on a polished face were digitally photographed using a Leica optical microscope. Micrographs from optical and electron microscopic techniques were imported into the Video Pro 32 Visual Analysis

software package for further analysis. The grain size and subgrain sizes were measured using the linear intercept method, and the percentage recrystallised grains was measured using the point counting method.

4.5.1 Atomic Force Microscopy

Atomic force microscopy (AFM) is a technique that utilises the physical repulsion between solid objects to map surface topography with high resolution. It is based on scanning a small cantilever across the surface of a sample (Fig. 4.4). As the scanning cantilever encounters places of higher and lower surface height a piezoelectric system keeps the sample and lever in contact, recording quantitatively the change of height. This quantitative map is referred to as a "height" map and is recorded in contact mode (the cantilever remains in contact with the sample at all times). The height maps can be displayed in 2 dimensions with the height represented by a colour scale (Fig. 4.5a), or may be shown in 3 dimensions (Fig. 4.5b). A cross section through the height map can be taken to analyse the surface profile more precisely, and an example is shown in Fig. 4.5c.

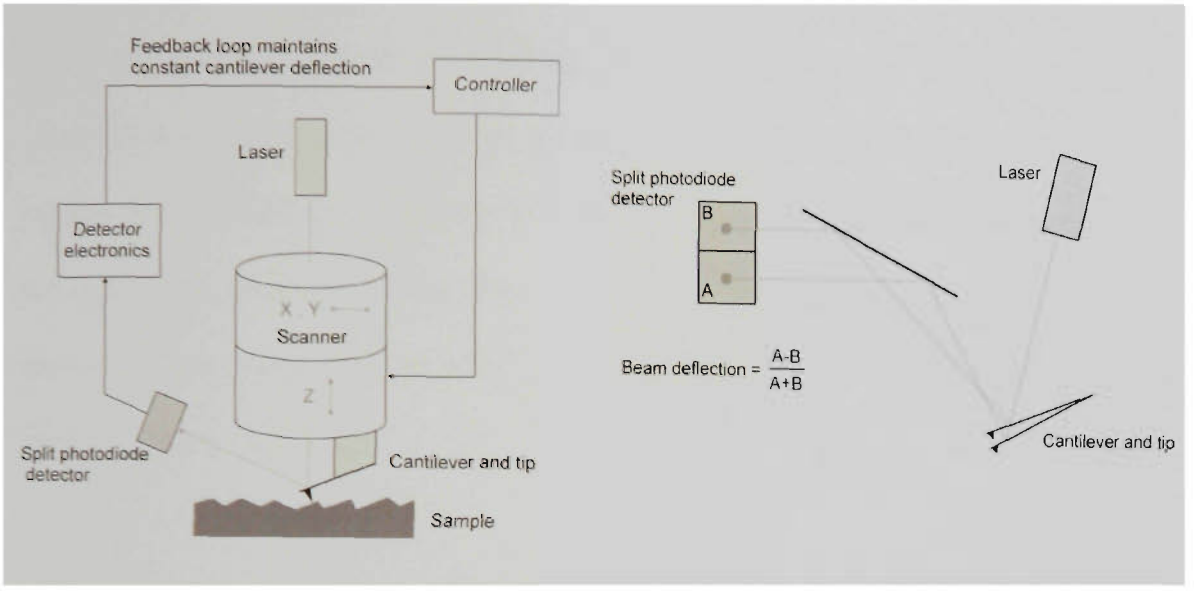

(a) (b)

Figure 4.4 Schematic illustration of atomic force microscopy showing (a) contact mode feedback loop maintaining sample/tip contact and (b) deflection error mode.

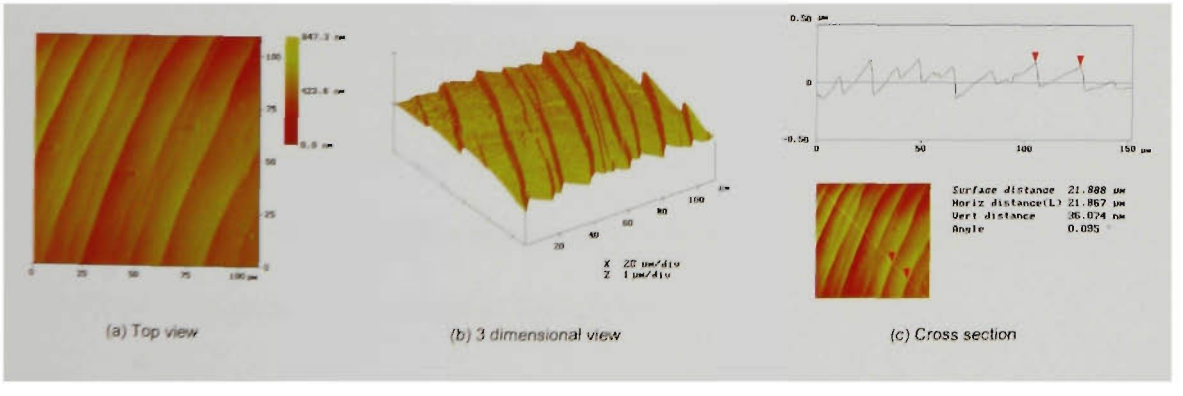

Figure 4.5 Example of AFM height mapping displayed in (a) 2 dimensions with higher areas coloured yellow and lower areas coloured brown; (b) 3 dimensions; (c) cross section through the diagonal of the map, red markers indicate identical positions in the top view and cross sectional profile. The details of the vertical height and horizontal distance between markers are included.

Whilst the contact mode is in operation, AFM can also record two other types of information, the surface friction from the lateral movement of the tip across the sample surface, and the deflection of the tip as it traverses the sample. Both of these techniques are qualitative, and can be recorded concurrently. To compare the three measuring techniques, an example of an AFM scan recorded in height, friction and deflection modes is shown in Fig. 4.6.

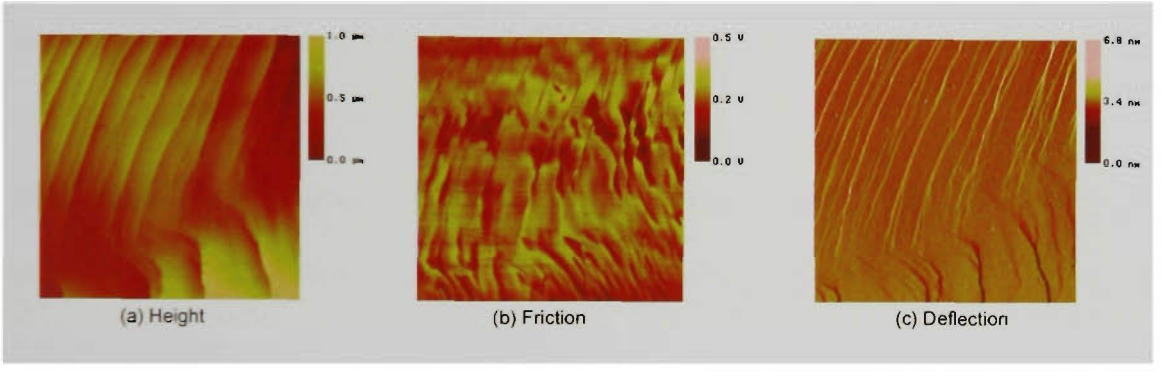

Figure 4.6 Examples of the three imaging modes used in AFM; (a) Height mode produces a quantitative map or the surface height of a sample; (b) Friction mode displays the friction of the tip on the sample surface; (c) Deflection mode shows the deflection of the tip.

In addition to data collection in contact mode, the cantilever can be tapped across the sample surface to obtain surface topography information, however, this technique was not found to be particularly useful in the current study.

AFM analysis was carried out using a Nanoscope® scanning probe microscope fitted with silicon nitride tips. No mathematical flattening techniques were used to manipulate data, although line to line correlation of the scan was carried out during collection of data.

Of the three data collection techniques available on the current system, only quantitative height and qualitative deflection modes were used to image surfaces. The friction mode was not found to produce useful information about the surface condition. The height mode was used to measure precisely the height and spacing of slip lines and other features of interest.

Preparation of samples for AFM involved a two step deformation process (Fig. 4.7). Firstly, samples were deformed in a channel die (as described above) to the desired strain. At high strains this produced an inhomogenous surface on the free face (ND-TD) with gradients much larger than the 8 μm height limit of the AFM. These ends were then sectioned, mechanically polished and electropolished to produce a scratch free surface. These were then placed back in the die and deformed an additional ~3% to produce slip lines on the polished face that accompany deformation to a specific strain.

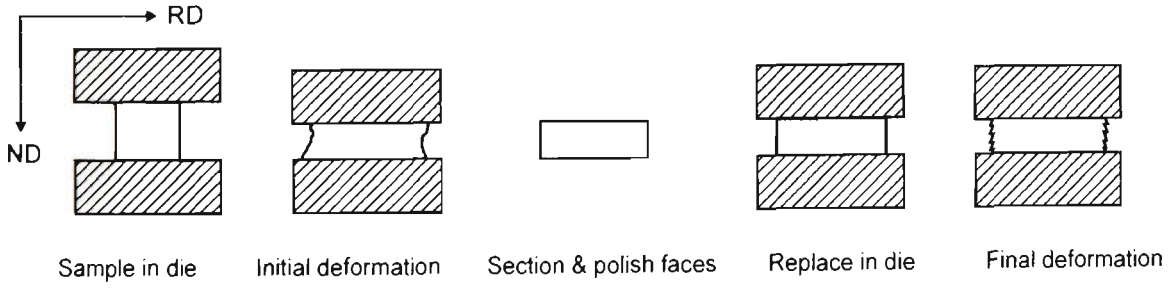

Figure 4.7 Schematic diagram showing ND-RD plane section of sample preparation process for AFM analysis.

4.6 Texture Analysis

4.6.1 Electron Backscattered Diffraction

Both the macroscopic texture of deformed samples and the discrete orientation of single crystals and grains were determined using electron backscattered diffraction (EBSD). EBSD is a surface technique used to determine the discrete orientation of a point on which an electron beam is focussed. Elastic interaction of the electron beam and the crystal structure diffract to produce a pattern which is unique to the orientation of the crystal. This diffraction pattern is incident onto a phosphor screen and this image is captured (Fig. 4.8). These patterns are automatically indexed, and the Euler angles of the crystal in relation to a reference direction recorded. The electron beam can be focussed sequentially in a grid pattern and each point in the grid indexed for its crystal orientation. These points can be reconstructed to produce an orientation map of the area with the resolution determined by the spacing between grid points.

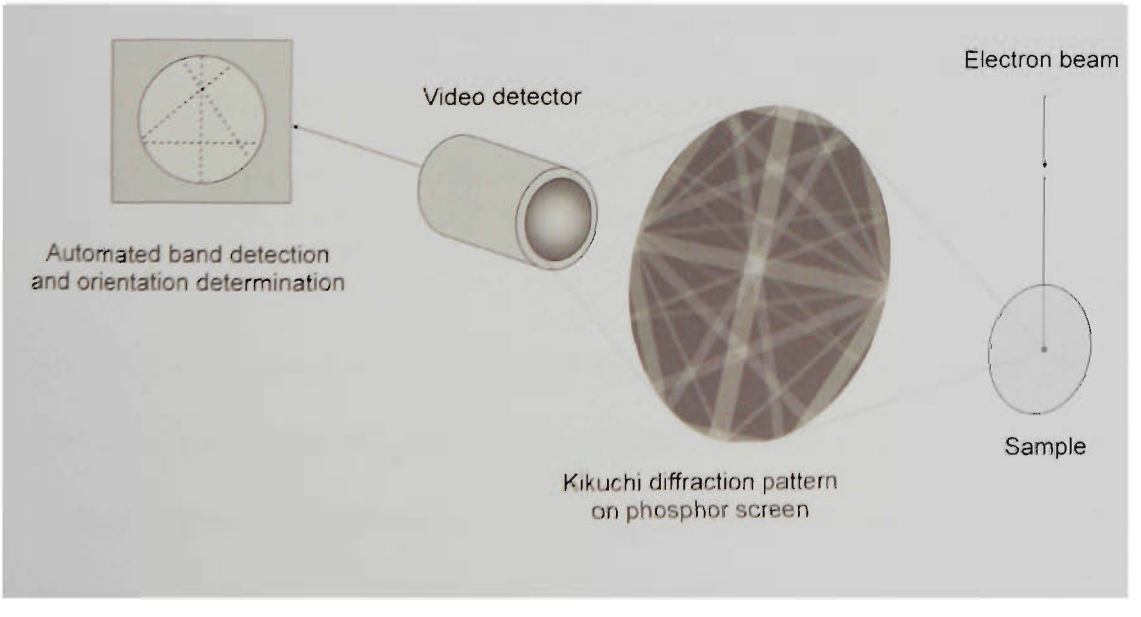

Figure 4.8 Schematic illustration of EBSD experimental setup.

The EBSD mapping can be displayed in a number of ways (Fig. 4.9). The most common is to assign a colour scale to each of the three Euler angles. Crystal orientations that are close have the same Euler angles and appear the same colour. Very different orientations have different Euler angles and appear a different colour. The microstructure is revealed through the change in orientation of different grains or subgrains. Orientation mapping can show all 3 Euler angles ("all Euler"), but can also show the value of just one of the Euler angles (eg. "Euler 1" mapping).

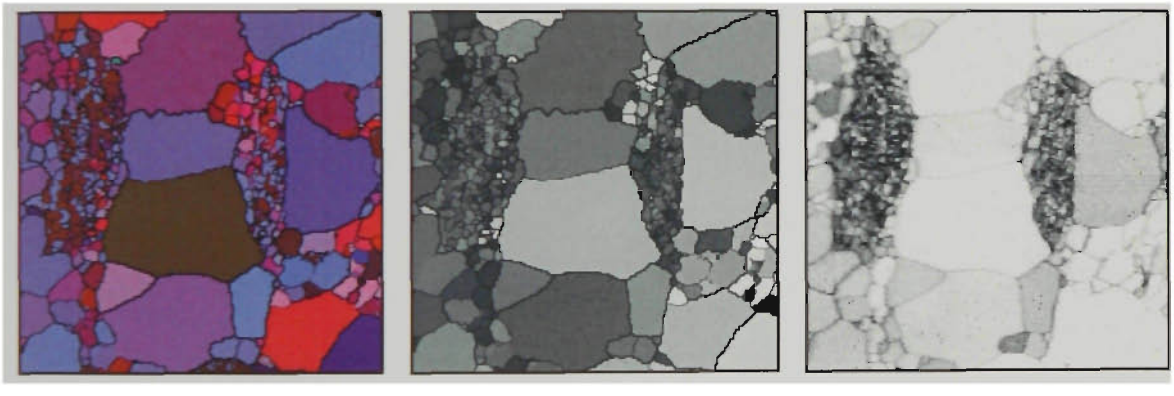

(a) (b) (c)

Figure 4.9 Examples of EBSD maps (a) All Euler orientation mapping, the three Euler angles are assigned a different colour scale which are summed to produce the coloured map shown, the boundaries between grains are shown by black lines; (b) Euler 1 orientation map, the first Euler angle is assigned a grey scale of white to black; (c) "Band contrast" map shows the quality of each diffraction pattern, deformed regions and grain boundaries have a low pattern quality and are shown darker than regions of high pattern quality such as recrystallised grains.

Another useful way of displaying EBSD maps is the "band contrast" map (Fig. 4.9c). This technique records the clarity of the diffraction pattern when it is indexed, and can be displayed as a map with high quality patterns light grey and poor quality patterns dark grey. In a deformed matrix, which appears dark, recrystallised grains appear lighter than their surroundings. Also, within a recrystallised region grain boundaries appear

darker than the interior of recrystallised grains, and sample preparation flaws such as scratches appear on the map also.

EBSD data can be displayed as a pole figure, orientation distribution function, inverse pole figure or shown in 3-D Euler space.

The system used is fully automated, controlled by the HKL^{TM} software package, and is calibrated regularly using a Si single crystal of known orientation. This technique has an absolute orientation accuracy of 2°, and a misorientation accuracy of 0.5°. The SEM conditions for analysis are an accelerating voltage of 20 kV, working distance of 25 mm, sample tilt of 71°, and a probe current between 40 and 90 nA, depending on both filament type and age.

4.6.2 X-Ray Diffraction

X-Ray diffraction (XRD) was carried out using a Philips PW 1729 X-ray generator for texture analysis. A Cu tube with β Ni filter was used as the X-ray source, and data was acquired using Visual XRD 122 software. Most XRD data was acquired using the (111) peak, however, in some instances a satisfactory (111) peak was not produced, and in these cases (220) or (200) pole figures were used to show the deformation texture.

5 Results - Cube Orientation

5.1 Cold-Deformed Microstructure and Texture

Samples were deformed to true strains of 0.06, 0.1, 0.2, 0.4, 0.7 and 1.2, and the microstructure was examined using electron channelling contrast imaging (ECC, Fig. 5.1). At low strains (≤ 0.4) the substructure is not well defined and it is not clear when viewed using ECC (Fig. 5.1a). At the high strains of 0.7 and 1.2 the substructure was better developed, and consisted of cells or subgrains that were elongated in the RD and TD (Fig. 5.1b). On a larger scale, at strains above 0.2, samples were found to develop deformation bands lying parallel to the ND as shown in the ND-TD section of Fig. 5.2c. These bands lie in the ND-RD plane and their width was observed to decrease with strain. The crystallographic rotation between adjacent bands increased with strain, and occurred by alternate rotations about the TD. A schematic diagram of these deformation bands with reference to the rolling geometry is shown in Fig. 5.3.

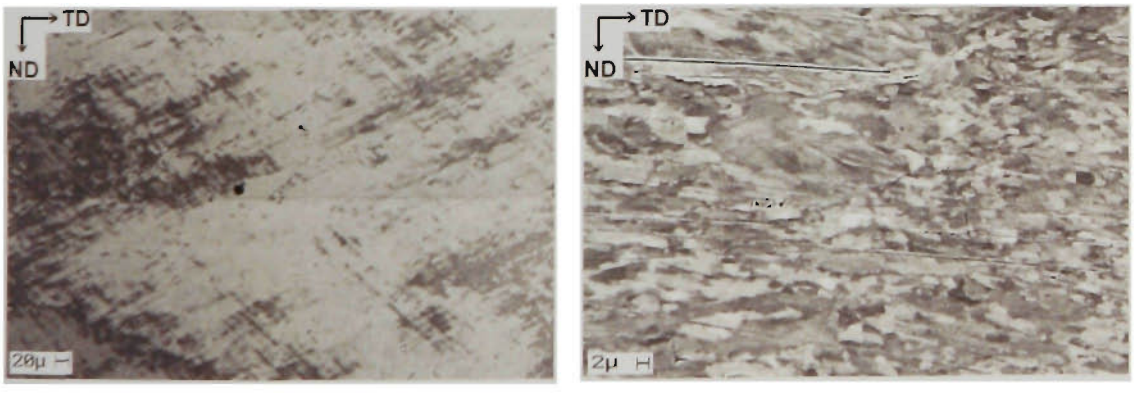

(a) (b)

Figure 5.1 ECC micrographs of the as-deformed microstructures for cold deformed Cube crystals deformed to a strain of (a) 0.4 and (b) 1.2. Note the higher magnification in (b).

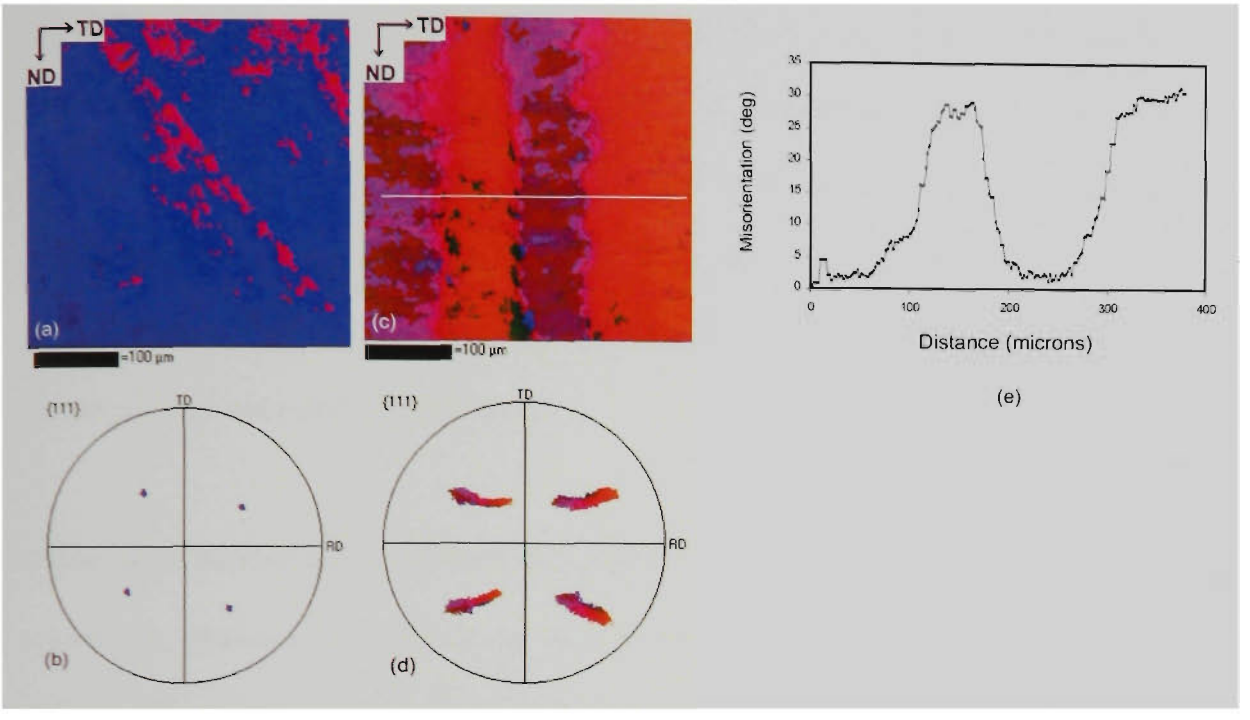

Figure 5.2 (a) Deformed microstructure and (b) texture for Cube crystals deformed to a strain of 0.1. (c) Deformed microstructure and (d) texture for Cube crystals deformed to 0.7. (e) Cumulative misorientation profile across deformation bands in (c).

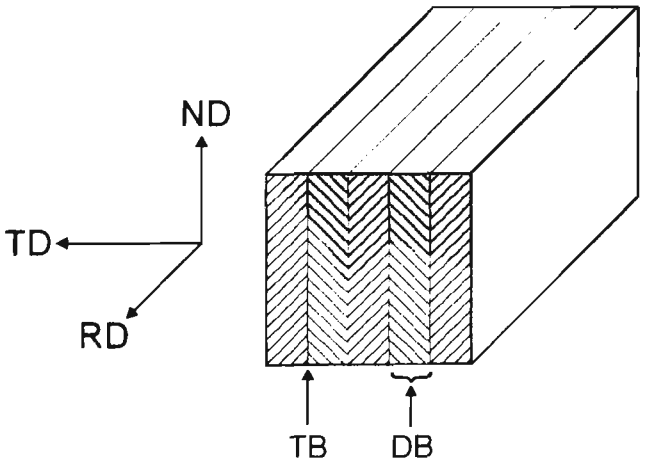

Figure 5.3 Schematic illustration of deformation banding in the Cube orientation with reference to the rolling geometry, TB indicates transition band, DB indicates deformation band.

The deformation texture for each sample was determined using electron backscattered diffraction (EBSD). Figure 5.2 shows both the microstructure and deformation texture after strains of 0.1 and 0.7. Samples were found to deviate from the original Cube orientation by the formation of deformation bands such as those shown in Fig. 5.2c, which developed by a strong rotation about TD. The details of the texture analysis for all samples are summarised in Table 5.1.

Deformation bands produced in the Cube oriented crystals after strains of 0.7 have sharp orientation gradients (Fig. 5.2c), up to 2.2°/μm with an average value of 1°/μm. Adjacent bands are complementary in orientation, being rotated oppositely about the TD to approximately the same magnitude. Between adjacent deformation bands, small amounts of the Cube orientation were detected at all strains. This is demonstrated in Fig. 5.4 where the Cube oriented material is highlighted blue in both the orientation map and the pole figure (other orientations in this pole figure which are not Cube oriented are shown black). With increasing strain, the width of material in the transition band which was Cube oriented became thinner.

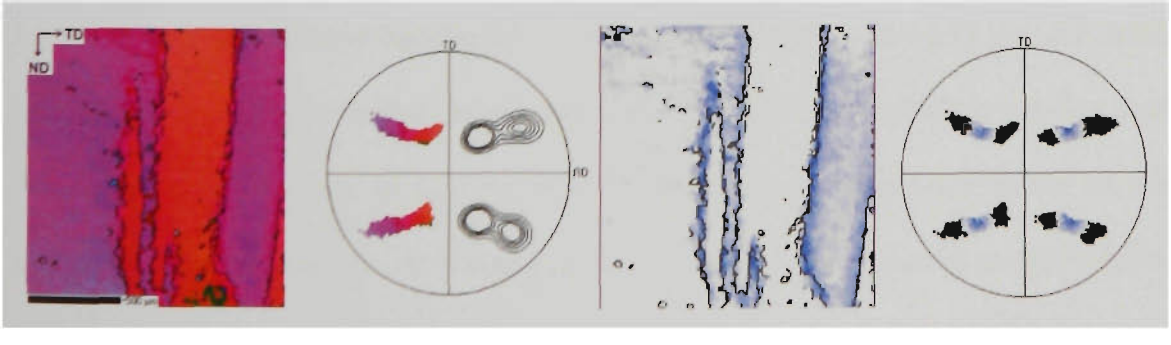

(a) (b) (c) (d)

Figure 5.4 (a) EBSD all-Euler orientation map and (b) (111) pole figure of deformation texture in a Cube oriented crystal deformed to a strain of 0.7. (c) All material within 15° of exact Cube graded blue, the remainder being white (d) (111) pole figure of 15° deviation from ideal Cube shown blue, remainder of deformation texture shown black.

True strain	% within 5° of Cube	% within 10° of Cube	% within 15° of Cube	% within 20° of Cube
0.1	85.5	100	100	100
0.2	24.4	100	100	100
0.4	5.3	54.2	97.5	100
0.7	1.0	14.1	45	71.6
1.2	2.6	15	36.9	46.2

Table 5.1 Percentage of material within 5°, 10°, 15° and 20° of ideal Cube orientation for samples deformed at room temperature.

5.2 Surface Relief Accompanying Deformation

The surface relief that occurs when slip lines intersect a polished surface in association with deformation was investigated using atomic force microscopy (AFM). Both quantitative data and qualitative deflection error mode imaging were recorded concurrently to produce detailed surface topography information.

The gradual change in deformation mechanism from equal duplex slip through to inhomogenous deformation banding by regions of single slip is shown in Fig. 5.5. Each micrograph is a sample section representative of the bulk. Deformation banding was detected at strains as low as 0.2, but at this strain only one band was found on the surface of the entire sample. At a strain of 0.7, the sample was covered in deformation bands of different shapes and sizes, and at a strain of 1.2 the surface was so inhomogenous that no clear regions could be discerned.

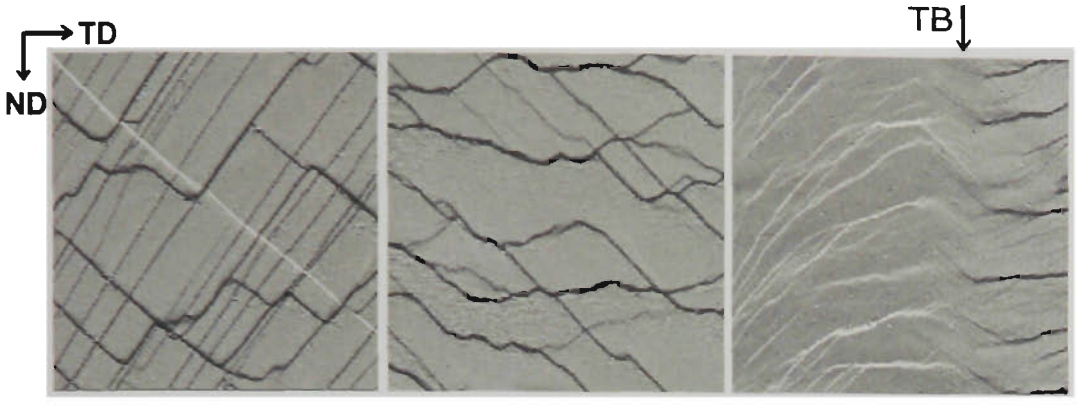

(a) (b) (c)

Figure 5.5 Development of microstructure in the Cube orientation on the ND-TD plane imaged using AFM deflection mode after strains of (a) 0.06 (b) 0.2 and (c) 0.7. Each image is 150 μm x 150 μm. TB = transition band.

After a strain of 0.06 the slip lines are sharp, and traces of the {111} planes are clearly defined. The point of intersection of slip lines is sometimes perpendicular, whilst others are curved. In Fig. 5.5a, the slip lines at +45° to the ND tend to be more closely spaced and continuous, whilst the slip lines at -45° are deeper and are not continuous (they have been slipped through repeatedly). A three dimensional image of this feature in Fig. 5.5a is shown in Fig. 5.6, and using such images it is possible to determine the approximate order in which slip lines have operated. It is clear from Fig. 5.6 that slip does not occur equally on all systems after a strain of 0.06.

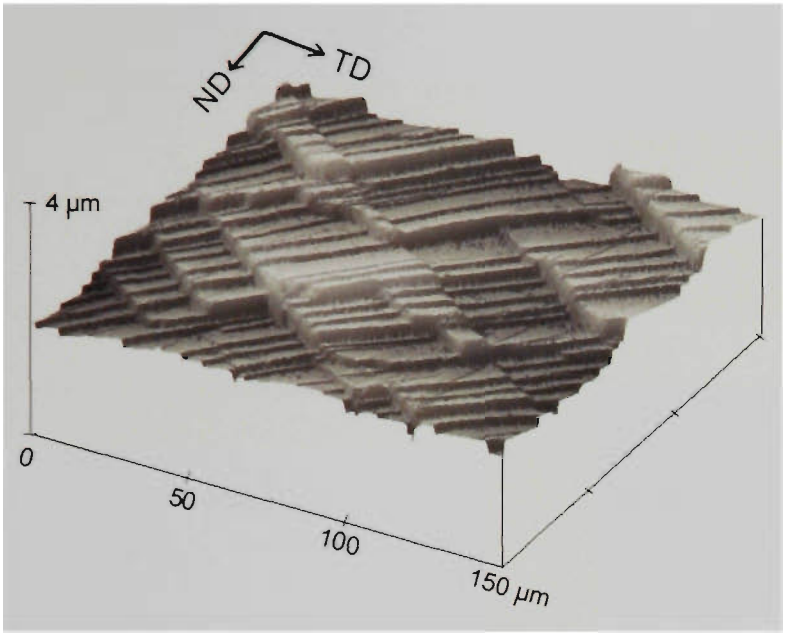

Figure 5.6 AFM quantitative surface profile for Cube oriented crystal deformed to a strain of 0.06. Vertical scale = 4 μm/division, horizontal scale = 50 μm / division.

Surface profiles were drawn perpendicular to slip lines, and the spacing (from peak to peak) of each slip step measured, along with the height of the corresponding slip step. Surface profile lines were drawn perpendicular to slip steps regardless of their orientation with respect to the deformation geometry. A statistical analysis of the slip accommodation on opposite diagonals in Fig. 5.7 is detailed in Table 5.2. The ε_{slip} column is a calculation of the strain produced by the summation of the slip steps across the sample width. The measured strain by slip steps should be close to the macroscopic strain imposed by deformation. The specifics of the calculation are detailed in Appendix B.

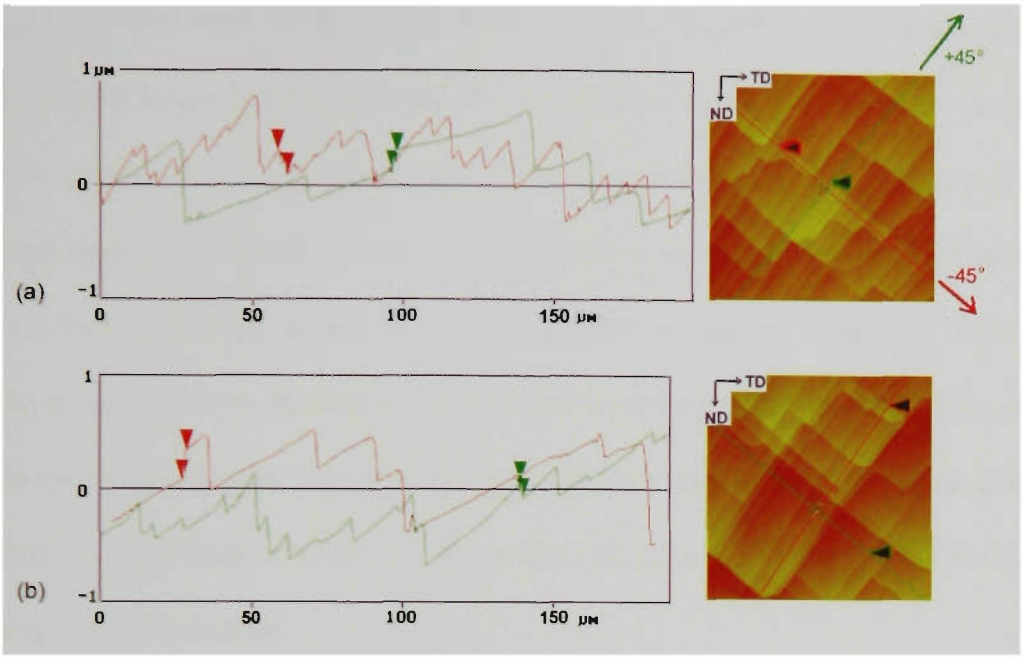

Figure 5.7 AFM surface height profile of slip step steps at ±45° in a Cube oriented crystal deformed to a strain of 0.06. (a) and (b) are two different fields of view.

Sample	n	$\bar{s}$ (µm)	$\bar{d}$ (µm)	r	H (mm)	ε_{slip}
Fig. 5.7(a), ε=0.06, -45°	20	0.25	8.6	0.027	0.242	0.048
Fig. 5.7(a), ε=0.06, +45°	6	0.375	31.0	0.015	0.134	0.026
Fig. 5.7(a), ε=0.06, ±45°	26	0.275	12.9	0.021	0.367	0.074
Fig. 5.7(a,b), ε=0.06, ±45°	46	0.285	13.3	0.022	0.394	0.077
Fig. 5.8(a), ε=0.2, -45°	5	0.578	32.5	0.022	0.184	0.027
Fig. 5.8(b), ε=0.2, +45°	13	0.448	14.2	0.032	0.268	0.039
Fig. 5.8(a,b) ε=0.2, ±45°	18	0.484	18.5	0.027	0.452	0.066
Fig. 5.9 ε = 0.2 Defmn. band	9	0.289	11.6	0.028	0.234	0.034

Table 5.2 Slip statistics for samples in Figs. 5.7 and 5.8. n = number of slip steps analysed, $\bar{s}$ = average slip step height, $\bar{d}$ = average perpendicular slip line spacing, r = ratio of slip step height divided by slip step spacing, H = sample elongation due to measured slip heights and spacings, ε_{slip} = conversion of H into true strain, Defmn. Band = deformation band. For specific calculations see Appendix B.

In Fig. 5.7 (a) there were 20 slip steps on one diagonal, but only 6 on the other. These 6 steps had much larger heights, but still did not produce an equivalent strain. A second AFM scan of the same sample in an adjacent region was analysed in the same way (Fig. 5.7b). and again it was found that many more slip lines were evident on one system than the other. However, even though the average height and spacing of the slip steps were different on each system, the strain accommodation on both was the same. These results indicate the inhomogenous nature of deformation after very small reductions, and also show that the magnitude of shear on a given slip system is not constant, even at the very early stages of deformation.

This analysis was repeated in a sample deformed to a strain of 0.2 in two areas, one within a deformation band and the other in the centre of the sample (Figs. 5.8 and 5.9). The details of this analysis are included in Table 5.2. It was found that many more slip steps were produced on one system than another, but these systems accommodated approximately the same strain. A similar analysis within the deformation band showed that the spacings and heights of slip steps are more regular within deformation bands than in the rest of the sample. For a deformation band to accommodate the same amount of slip as the bulk of the sample whilst operating half the number of systems, these must either slip by twice the magnitude, or with half the spacing of those in the bulk. The measured distance between slip steps in the deformation band was actually found to be smaller than in the bulk, but the slip heights were approximately the same (Fig. 5.9).

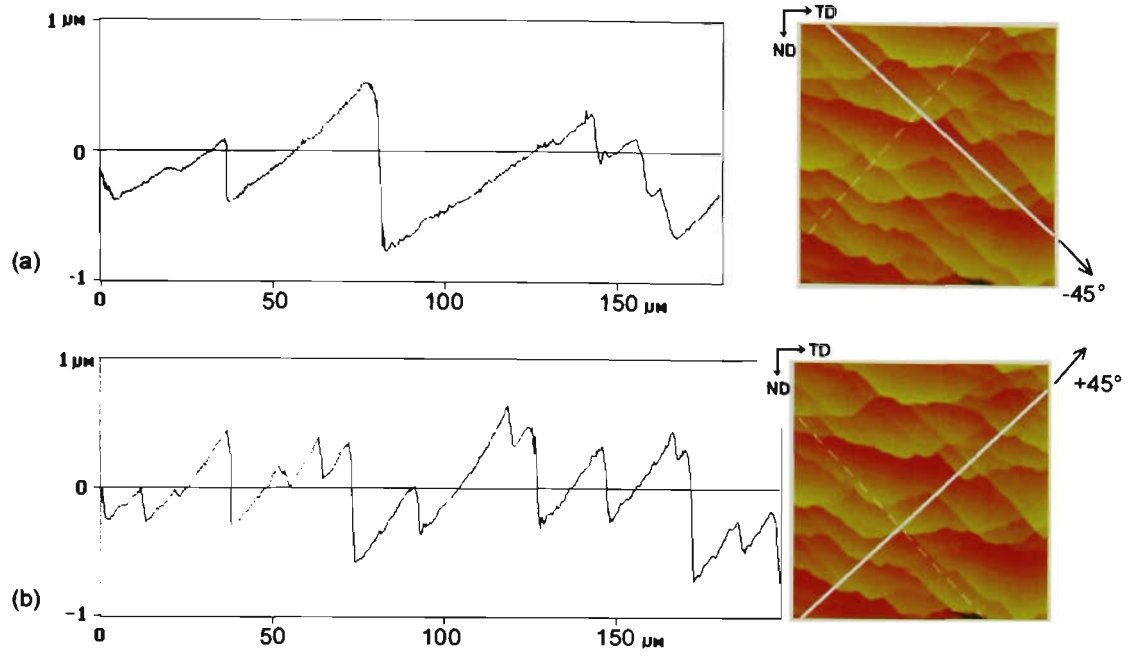

Figure 5.8 AFM surface height profile of slip step steps at (a) -45° and (b) +45° in a Cube oriented crystal deformed to a strain of 0.2.

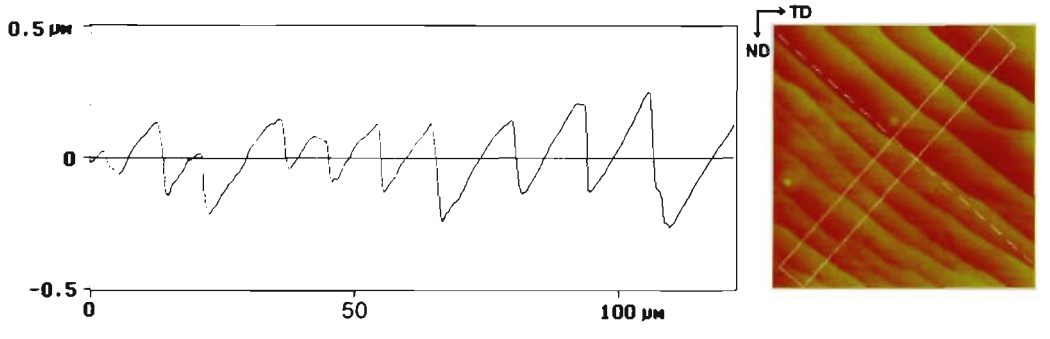

Figure 5.9 AFM surface height profile within a transition band in a Cube oriented crystal deformed to a strain of 0.2.

After a strain of 0.7, some regions showed regular slip lines, whereas other regions showed a "surface rumpling" effect with no clearly defined slip lines. Where deformation bands were evident, the slip steps in adjacent bands were oppositely aligned as shown in Fig. 5.10. The region between these opposite bands is also shown, and corresponds to a transition band. Transition bands are traditionally thought to be areas of high energy with a high dislocation density[11]. This implies the regions

undergo large deformation, possibly more than the surrounding matrix. However, the surface topography shows that deformation does not occur through heterogeneous intense slip, but may occur by more homogenous densely spaced slip lines. Some qualitative evidence of this mechanism was found using higher magnification AFM within transition band regions which showed densely spaced fine slip lines together with regions exhibiting course slip steps (Fig. 5.11). This was evident in samples deformed to strains at and above 0.7.

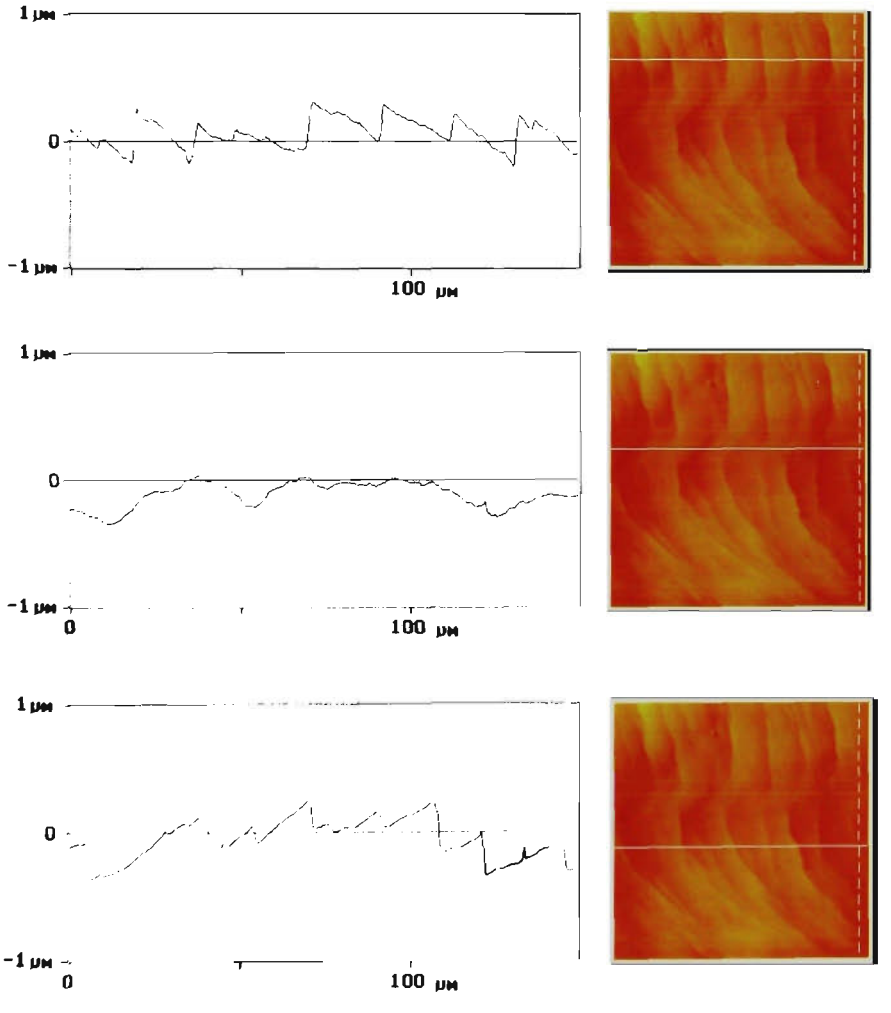

Figure 5.10 AFM surface height profile of slip steps in the ND of a Cube oriented crystal deformed to a strain of 0.7. Note 90° rotation of micrograph with respect to Figs. 5.5 – 5.9.

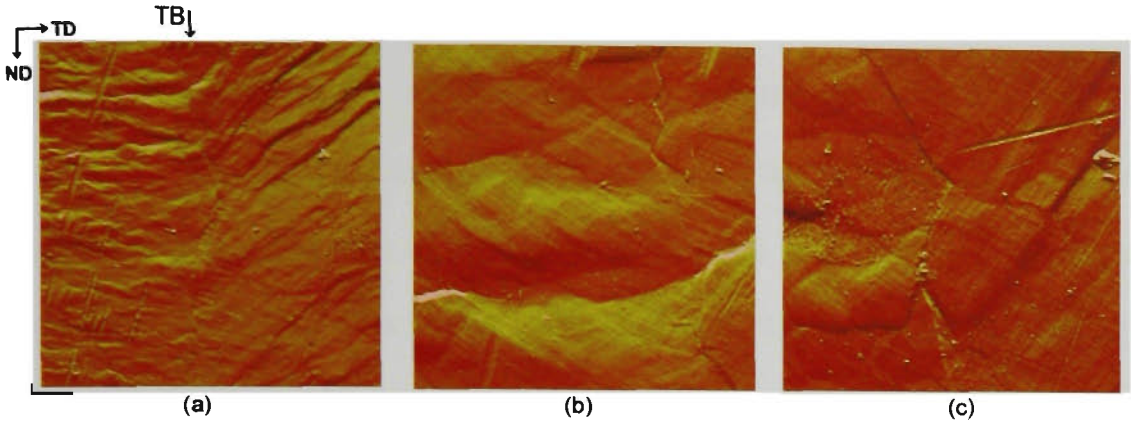

Figure 5.11 AFM deflection imaging of a transition band region in a Cube oriented crystal deformed to a strain of 0.7. Image (a) = 50 μm x 50 μm, (b) and (c) =10 μm x 10 μm. TB = transition band.

Deformation of Cube oriented crystals to a strain of 1.2 did not yield clearly defined deformation bands. However, there were some regions in which some surface topography was evident. AFM analysis showed these regions to be complex surface features associated with transition bands. These transition regions were evident for a number of reasons: they deform to produce different surface topography on either side, and the division between bands often comprised a sharp change in surface height (Fig. 5.12a). This behaviour is remarkably similar to that exhibited by grain boundaries in polycrystalline metals.

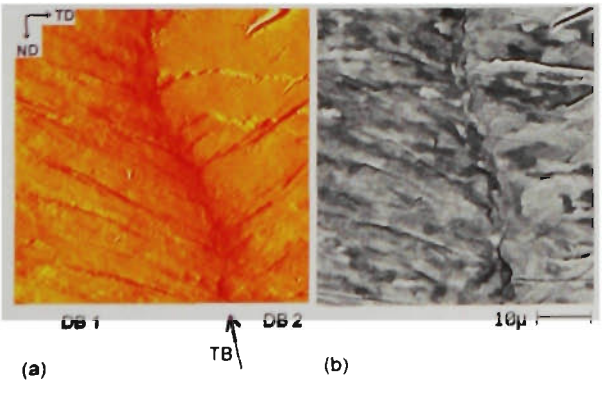

Figure 5.12 (a) AFM deflection image of two deformation bands (DB 1 and DB 2) separated by a transition band (TB); (b) SEM ECC micrograph of same region as (a) in a Cube oriented crystal deformed to a strain of 1.2.

Since the ND-TD face of samples were electro-polished prior to final deformation, it was possible to view the microstructure using ECC with the slip lines also visible. This allowed easy recognition of transition bands, and the slip lines could be correlated to the microstructure. An example of this analysis is shown in Fig. 5.12b. The surface topography has been analysed using both AFM and ECC of the same region. The diffuse substructure is aligned parallel with the slip lines in the first deformation band (DB1), and the transition region is composed of smaller subgrains than the deformation bands. At lower strains, the substructure was not well defined within deformation bands, but was more defined in transition bands (Fig. 5.13). Subgrains were observed to be elongated along the length of transition bands, and lie between regions of differing slip behaviour. The elongation of discrete subgrains is particularly evident in Fig. 5.13c, which shows that the substructure within deformation bands is aligned parallel to the slip traces.

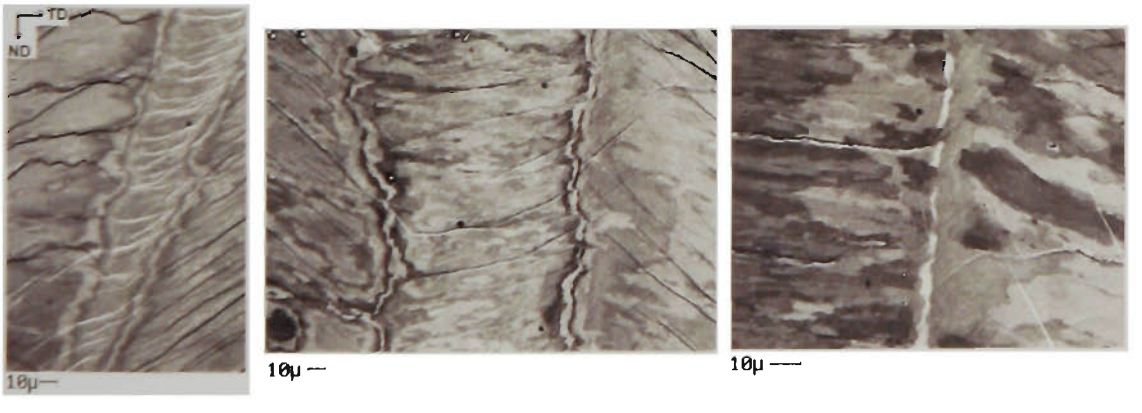

(a) (b) (c)

Figure 5.13 SEM ECC micrographs of the microstructure and slip pattern in transition band regions in a Cube oriented crystal deformed to a strain of 0.7.

5.3 Hot Deformed Texture and Microstructure

Flow curves were obtained during deformation of the Cube oriented crystals, and these are detailed in Appendix C. All stress-strain calculations were carried out using instantaneous area calculations to account for the changing length of the samples during deformation. The stress increased with strain and peaked at the completion of deformation. This result is consistent with the stress-strain data published by Maurice and Driver for Cube oriented crystals[18].

Examples of the microstructure examined using ECC are shown in Fig. 5.14. This investigation showed that many samples deformed at or above 200°C were partially or fully recrystallised (Table 5.3), and these regions were omitted from the deformation texture analysis. The as-deformed state consisted of a substructure that became better defined at higher deformation temperatures. Following deformation at 200°C, subgrains were elongated, and at higher deformation temperatures the subgrains became more equiaxed. Deformation banding was evident up to deformation temperatures of 300°C, but these bands were very small, did not span the sample length, and were not parallel to the ND as was observed at room temperature. At and above 400°C there was no evidence of deformation banding in either the texture analysis or microstructural features.

(a) (b) (c)

Figure 5.14 SEM ECC of Cube oriented crystals deformed at (a) 25°C, (b) 200°C, and (c) 500°C at $50s^{-1}$ to a strain of 1.0. Note the higher magnification of (a).

Since extensive recrystallisation occurred in certain samples, accurate determination of the deformation texture was possible only through EBSD, and the results are summarised in Table 5.3. An example of the hot deformed texture and microstructure measured using EBSD is shown in Fig. 5.15. There are two features to the microstructure, one large recrystallised grain and a coarse substructure. It is noteworthy that the orientation of the recrystallised grain lies close to the deformation texture. In general, the orientation of recrystallised grains present in the as-deformed state were close to that of the deformation texture.

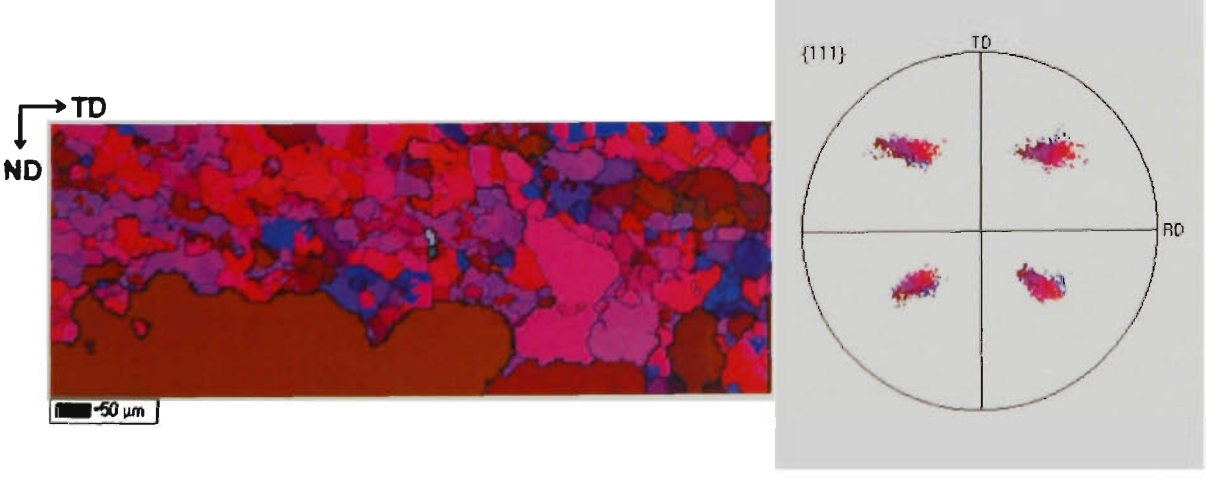

Figure 5.15 EBSD analysis of hot deformed microstructure and texture in a Cube oriented crystal deformed at 500°C at a strain rate of $5s^{-1}$ to a strain of 1.0.

Temp. (°C)	Strain rate	Strain	Ln Z *	Subgrain size	% rex.**	Cube tex.#
25	50 s^{-1}	1.0	66.9	2 μm	0	18 %
200	50 s^{-1}	1.0	43.6	5.5 μm	28	35 %
300	50 s^{-1}	1.0	36.7	3 μm	0	47 %
400	50 s^{-1}	1.0	31.8	10 μm	80	89 %
500	50 s^{-1}	1.0	28.2	22 μm	85	87 %
600	50 s^{-1}	1.0	25.4	-	100	-
500	5 s^{-1}	1.0	25.9	20 μm	55	87 %
500	0.5 s^{-1}	1.0	23.6	32 μm	45	88 %
500	0.05 s^{-1}	1.0	21.3	63 μm	83	95 %
500	0.005 s^{-1}	1.0	19.0	-	100	-

Table 5.3 Details of the as-deformed microstructure and texture of hot deformed Cube crystals. *Activation energy, Q = 156 kJ/mol. (Ref. [39]) ** % rex. = % recrystallised. #Cube tex. = percentage of unrecrystallised material within 15° of ideal Cube orientation measured using EBSD.

5.4 Post-Deformation Annealing Behaviour

5.4.1 Cold Deformed and Annealed

The recrystallisation kinetics and heat treatment for each cold deformed and annealed sample are detailed in Table 5.4. In general, very few grains nucleated and these grew very large. Recrystallisation occurred in clusters, and there was a tendency for anisotropic grain shape in partially recrystallised samples (Fig. 5.16). Where these elongated grains intersect the surface, small pockets of as-deformed material are retained within these partially recrystallised clusters. These retained pockets of

unrecrystallised material were not found to have a significant regularity or consistency in behaviour, and are consumed by further recrystallisation. After complete recrystallisation, the grains reverted to an equiaxed shape (Fig. 5.17). The recrystallisation textures were generally random, with no significant portion of the Cube texture was detected over the range of strains investigated.

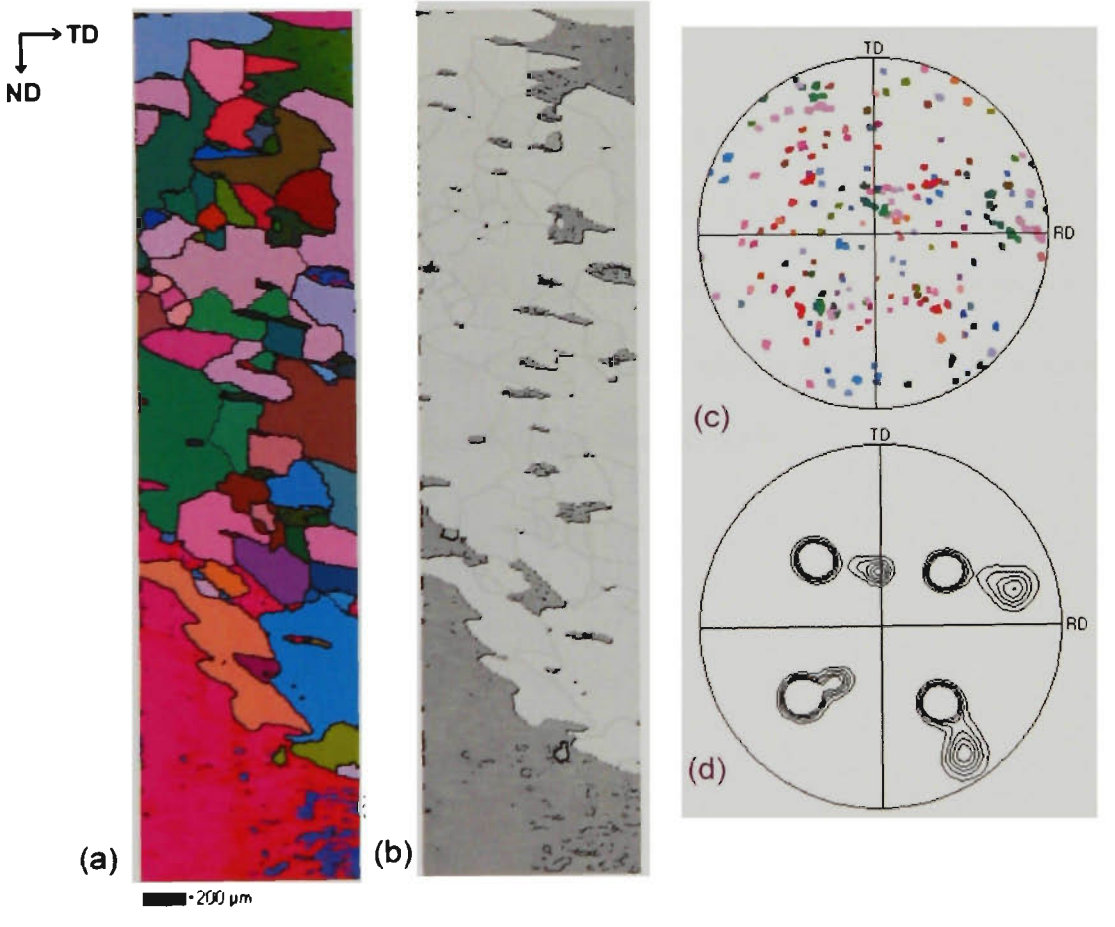

Figure 5.16 EBSD analysis of Cube oriented crystal deformed to a strain of 0.7 and annealed for 4 hours at 300°C. (a) All Euler orientation map and (c) corresponding (111) pole figure of recrystallised grains only. (b) Orientation map with deformed regions shaded dark grey and (d) corresponding (111) pole figure of as-deformed regions only.

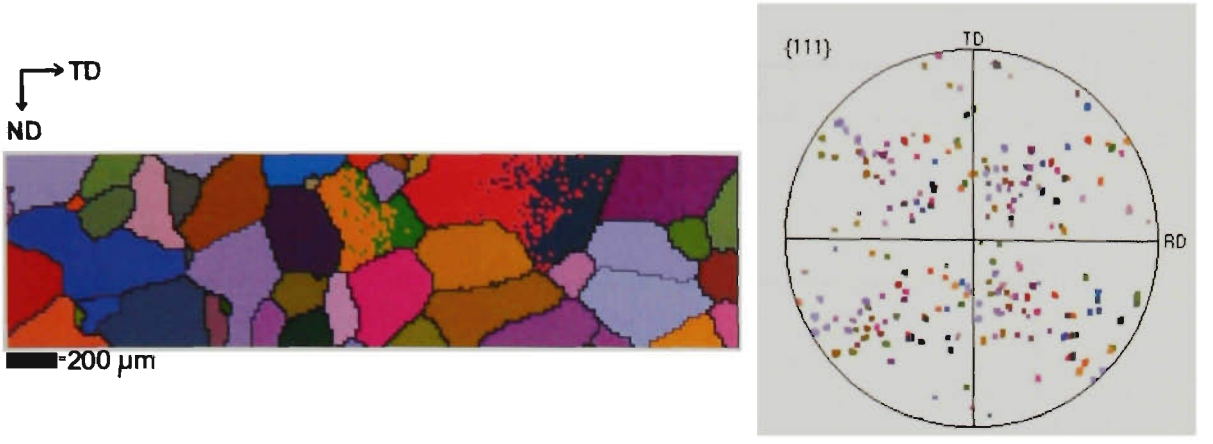

Figure 5.17 EBSD orientation map and (111) pole figure of the recrystallised microstructure of a Cube oriented crystal cold deformed to a strain of 1.2 and annealed for 2 hours at 300°C

Of interest in Table 5.4 is one particularly anomalous result. The sample deformed to a strain of 0.1 did not recrystallise after heat treatment at 400°C, but showed 15% recrystallised after 2 hours at 300°C. Furthermore, after the same heat treatment the sample deformed to the higher strain of 0.4 did not recrystallise either. This unusual behaviour may be the result of artificial surface nucleation[77].

Strain	Heat Treatment	% Recrystallised	Grain size
0.1	2 hours 200°C	0	-
0.4	2 hours 200°C	0	-
0.7	2 hours 200°C	0	-
0.1	½ hour 300°C	0	-
0.4	½ hour 300°C	0	-
0.7	½ hour 300°C	0	-
0.1	2 hours 300°C	15	120 μm
0.4	2 hours 300°C	0	-
0.7	2 hours 300°C	15	196 μm
1.2	2 hours 300°C	100	310 μm
0.1	4 hour 300°C	0	-
0.4	4 hour 300°C	12	300 μm
0.7	4 hour 300°C	45	230 μm
0.1	½ hour 400°C	0	-
0.4	½ hour 400°C	100	1700 μm
0.7	½ hour 400°C	100	1450 μm
1.2	½ hour 400°C	100	518 μm
0.1	2 hour 400°C	0	-

Table 5.4 Details of the recrystallisation behaviour for cold deformed Cube oriented crystals.

5.4.2 Hot Deformed and Annealed

The recrystallisation kinetics and heat treatment for each hot deformed and annealed sample are detailed in Table 5.5. The recrystallisation behaviour was inhomogenous, showing both clusters of small recrystallised grains with orientations close to those in the deformation texture, as well as some large grains which were highly misoriented from the deformed state. The recrystallisation texture was often similar to the deformation texture (Fig. 5.18).

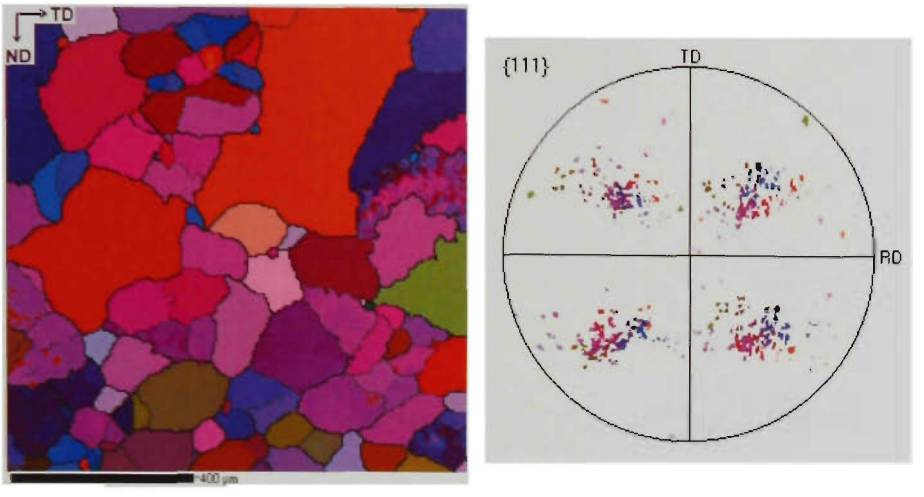

Figure 5.18 EBSD orientation map and (111) pole figure for a Cube crystal deformed at 300°C to a strain of 1.0 at $50s^{-1}$ and annealed for 4 hrs at 300°C.

Transition bands are often considered features favourable for nucleation, but these were found to be retained in the microstructure after annealing, ie, they were not the first places to be consumed by the recrystallisation process (Fig. 5.19). The most notable feature of the interaction between deformation bands and the recrystallisation process is the confinement of large growing recrystallised grains between adjacent transition bands (Fig. 5.19), possibly due to the formation of low mobility boundaries. EBSD revealed only one possible example of transition band nucleation, and this is shown in Fig. 5.20. This nucleus probably grew from the transition band region because it is close in orientation to the transition band.

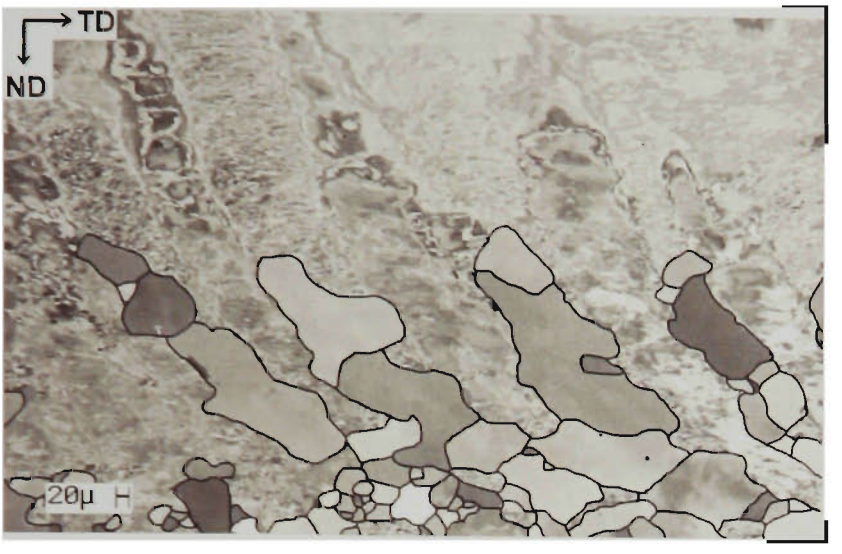

Figure 5.19 SEM ECC of deformation banding in a Cube oriented crystal deformed at 300°C and annealed for 15 minutes at 300°C. Recrystallised grains are outlined for clarity

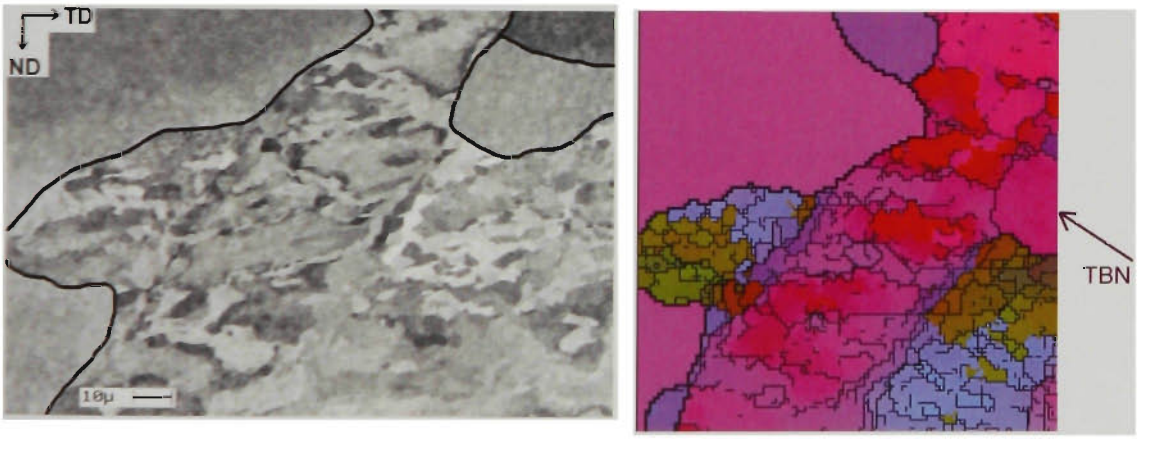

(a) (b)

Figure 5.20 (a) SEM ECC and (b) EBSD all Euler orientation map of identical region of sample deformed at 200°C and annealed for 15 minutes at 300°C. TBN = transition band nucleus. Recrystallised grains in (a) have been outlined for clarity.

Strain	Deformation Temperature	Heat Treatment	% Recrystallised	Recrystallised grain size
1.0	200°C	15 min. 300°C	66 %	450 μm
1.0	300°C	15 min. 300°C	50 %	32 μm
1.0	400°C	15 min. 300°C	65 %	35 μm
1.0	300°C	4 hour 300°C	78 %	159 μm
1.0	400°C	4 hour 300°C	75%	240 μm

Table 5.5 Details of the recrystallisation behaviour of hot deformed Cube oriented crystals.

6 Results – (011)[01 $\bar{1}$] Orientation

6.1 Deformation Behaviour

Samples of the (011)[01 $\bar{1}$] orientation were deformed to strains of 0.5 and 1.0 at a strain rate of 0.01 s^{-1} at temperatures of 25, 200 and 300°C. Microstructural development was examined using ECC, and no recrystallisation of any sample was found to occur during quenching. Hot deformed samples underwent dynamic recovery, resulting in a relatively large subgrain size which is detailed in Table 6.1. Flow curves were obtained for each sample and the true stress-true strain curves plotted for each using instantaneous area calculations (Appendix D).

Strain	Strain rate	Temperature	Subgrain size	σ_f (MPa)
0.5	0.01 s^{-1}	25°C	3 μm	140
0.5	0.01 s^{-1}	200°C	3.7 μm	70
0.5	0.01 s^{-1}	300°C	7.5 μm	37
1	0.01 s^{-1}	25°C	1.4 μm	150
1	0.01 s^{-1}	200°C	4 μm	71
1	0.01 s^{-1}	300°C	8 μm	35

Table 6.1 Details of experimental conditions, resultant subgrain size and steady state flow stress (σ_f) for (011)[01 $\bar{1}$] crystals.

The deformation behaviour of this orientation is complex, and as a result the texture and microstructure of each sample is examined individually in the following sections.

6.1.1 Texture and Microstructure at T_{def} = 25°C

Results of the textural analysis in the as-deformed state by XRD and EBSD are detailed in Fig. 6.1. At a true strain of 0.5 the crystal developed only a small amount of orientation spread, and at a strain of 1.0 was slightly more spread about the TD. No deformation bands were detected by either ECC or EBSD.

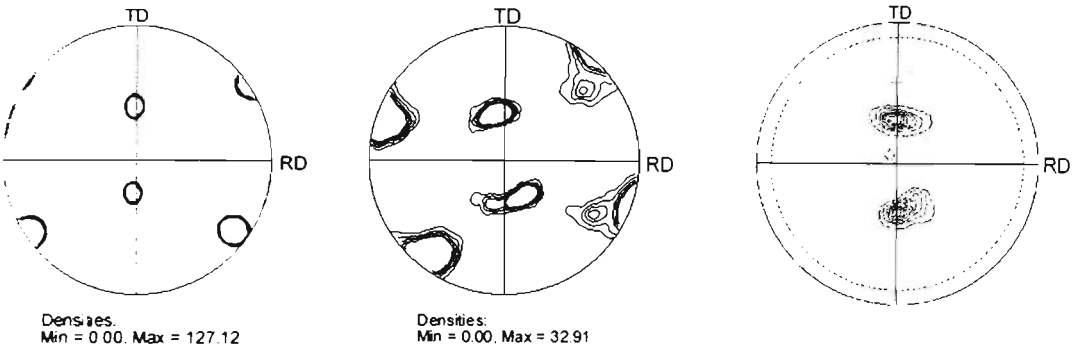

Figure 6.1 (111) pole figures of the deformation texture of (011)[01 $\bar{1}$] oriented crystals deformed at room temperature to the strains indicated, measured using (a, b) EBSD and (c) XRD.

6.1.2 Texture and Microstructure at T_{def} = 200°C

An example of the typical substructure developed after a strain of 0.5 at 200°C is shown in Fig. 6.2. No deformation bands were detected in the ND-TD plane, leading to a homogenous structure whose deformation texture remained relatively clustered. However, after a strain of 0.5, the entire crystal did rotate ~ 15° about the ND (Fig. 6.3).

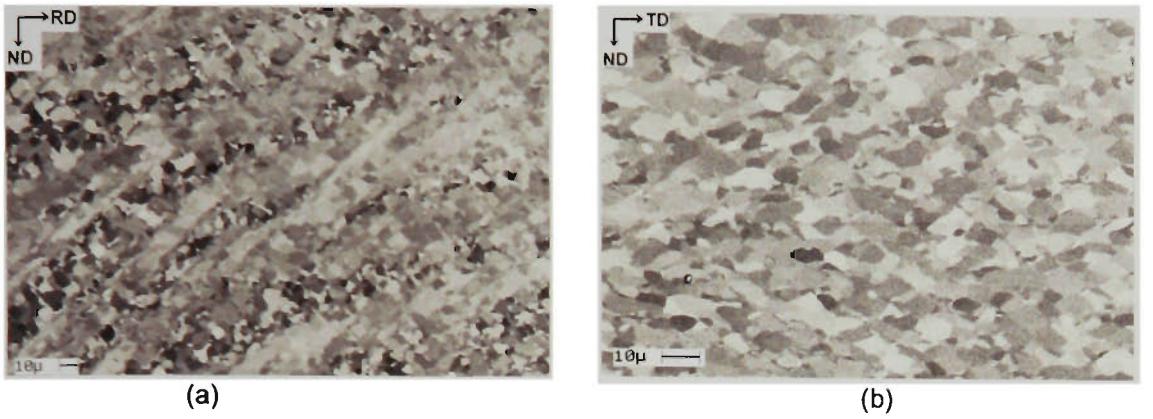

(a) (b)

Figure 6.2 SEM ECC of microstructure of (011)[01 $\bar{1}$] oriented crystal deformed at 200°C to a strain of 1.0. Note higher magnification in (b).

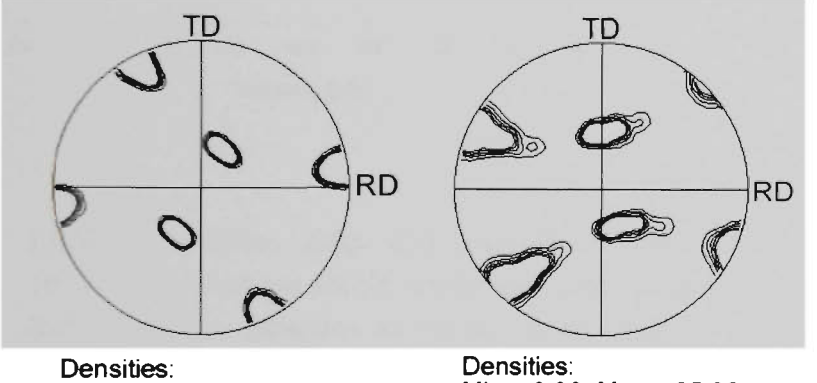

Figure 6.3 EBSD texture analysis for (011)[01 $\bar{1}$] oriented crystal deformed at 200°C to a strain of 0.5 and 1.0 as indicated.

EBSD mapping of the ND-TD plane revealed that some regions of the sample contained cyclic orientation gradients, and the crystallographic rotation between these layers was ~10° about the TD. The EBSD orientation map in Fig. 6.4 shows the diffuse nature of these layers.

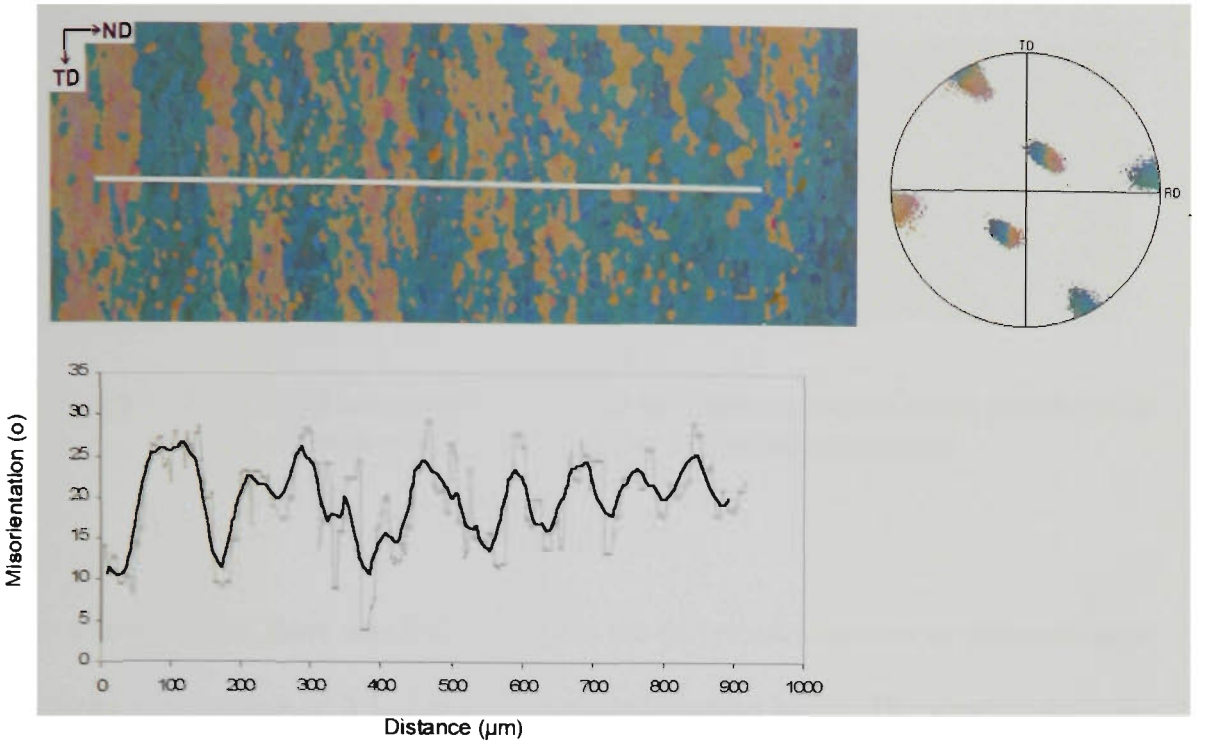

Figure 6.4 EBSD orientation map and cumulative misorientation profile for (011)[01 $\bar{1}$] oriented single crystal deformed to a strain of 0.5 at 200°C. Bold black line indicates an average misorientation profile from the raw data shown in grey.

EBSD analysis in the ND-RD plane showed that, on a finer scale, samples contained parallel bands of moderately high angle boundaries running at ~±45° to the rolling plane. The nature of these boundaries is not uniform along the sample length, in some regions the boundaries running at 45° dominate, and in other regions those at -45° dominate (Fig. 6.5). Intersection of these bands with the ND-TD plane produced the diffuse layered structure of Fig. 6.4.

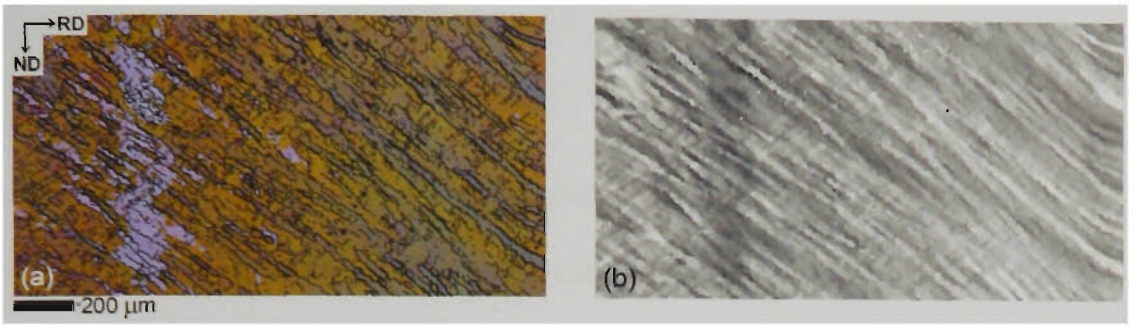

Figure 6.5 High angle boundaries on the ND-RD plane measured using EBSD (a) all Euler orientation mapping (b) Euler 3 orientation mapping.

After a strain of 1.0, there was little change in the deformation texture or microstructure compared with a strain of 0.5. There were no deformation bands. The magnitude of the cyclic misorientation gradients parallel to the ND are enhanced, up to 25°, and have a smaller spacing of 50-100 µm. The subgrain size is virtually unchanged due to the dynamic restoration process.

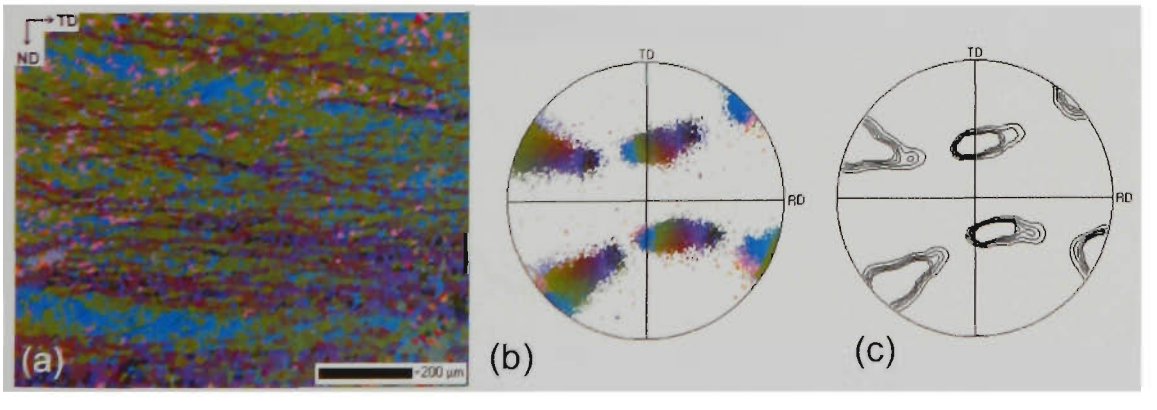

Figure 6.6 (a) EBSD all Euler orientation map and (b,c) (111) pole figures of as-deformed state of (011)[01 $\bar{1}$] oriented crystal deformed to a strain of 1.0 at 200°C.

6.1.3 *Texture and Microstructure at T_{def} = 300°C*

After a strain of 0.5 at 300°C, a regular substructure developed throughout the sample. EBSD analysis revealed a macroscopic break-up of the sample into large bands up to 500 μm wide that lie in the ND-RD plane. Adjacent bands had a complementary orientation, with the axis of rotation being about the ND. Of particular interest is the structure of the region between adjacent bands, which contained a continuous orientation gradient. The subgrains in these regions were not elongated parallel to the bands, as was found in transition bands in the Cube orientation. The orientation gradient between bands was ~0.06°/μm at its maximum (Fig 6.7). A consequence of this feature was an increase in the deformation texture spread of the sample compared to deformation at lower temperatures (Fig.6.8).

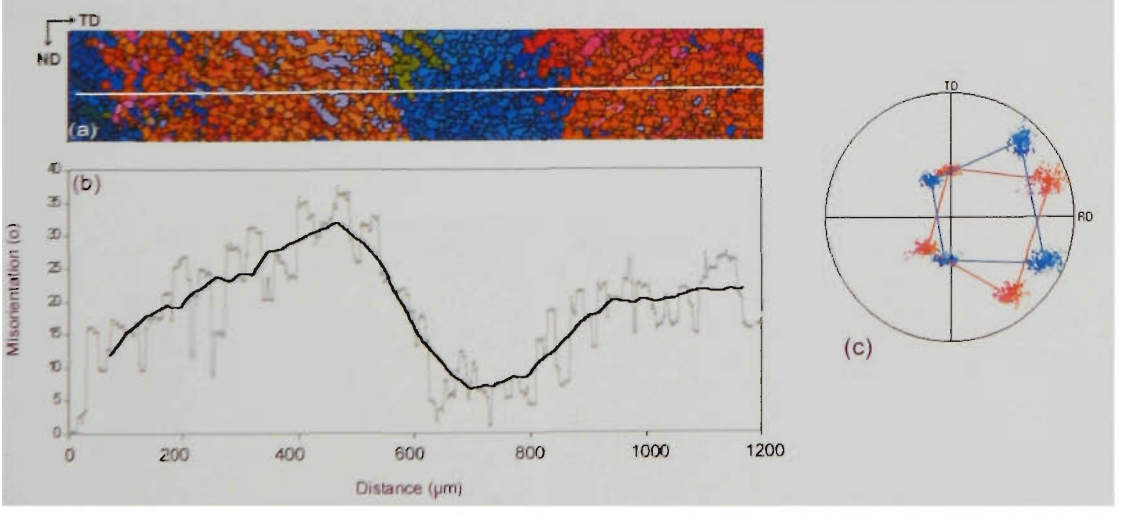

Figure 6.7 (a) EBSD all Euler orientation map (b) cumulative misorientation profile (c) (111) pole figure of (011)[01 $\bar{1}$] oriented crystal deformed to a strain of 0.5 at 300°C. The bold black line indicates and average misorientation profile from the raw data shown in grey.

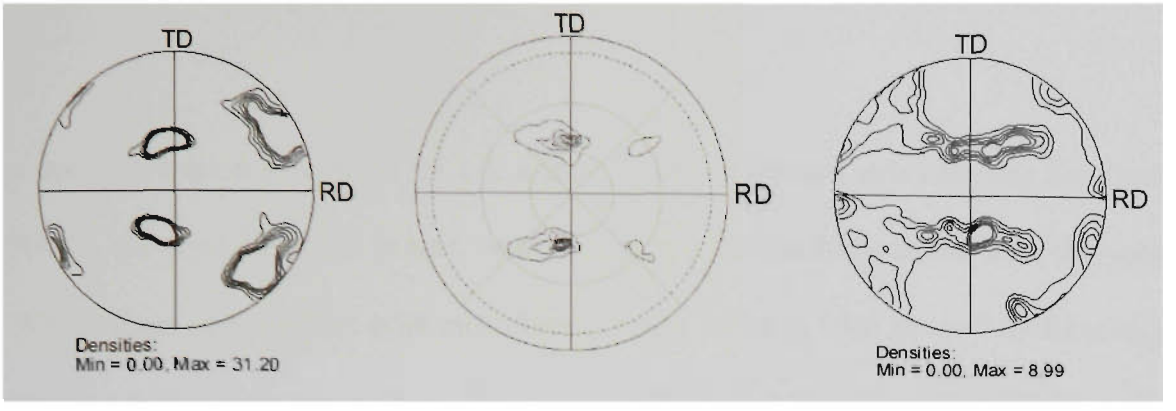

Strain = 0.5 Strain = 0.5 Strain = 1.0

(a) (b) (c)

Figure 6.8 (111) pole figures of deformation texture of (011)[01 $\bar{1}$] oriented crystals deformed at 300°C to the strains indicated using (a) EBSD, (b) XRD and (c) EBSD.

On a finer scale, in the ND-RD plane, samples deformed at 300°C contained the same parallel layers of moderately high angle boundaries running at 45° to the rolling plane, as was found after deformation at 200°C (Fig. 6.9).

(a) (b)

Figure 6.9 (a) Orientation map including grain boundaries and (b) band contrast map of (011)[01 $\bar{1}$]crystal deformed to a strain of 1.0 at 300°C.

After deformation to a strain of 1.0, a more complex banded structure was observed. Firstly, the crystal divided in half, centrally along a section lying in the ND-RD plane. Within these halves there exist more bands which to lie at ~40° to the ND forming a "herring-bone" structure such as described by Ferry and Humphreys[100] (Fig. 6.10). These herring-bone bands are composed of complementary ND rotated texture components, and have a perpendicular spacing of 100 to 250 μm. The orientation gradient between adjacent bands was ~0.25°/μm, and the orientation gradient across the boundary between halves was measured to be approximately the same magnitude as the maximum gradient between the 40° bands. A correlation of texture and microstructure is illustrated in Fig. 6.11.

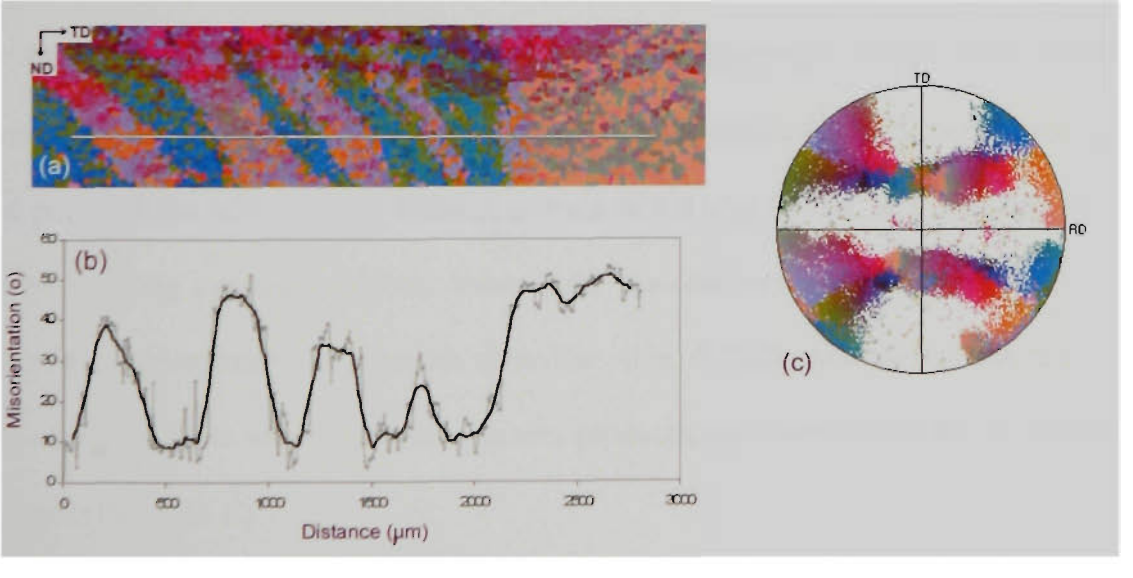

Figure 6.10 (a) EBSD all Euler orientation map, (b) cumulative misorientation profile, and (c) (111) pole figure of (011)[01 $\bar{1}$] oriented crystal deformed to strain of 1.0 at 300°C

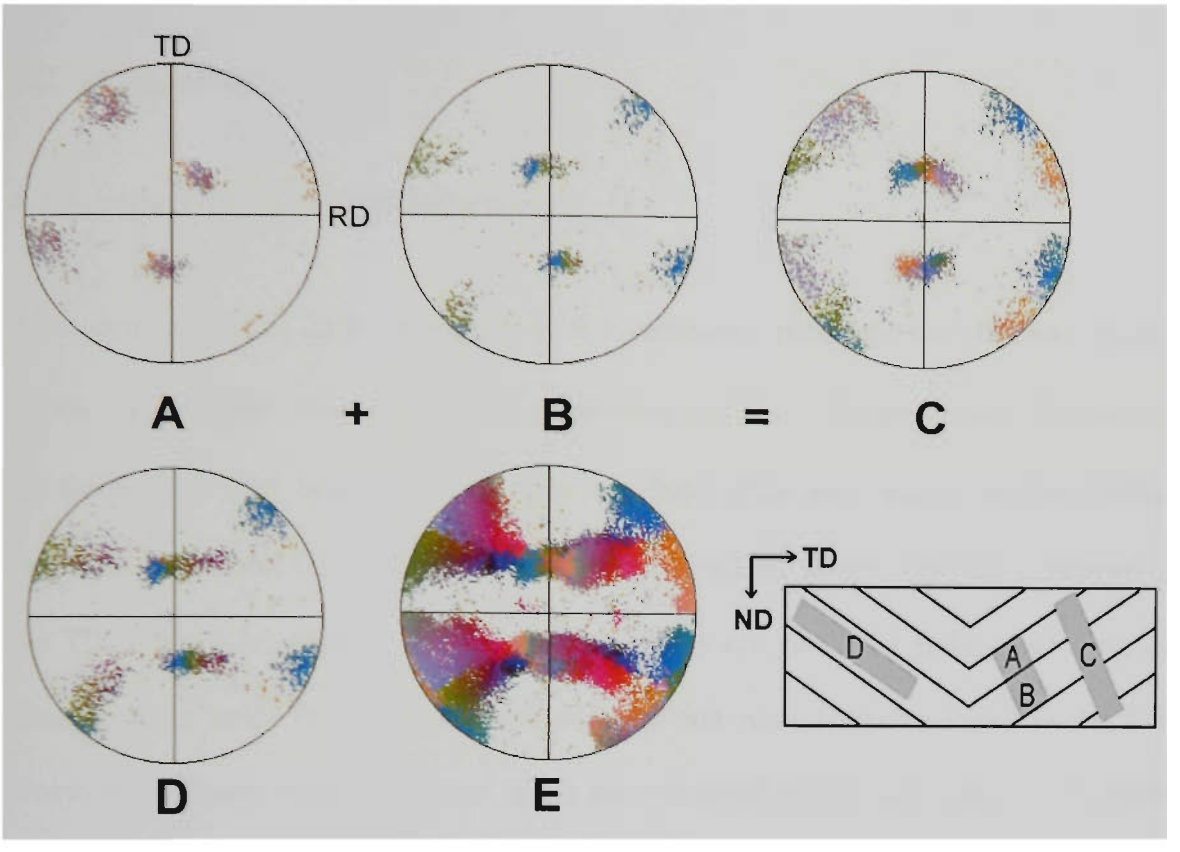

Figure 6.11 Schematic correlation of texture and microstructure in a (011)[01 $\bar{1}$] oriented crystal deformed to a strain of 1.0 at 300°C. All pole figures shown are (111) poles.

The bands that lie at 40° to the ND comprise complementary orientations, whose rotation lies about the ND. Addition of the texture components for each complementary band produces the ND rotations found at a strain of 1.0 (Fig 6.11 A, B, C. Texture of A + B = C). Along the length of these bands there is a continuous rotation about the TD, which is complementary in opposite directions (Fig 6.11D). Addition of the texture components of these microstructural features produces the overall deformation texture observed (Fig. 6.11 E).

6.2 Annealing

6.2.1 Annealing after Cold Deformation

After deformation at 25°C to a strain of 0.5, annealing produced recrystallised grains which grew rapidly, resulting in large grain sizes of up to 1300 μm. After the shortest annealing time of 1 hour at 300°C, only one large grain was present on the surface analysed, and it had a unique shape consisting of parallel fingers extending parallel to the TD (Fig. 6.12a). After 4 hours there were many recrystallised grains, and some of these retained strips of unrecrystallised material that were aligned parallel to the TD. These as-deformed regions spanned many recrystallised grains, and were not deviated by high angle grain boundaries (Fig. 6.12b). After 10 hours annealing the measured recrystallised percentage was slightly lower than after annealing for 4 hours, which indicates the inhomogenous nature of recrystallisation in the samples.

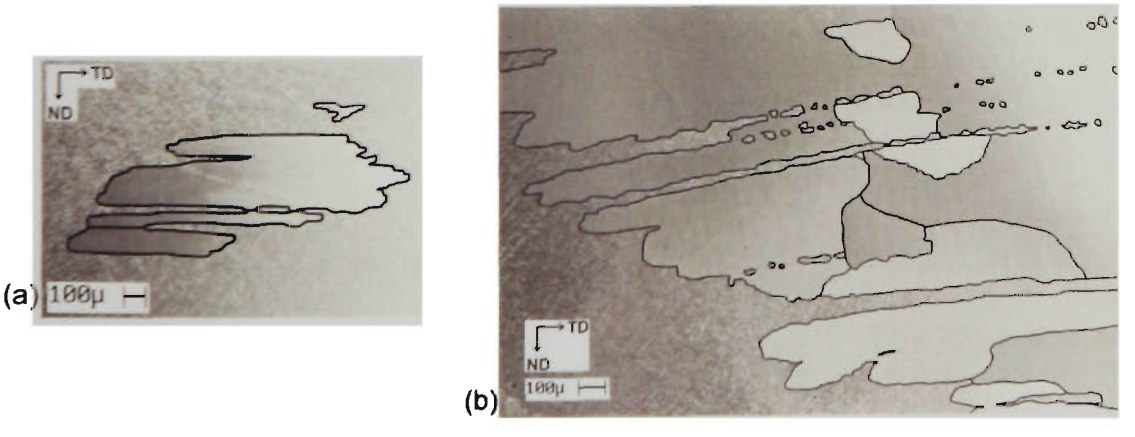

Figure 6.12 ECC micrograph recrystallised grains in a (011)[01 $\bar{1}$] crystal deformed to a strain of 0.5 at 25°C and annealed at 300°C for (a) 1 hour and (b) 10 hours.

The recrystallisation texture after deformation to a strain of 0.5 was found to be random. The recrystallised structure was composed of very few, large grains that were far removed in orientation from the deformed state (Fig. 6.13)

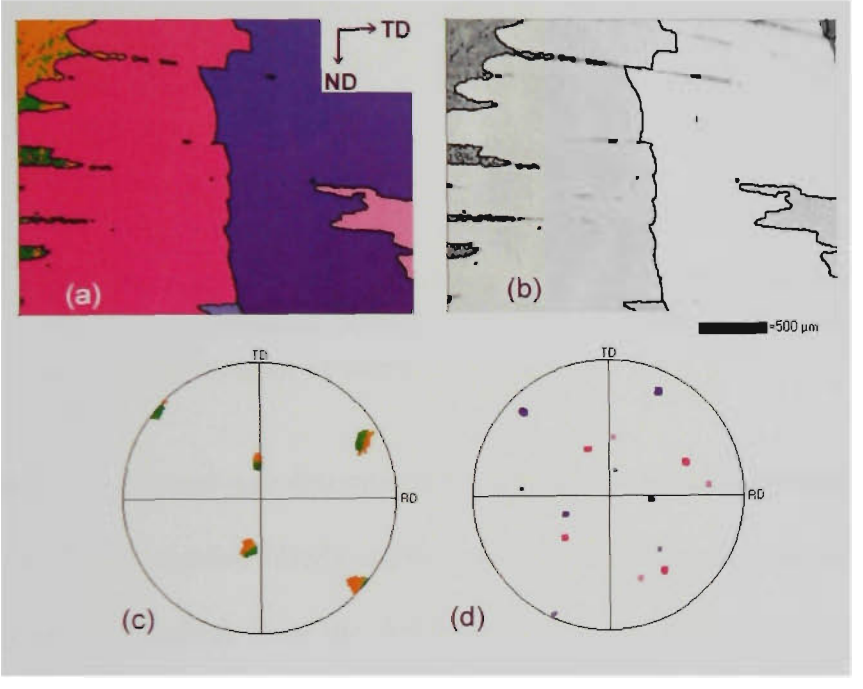

Figure 6.13 EBSD analysis of (011)[01 $\bar{1}$] oriented crystal deformed to strain of 0.5 at 25°C and annealed for 10 hours at 300°C. (a) Orientation map showing all Euler colouring, (b) band contrast map showing deformed regions dark grey and recrystallised grains light grey (c) (111) pole figure of the deformed regions only (d) (111) pole figure of the recrystallised grains only.

After deformation to a strain of 1.0 at 25°C, the kinetics of recrystallisation were markedly faster compared to a strain of 0.5. After annealing for 1 hour the sample was almost fully recrystallised, and had a relatively small grain size of 320 µm. The grains were reasonably equiaxed, but the grain boundaries did not exhibit the usual structure, they were irregular, and the intersection of two growing grains rarely produced a flat grain boundary (Fig. 6.14).

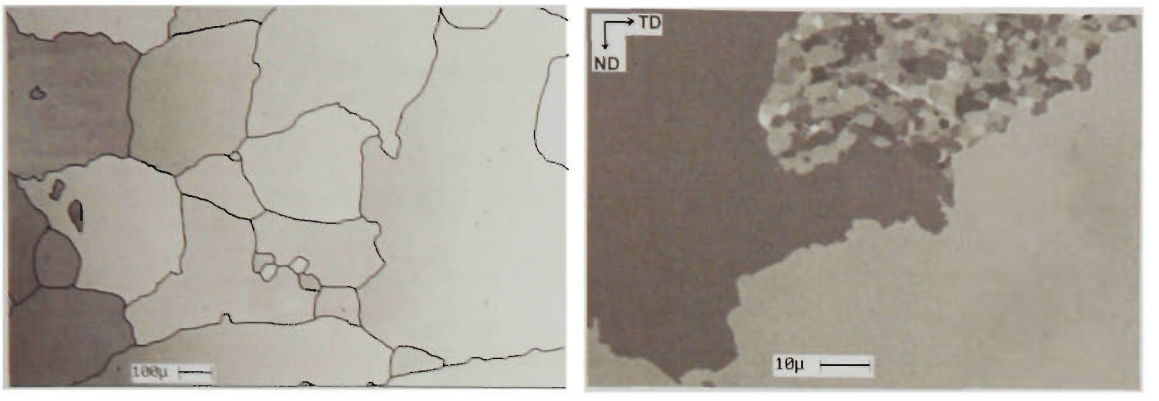

Figure 6.14 ECC micrograph of grain boundaries at two different magnifications in a (011)[01 $\bar{1}$] oriented crystal deformed to a strain of 1.0 at 25°C and annealed for 1 hour at 300°C.

The recrystallisation texture was determined to be roughly spread about the deformation texture (Fig. 6.15b). Extensive EBSD scanning indicated the largest grains in the sample were usually spread furthest from the deformation texture. Clusters of smaller grains had a preferred orientation corresponding to the periphery of the deformation texture, ie, spread ~15° from the starting orientation.

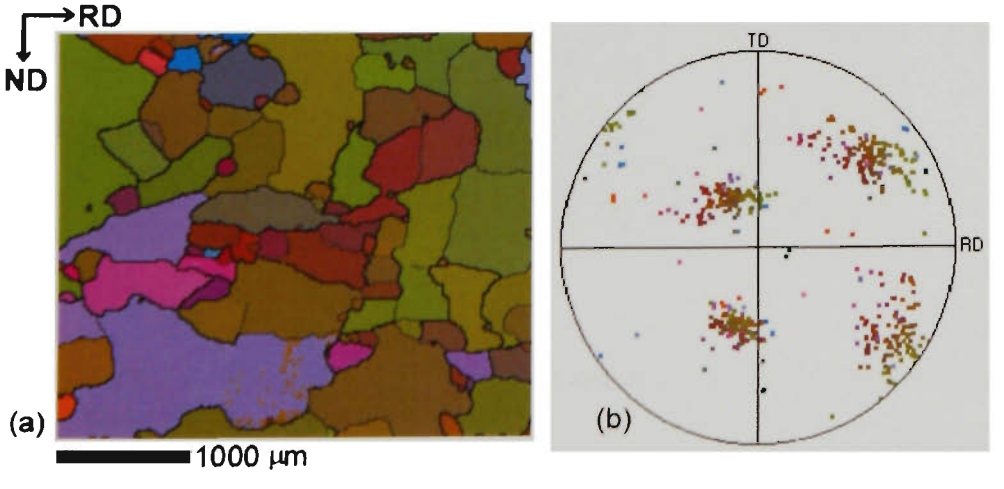

Figure 6.15 (a) EBSD all Euler orientation map and (b) (111) pole figure of (011)[01 $\bar{1}$] oriented single crystal deformed to a strain of 1.0 at 25°C and annealed for 1 hour at 300°C.

6.2.2 Annealing after Hot Deformation to ε = 0.5

The annealing response of samples deformed to a strain of 0.5 at 200 and 300°C was quite similar, and are presented here together. The already well developed subgrains were found to grow by only very small amounts with time at temperature. However, regularly spaced bands of subgrains grew rapidly into what can be described as recrystallised grains (Fig. 6.16). This behaviour was not homogenous across the sample length but occurred in clusters. The recrystallised grains were separated from each other by low angle grain boundaries but usually were separated from the as-deformed structure by high angle grain boundaries (Fig. 6.17).

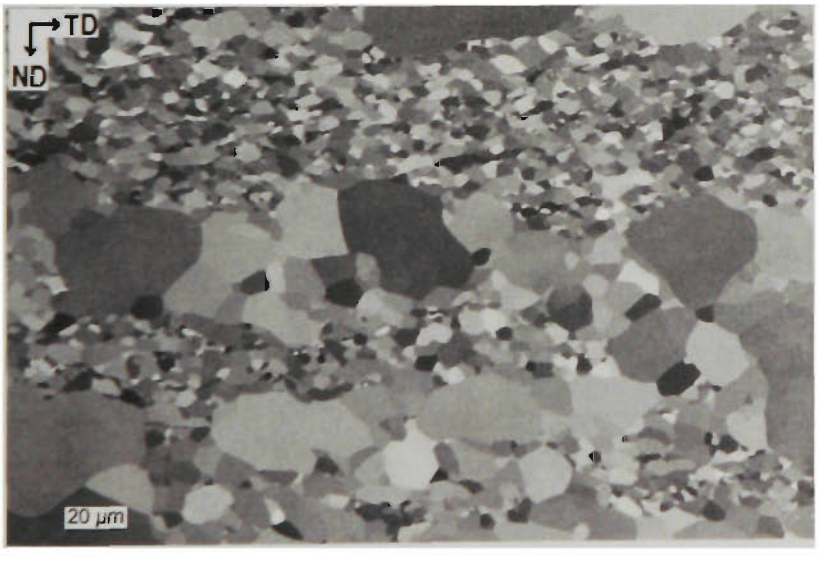

Figure 6.16 SEM ECC of (011)[01$\bar{1}$] crystal deformed at 200°C to a strain of 0.5, annealed for 1 hour at 300°C.

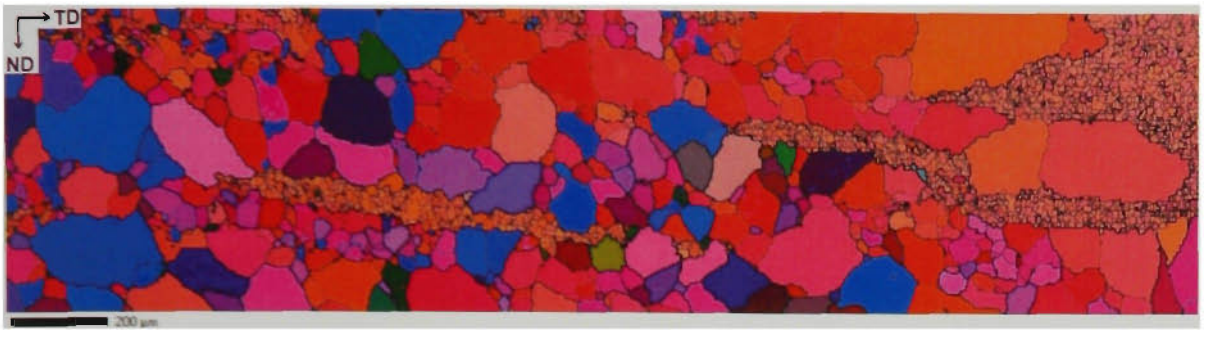

Figure 6.17 EBSD orientation map of (011)[01 $\bar{1}$] oriented crystal deformed at 200°C to a strain of 0.5 and annealed for 1 hour at 300°C.

In partially recrystallised, the bands of recrystallised grains were confined within well defined parallel boundaries, and were separated by bands of as-deformed subgrains (Fig. 6.18). These layers of as-deformed material were retained even after 10 hours annealing, and when analysed in ND-RD sections were found to be columnar or rod shaped (Fig. 6.19) with axis parallel to the TD, and an approximate diameter of 20 – 125 μm. These rods were often several millimetres in length, were not randomly spaced, but arranged regularly into an array in the ND-RD plane which, when sectioned, produced the distinctive bands found in the ND-TD plane of Fig. 6.18. The relationship between these unrecrystallised rods and the deformation geometry is shown schematically in Fig. 6.20. At the periphery of the recrystallised clusters there were usually a few large grains, much larger than at the centre of the recrystallised cluster. Rods of unrecrystallised material were often observed within these large grains also (Fig. 6.19).

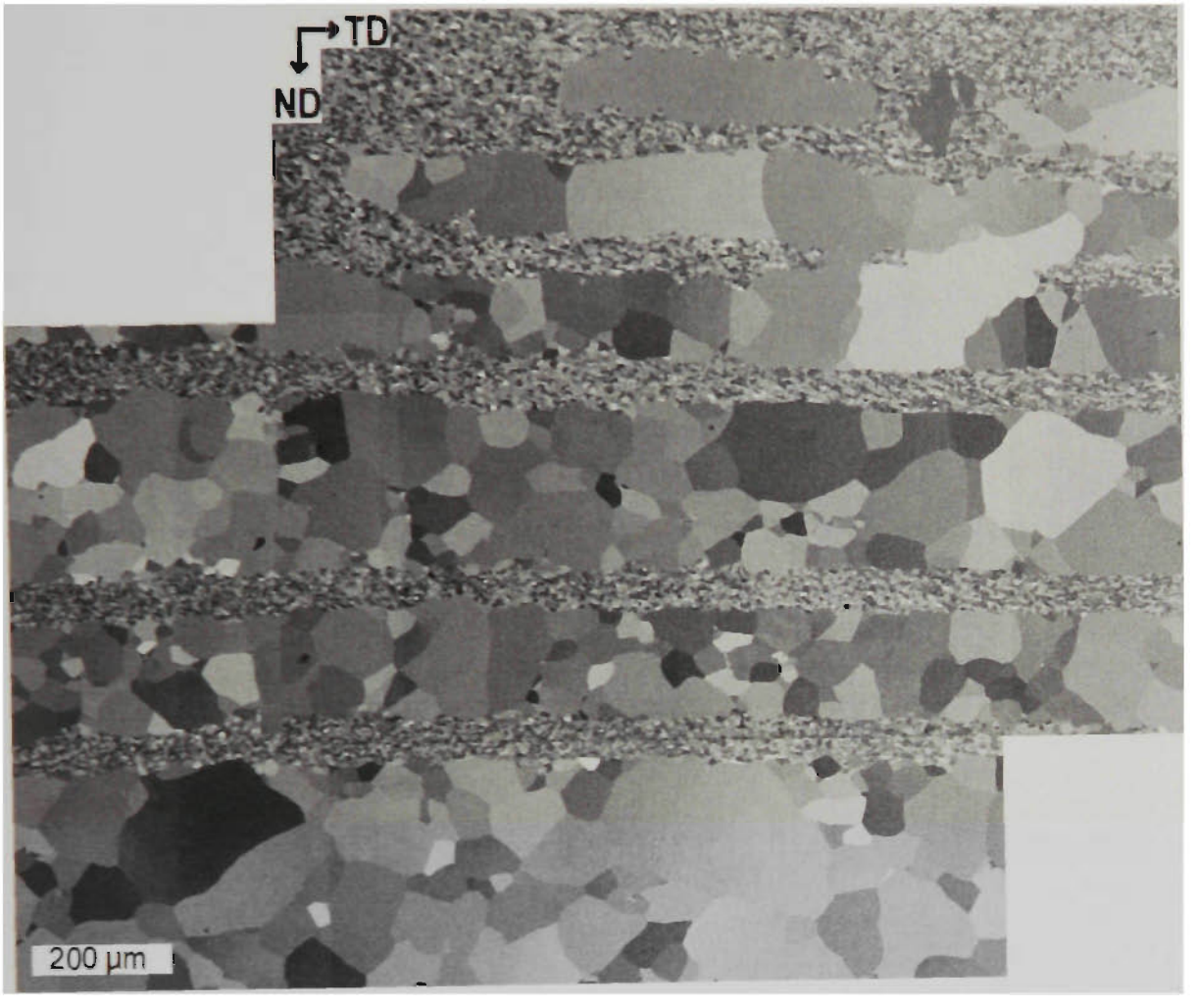

Figure 6.18 ECC micrograph of (011)[01 $\bar{1}$] crystal deformed at 200°C to a strain of 0.5, annealed for 10 hours at 300°C.

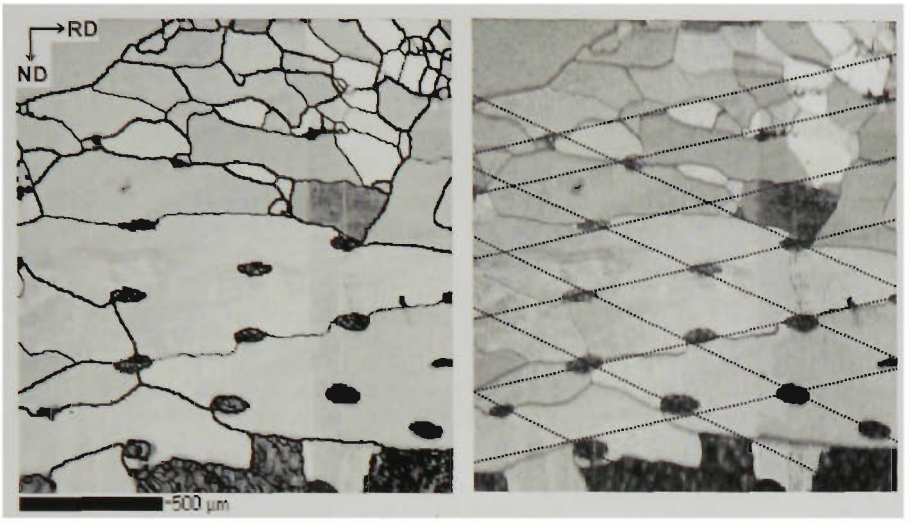

Figure 6.19 EBSD mapping of a (011)[01 $\bar{1}$] crystal deformed to 0.5 at 200°C, annealed for 4 hours at 300°C. Figure (a) is displayed using band contrast mapping, where as-deformed regions appear dark grey, and recrystallised grains appear lighter grey. High angle grain boundaries are shown as bold lines, and low angle grain boundaries as thin black lines. (b) EBSD band contrast map including schematic of array of rods of as-deformed material, with an axis in the TD and aligned in layers at a shallow angle to the RD.

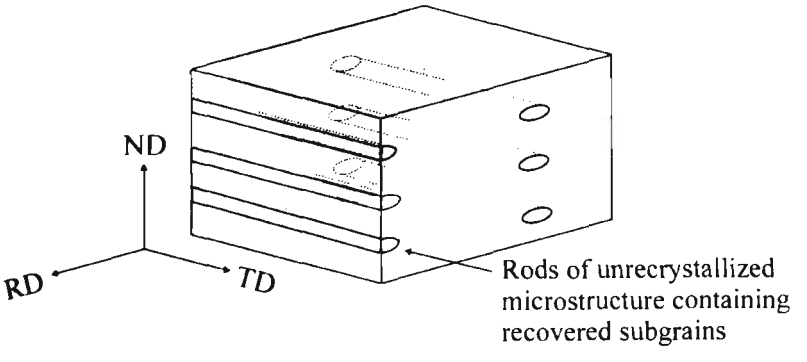

Figure 6.20 Schematic diagram of the relationship between rods of unrecrystallised microstructure and the deformation geometry for (011)[01 $\bar{1}$] oriented crystals deformed to a strain of 0.5 at 200 and 300°C.

Where recrystallised grains grew to impingement, a banded structure was retained in the fully recrystallised regions (Fig. 6.21a). At a strain of 0.5 these bands had a spacing of 200-400 µm. The recrystallisation texture was found to lie within the deformation texture (Fig. 6.21b).

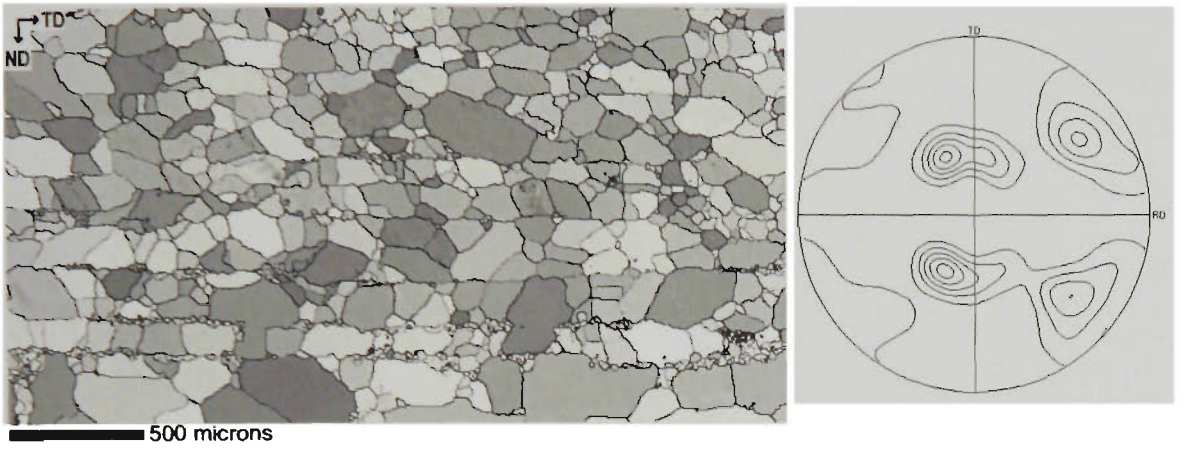

(a) (b)

Figure 6.21 EBSD Euler 3 map and (111) pole figure of recrystallised microstructure of (011)[01 $\bar{1}$] crystal deformed at 300°C to a strain of 0.5, and annealed at 300°C for 4 hours.

6.2.3 Annealing after Hot Deformation to ε = 1.0

After a strain of 1.0, the annealing behaviour of samples deformed at 200°C and 300°C were significantly different, as was their deformation behaviour. After deformation at 200°C to a strain of 1.0, annealing produced prolific nucleation of recrystallisation, usually in diffuse bands parallel to the TD in the ND-TD plane in a similar manner to those described above after a strain of 0.5. The nucleation of recrystallisation was homogenous across the entire length of the sample (Fig. 6.22). Similar to the annealing behaviour of this orientation after a strain of 0.5, there were some regions that resisted recrystallisation, producing the same distinctive banded structure. However, these bands were more closely spaced, being 50-200 μm wide. Again, the as-deformed regions were rod or lath shaped, and arranged regularly in an array as they were after a strain of 0.5. However, their cross-sections were not always circular, but were also observed to be elliptical or almond shaped in the ND-RD section.

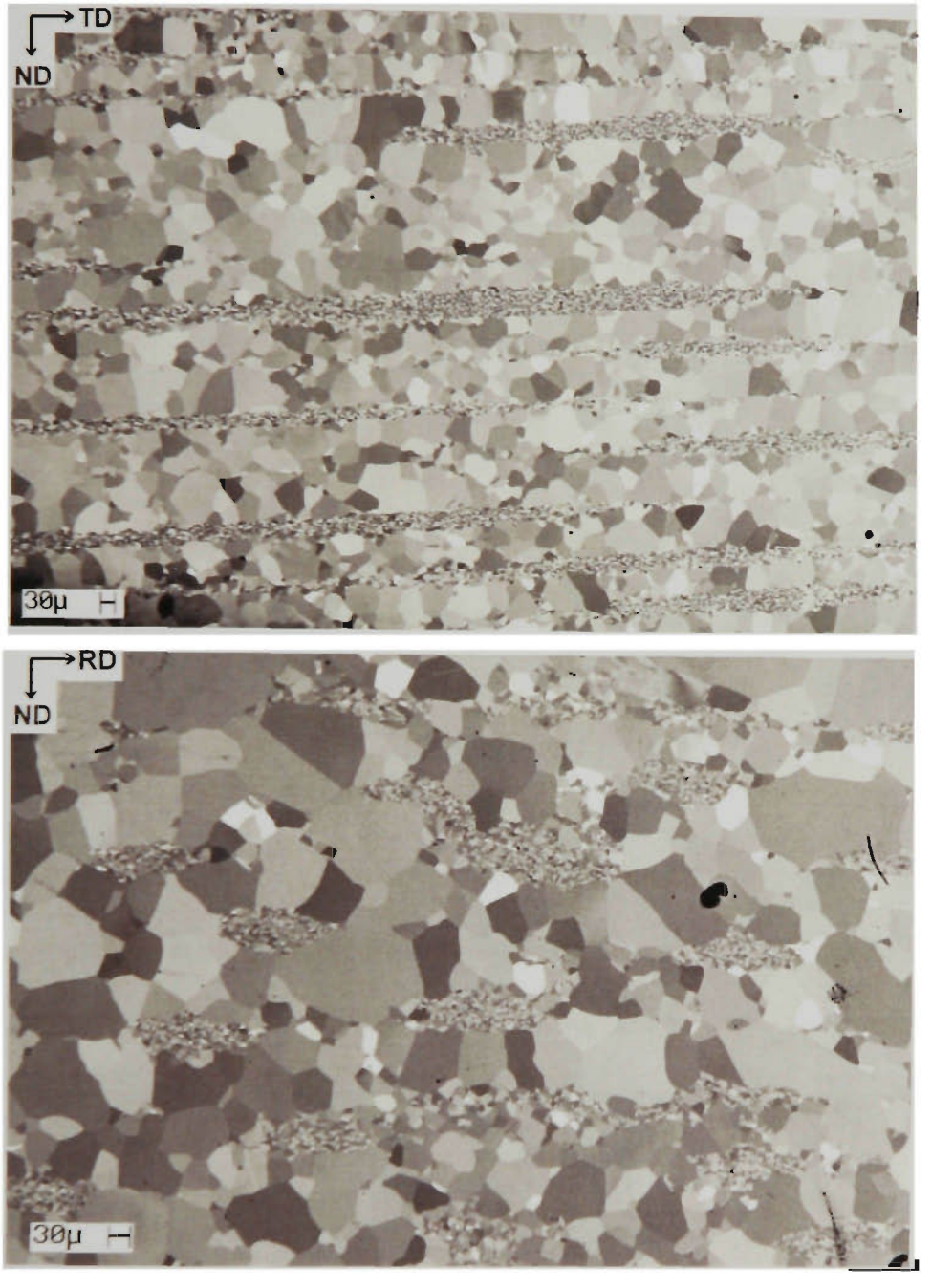

Figure 6.22 ECC micrograph of (011)[01 $\bar{1}$] oriented crystal deformed at 200°C to a strain of 1.0 and annealed for 1 hour at 300°C.

The recrystallisation texture was similar to the deformation texture (Fig. 6.23).

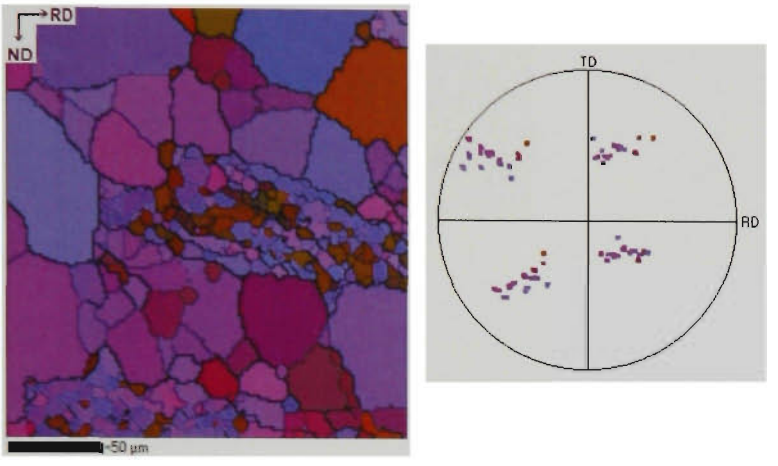

Figure 6.23 Recrystallised microstructure and texture measured using EBSD for a (011)[01 $\bar{1}$] crystal deformed to a strain of 1.0 at 200°C and annealed for 1 hour at 300°C. (111) pole figure shows texture of 20 largest grains in the mapped section.

The recrystallisation behaviour was markedly different after deformation at 300°C, compared to deformation at 200°C. The initial stages of recrystallisation produced very few recrystallised grains, and these were anisotropic in shape, being elongated in the TD and RD. In general these initial grains had orientations that lie within the deformation texture.

Further annealing produced some evidence of the banded microstructure found in samples deformed at 200°C, but this behaviour is not prolific after deformation at 300°C. The recrystallisation texture was similar to the deformation texture (Fig. 6.24).

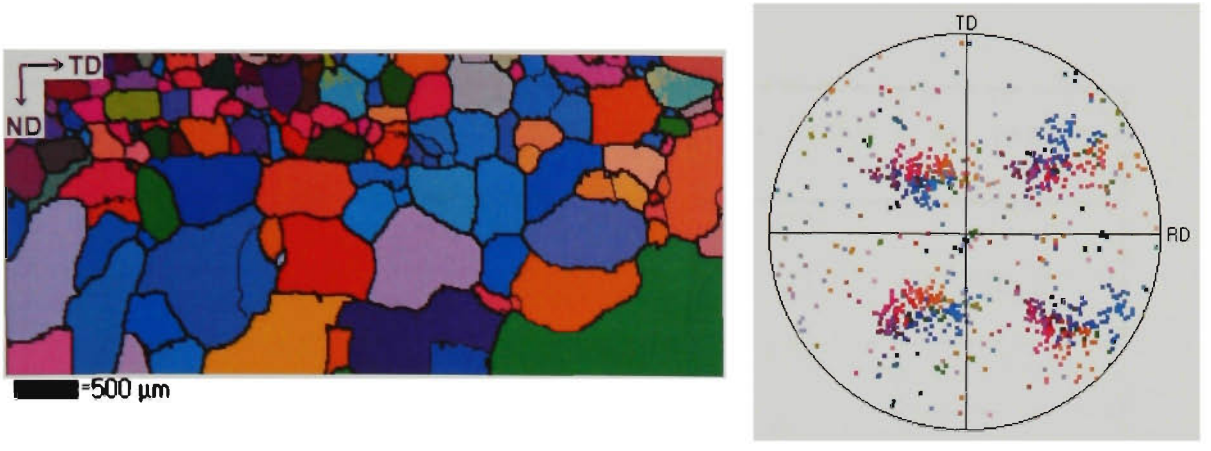

Figure 6.24 EBSD orientation map and (111) pole figure for a (011)[01$\bar{1}$] crystal deformed to a strain of 1.0 at 300°C followed by annealing for 10 hours at 300°C.

6.2.4 Recrystallisation and Recovery Kinetics

The percentage recrystallisation, and the recrystallised grain sizes for each sample are detailed in Table 6.2.

The rate of post-deformation recrystallisation was decreased by an increase in the deformation temperature, and by a reduction in the strain.

Strain	Deformation Temp.	Heat Treatment	Rex. Fraction	Rex. grain size
1.0	25°C	¼ hour @ 300°C	42 %	140 μm
1.0	200°C	¼ hour @ 300°C	46 %	23 μm
1.0	25°C	1 hour @ 300°C	95 %	320 μm
1.0	200°C	1 hour @ 300°C	85 %	40 μm
1.0	300°C	1 hour @ 300°C	23 %	108 μm
1.0	200°C	4 hours @ 300°C	100 %	81 μm
1.0	300°C	4 hours @ 300°C	30 %	240 μm
1.0	25°C	10 hours @ 300°C	100 %	270 μm
1.0	300°C	10 hours @ 300°C	97 %	196 μm
0.5	25°C	1 hour @ 300°C	28 %	600 μm
0.5	200°C	1 hour @ 300°C	36 %	125 μm
0.5	300°C	1 hour @ 300°C	18 %	77 μm
0.5	25°C	4 hours @ 300°C	92 %	800 μm
0.5	200°C	4 hours @ 300°C	45 %	53 μm
0.5	300°C	4 hours @ 300°C	24 %	141 μm
0.5	25°C	10 hours @ 300°C	62 %	1300 μm
0.5	200°C	10 hours @ 300°C	67 %	148 μm
0.5	300°C	10 hours @ 300°C	60 %	140 μm

Table 6.2 Details of the heat treatment for deformed (011)[01 $\bar{1}$] oriented crystals.

7 Discussion - Deformation of the Cube Orientation

7.1 Microstructure and Texture of Cold Deformation

The active slip systems for fcc metals at room temperature are known to be {111} <011>[1]. The Cube orientation lies with the [100] crystallographic direction parallel to the rolling direction (Fig. 7.1) and its active slip systems at room temperature have been calculated to be $(111)[10\bar{1}]$, $(\bar{1}\,\bar{1}\,1)[\bar{1}0\bar{1}]$, $(\bar{1}11)[\bar{1}0\bar{1}]$ and $(1\bar{1}1)[10\bar{1}]$ when deformed in plain strain compression[68]. In the Bishop-Hill notation, these correspond to the systems $-a_2$, $-b_2$, $-c_2$ and $-d_2$[2], and are shown schematically in Fig. 7.1.

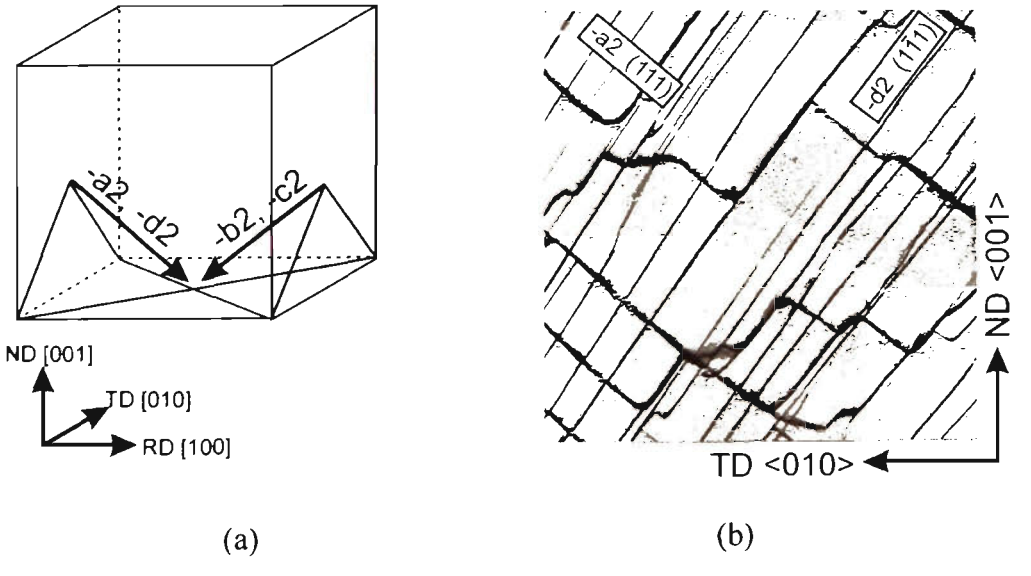

Figure 7.1 (a) Schematic diagram of slip systems in the Bishop–Hill notation after Wert *et al.* [68]. (b) Slip traces on surface of Cube crystal deformed to a strain of 0.06 on grey face of schematic in (a). Region (b) = 150 μm x 150 μm.

Cube oriented grains are unstable during low temperature rolling or plane strain compression, and break up to form deformation bands [18, 22, 68, 69]. Development of deformation bands begins at low strains. Liu and Hansen [69] observed their

development at a strain of 0.16, where the rotation occurred about the TD with a magnitude of ~4°. This is consistent with the current study where a deformation band was observed at a strain of 0.2, and the rotation about TD across the band was measured to be ~7° (Fig. 7.2). AFM imaging of the surface topography showed that the band deformed by single slip, whereas the remainder of the sample displayed slip on more than one plane (Fig 7.3).

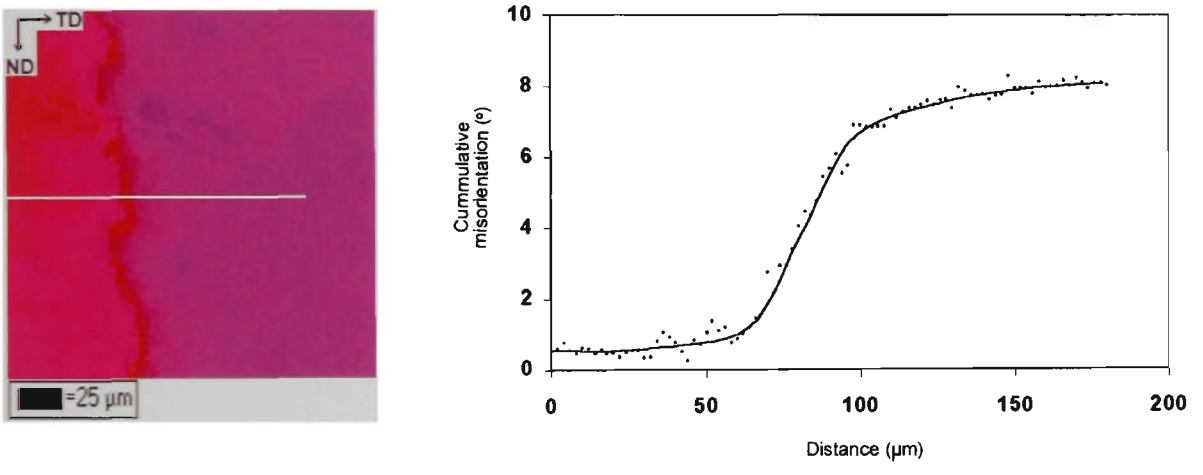

Figure 7.2 (a) EBSD orientation map of deformation banding in Cube crystal deformed to 0.2. (b) Misorientation across band shown in (a).

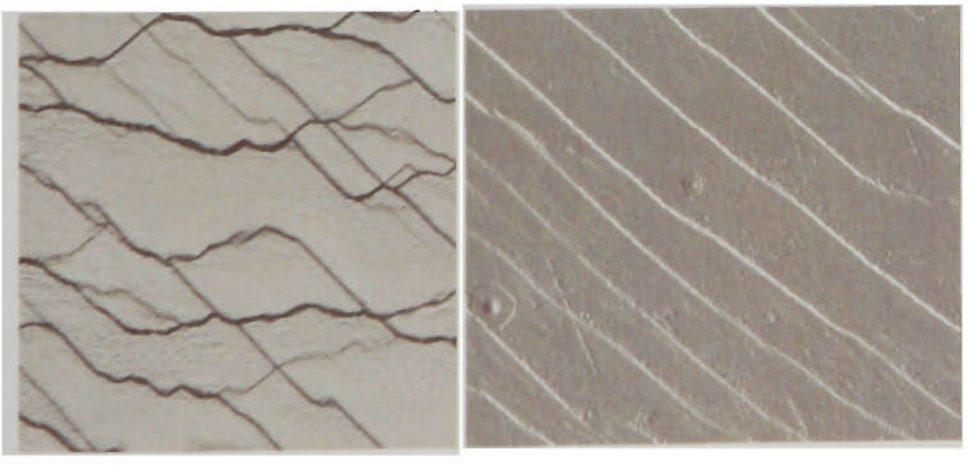

(a) (b)

Figure 7.3 AFM deflection images of Cube crystal deformed to 0.2 showing (a) bulk deformation behaviour and (b) deformation band slip behaviour. Each micrograph = 150 µm x 150 µm.

Published data show that with increasing deformation the initial Cube orientation further diverges about the TD and after a true strain of unity (63% reduction) the crystal composes two symmetrical orientation components of type $\{012\}<02\bar{1}>$ [18, 35, 67]. AFM and EBSD examination of samples deformed at strains greater than 0.7 showed that the entire microstructure splits into bands of alternate orientations, and confirm that these bands rotate toward the orientation $\{012\}<02\bar{1}>$ (see Fig. 5.2 of the Results section).

Maurice and Driver[35] and Akef and Driver[67] reported that after strains greater than 2 (86% reduction) further rotation about the TD together with slight RD rotations lead to the formation of 4 S-type orientations, ie.

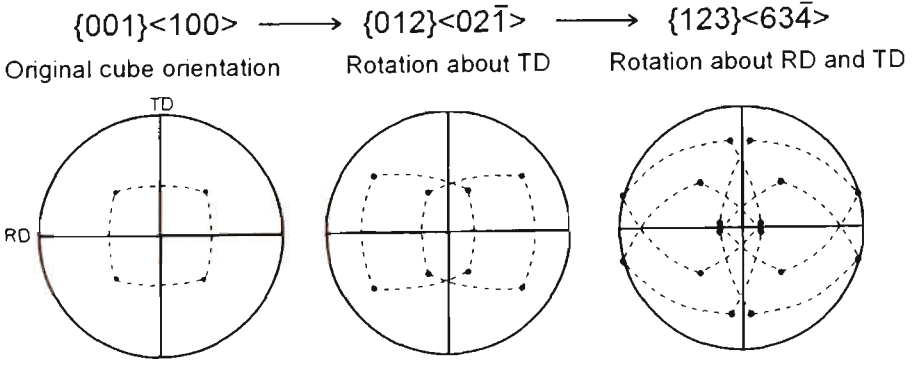

While such rotations are reported to lead to the development of deformation bands in the rolling plane[22, 67], none were found in the current study. These bands are the result of high strain deformation, above a true strain of ~1, and accompany the formation of the S-type orientations [35, 67].

7.2 Deformation and Transition bands

Kulkarni *et al.*[21] have recently completed an extensive study of deformation banding in polycrystalline aluminium. The development of deformation bands was found to occur firstly by orientation splitting of individual grains, followed by subdivision of the bands themselves into 'secondary' and 'tertiary' bands. There is evidence that such a decomposition occurs in the Cube orientation, and an example was shown in Fig 5.4 of the Results section.

The published data of Liu *et al.*[22], Liu and Hansen[69], and Akef and Driver[67] have been analysed, and the width of 'primary' deformation bands estimated by the use of published micrographs and orientation profiles. These measured deformation band widths have been plotted as a function of strain, and the effect of strain on deformation banding in Cube single crystals of Al quantified.

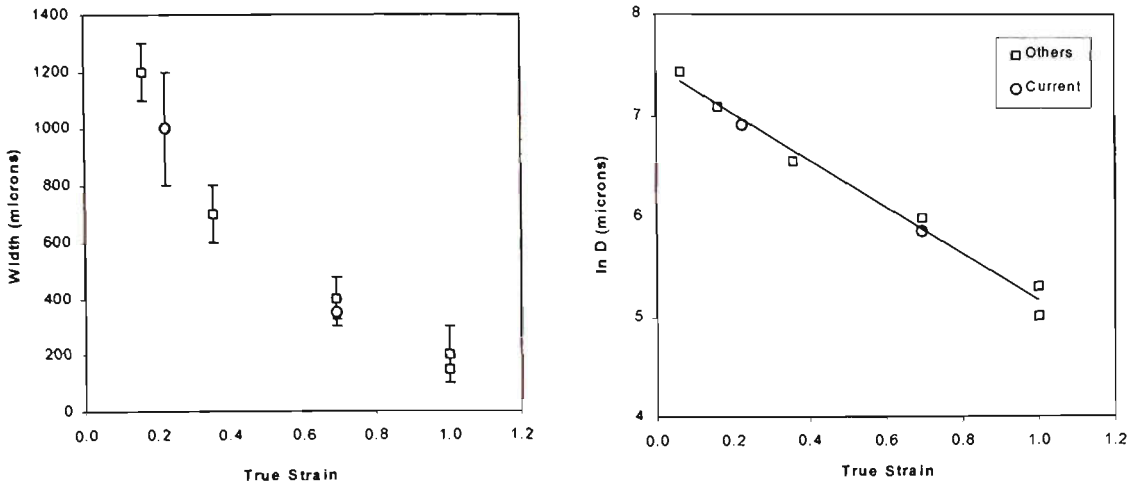

(a) (b)

Figure 7.4 Deformation band width (D) as a function of true strain derived from published results of Liu *et al.*[22], Liu and Hansen[69] and Akef and Driver[67] and the current results.

Figure 7.4b shows the logarithmic change in deformation band width with strain. Applying a line of best fit the linear data points produce a relationship of the form ln D = $-2.3\varepsilon + 7.5$, allowing an estimation of the largest possible deformation band (1808 μm).

It is well established that an increase in strain corresponds to an increase in crystallographic rotation across transition bands, and also corresponds to an increase in misorientation gradient within transition bands[22, 67]. The misorientation across transition bands has been measured as a function of strain for each cold deformed Cube oriented crystal (Fig. 7.5). The published data of Liu and Hansen[69], Akef and Diver[67] and Liu *et al.*[22] have also been used for comparison in this figure, showing the strong influence of strain on the misorientation across transition bands.

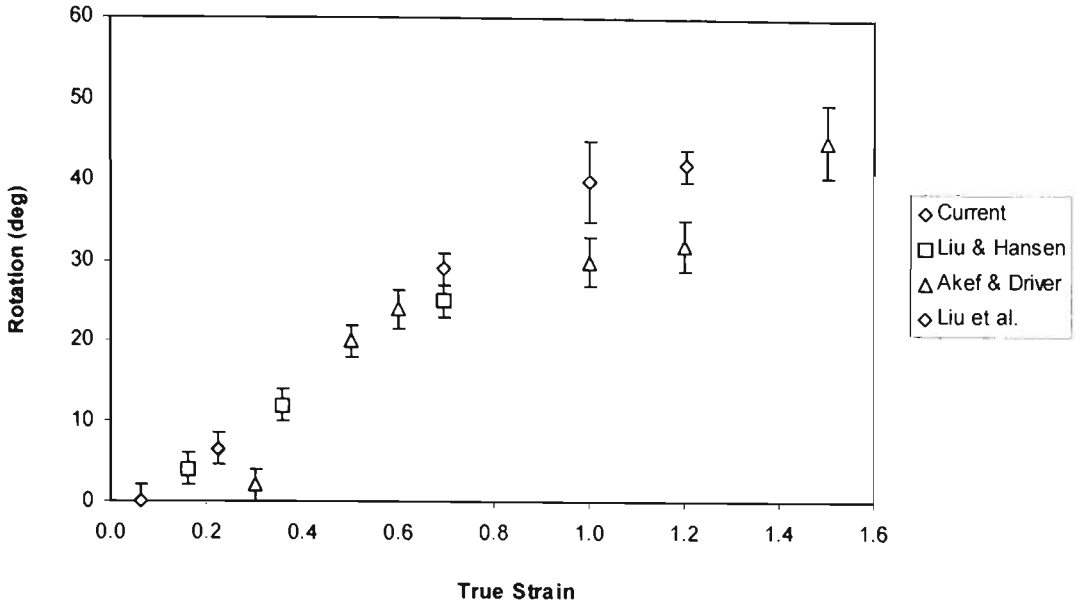

Figure 7.5 The effect of strain on the misorientation across transition bands formed in cold deformed Cube oriented crystals parallel to the TD.

A summary of the experimentally determined rotations associated with deformation bands in cold deformed Cube oriented crystals is shown in Fig. 7.5. It is clear that up to a strain of 0.8 there is a linear relationship between strain and crystallographic rotation. Through a line of best fit analysis, excluding those data points above strains of 0.8, and excluding the one outlier at $\varepsilon = 0.3$, the beginning of deformation banding has been calculated to be at a strain of 0.1. For strains greater than 0.8, significant rotations about RD begin, which lead to a more complex deformation microstructure and texture. This is probably the reason for the spread in results above this strain.

When deformed in plane strain compression, the width of a sample remains constant. When the first deformation band develops, it has an effective width of half the sample size. Each side of the transition band rotates in opposite directions about the TD. For the next band to develop, as has been observed experimentally, one portion of the sample must cease to rotate in one direction, and then rotate back through the Cube orientation

and continue on. This orientation reversal ensures that the Cube orientation is retained within the transition band between the parent and the secondary bands. Basson and Driver[89] observe that many bands originate at the interface between die and sample, as did the current study. However, some secondary bands such as those in Fig. 5.4 do not appear to originate at the sample surface.

7.3 Theories of Deformation Banding in the Cube Orientation

Plane strain compression prevents lateral spread or transverse shear on deformation, and restricts the deformation to two strain components, reduction in height in the normal direction, and increase in length in the rolling direction. Stated mathematically,

$$\varepsilon_{ij} = \begin{pmatrix} \varepsilon_{11} & 0 & 0 \\ 0 & 0 & 0 \\ 0 & 0 & -\varepsilon_{33} \end{pmatrix}$$

where ε_{ij} is the total strain on the system. For Cube oriented crystals, the amplitude of shear, γ, on each of the 4 slip systems can be calculated by multiplying the total strain by the Schmidt factor (0.41 for the Cube orientation) and dividing by 4. Assuming equal slip occurs on the four equally stressed systems, a_2, b_2, c_2 and d_2, no rotation of the lattice is expected to occur, which is in clear contradiction to observations of extensive TD and RD rotations with strain[68].

Many mathematical models have been proposed to describe this behaviour. Most analyse the rotation rates of the Cube crystal using Taylor type theory, usually with

relaxed constraints. The models differ primarily in the assumption of which systems are operating within the deformation band. The first model reviewed assumes only one from the four possible slip systems operates within the band. The other two models assume pairs of systems operate unequally: Wert *et al.*[68] assumes these pairs are co-linear (different planes in the one direction) whilst Basson and Driver[89] assume the opposite combination of pairs. The following sections review the models proposed for the creation of deformation bands in Cube oriented crystals, specifically in relation to the extensive TD rotations which lead to the formation of deformation bands.

7.3.1 Single Slip

Akef and Driver[67] have analysed the possibility that deformation bands are the result of regions of single slip, a condition that requires the complete suppression of the other 3 systems within the band.

Single slip leads to the greatest rotation rate with strain, occurs by rotation exclusively about TD, and this has been calculated to be:

a_1, c_1 $\quad 2\phi = \sin^{-1} [1-\exp\{-2(\varepsilon-\varepsilon_c)\}]$ (7.1)

b_1, d_1 $\quad 2\phi = \sin^{-1} (-[1-\exp\{-2(\varepsilon-\varepsilon_c)\}])$ (7.2)

where ϕ is the rotation angle about TD, and ε is true strain. The calculation requires the selection of a critical strain, ε_c, below which deformation banding does not occur. Akef and Driver choose 0.3, whilst it is known that deformation bands occur at strains as low as 0.15[22]. When a value of 0.1 is substituted into the equation for ε_c, Equation 7.1

shows a similar trend shifted to lower strains. The model also predicts that the theoretical maximum rotation of 45° occurs at a strain of 0.7 (Fig. 7.6). This analysis clearly predicts a crystallographic rotation that is far more rapid than experimentally observed (Fig. 7.6b).

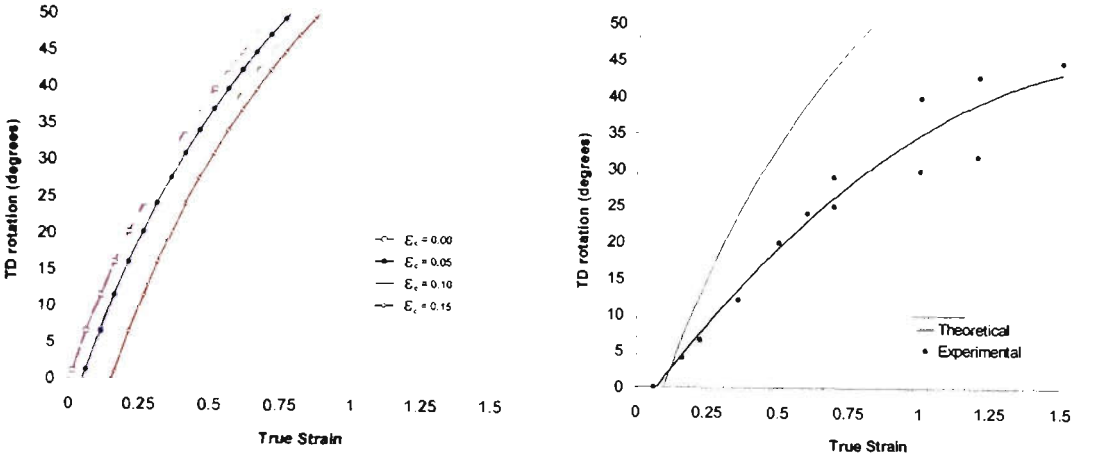

(a) (b)

Figure 7.6 (a) Theoretical crystallographic rotation about a deformation band in the Cube orientation, predicted by Equation 7.1, as a function of strain, and assuming the critical strain values (ε_c) shown on the graph. (b) Experimentally measured crystallographic rotation.

7.3.2 Co-linear slip

Wert *et al.*[68] suggest that the 4 systems can be paired into two sets of 2 slip systems, and that each pair share a common direction (the pairs of systems are co-linear). If each pair produces a different amount of slip this will lead to the rotation of the lattice to produce deformation bands. When alternate pairs dominate slip in adjacent bands, this leads to the divergent nature of rotations that are observed experimentally.

Mathematically, the co-linear slip theory produces an expression for the rotation about the sample axes:

$$R1 = 0$$

$$R2 = \frac{-4\delta\gamma}{\sqrt{6}} \qquad (7.3)$$

$$R3 = 0$$

where $\delta\gamma$ is the difference in shear strain between the two pairs of systems. The true strain applied to the sample may be converted to the shear amplitude (γ_o) by multiplying true strain by the Schmidt factor and dividing by 4 ($^1/_4$ shear on each 4 systems). Thus Wert *et al.* find that a shear amplitude change of 20% between systems can cause the TD rotations observed in their experiments. The current work has shown that the rotation about the RD is negligible up to a strain of ~0.7, which suggests that the co-linear slip theory becomes invalid beyond this strain because significant rotations about the RD are then known to occur.

Co-linear slip, for example, on systems b_2 and c_2, would occur in the common direction, [101], on the different planes, $(\bar{1}\,\bar{1}\,1)$ and $(\bar{1}\,1\,1)$. Basson and Driver[89] point out that surface topography observations of a co-linear slip mechanism would show that deformation bands have activity on two planes which are at 90° to one another. If this were the case, deformation bands would appear virtually identical to areas deforming by equal slip on all 4 systems. This is not consistent with observations both in the current study and those by optical techniques[67].

7.3.3 Slip Rate Ratio Model

Basson and Driver[89] propose that at the earliest stages of deformation, local perturbations occur at sites such as the crystal/die interface, and that these small rotations promote or nucleate deformation bands. This assumption is supported by AFM observations in the current experiments, where preferential activity of certain systems was found to occur at the smallest strain of 0.06 (Fig. 7.7). In this example, the deflection image shows the 4 different slip system traces as white lines and black lines at both +45° and -45°. It is clear in the figure that over this small region, which lies in the centre of the sample, the magnitude of slip is not equal on all 4 systems. The strain accommodation has been analysed already in the section 5.2, and although many slip lines have approximately the same height, the number of slipped planes from each system is vastly different at this low strain.

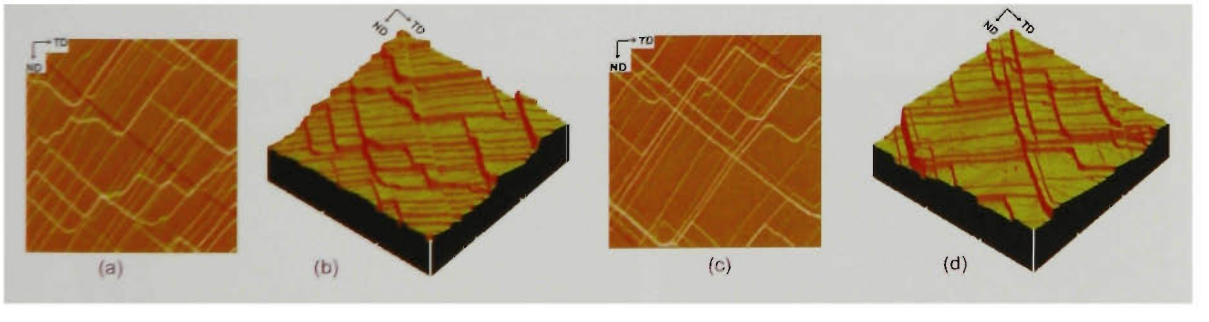

Figure 7.7 AFM images of Cube oriented crystal deformed to a strain of 0.06. (a) Deflection image of (b). (c) Deflection image of (d).

The Basson-Driver[89] model assumes that these local perturbations lead to the formation of the first deformation band, followed by the opposite rotation of the adjacent lattice causing a cascade of rotations resulting in the formation of many bands. These bands supposedly form by the predominant operation of $\{a_2+b_2\}$ and $\{c_2+d_2\}$

systems. Mathematical analysis of this assumption shows rotation can occur about both the TD and RD, but that ND rotations remain zero. This seems the most plausible model for deformation banding, and accounts for all experimental observations of both slip line analysis, local crystallographic rotation and macroscopic textural analysis.

7.4 Coupling AFM , ECC and EBSD

After the surface relief accompanying deformation had been fully characterised, regions of interest such as deformation bands were investigated using EBSD and ECC techniques. For the coupling of these techniques, the samples deformed to strains of 0.7 and 1.2 were most suitable due to their inhomogenous deformation structures. Also, samples deformed to low strains showed little structure in ECC and EBSD. ECC is a qualitative technique that images both surface relief and crystallographic rotation. It is an excellent tool to bridge the quantitative data obtained by AFM and EBSD.

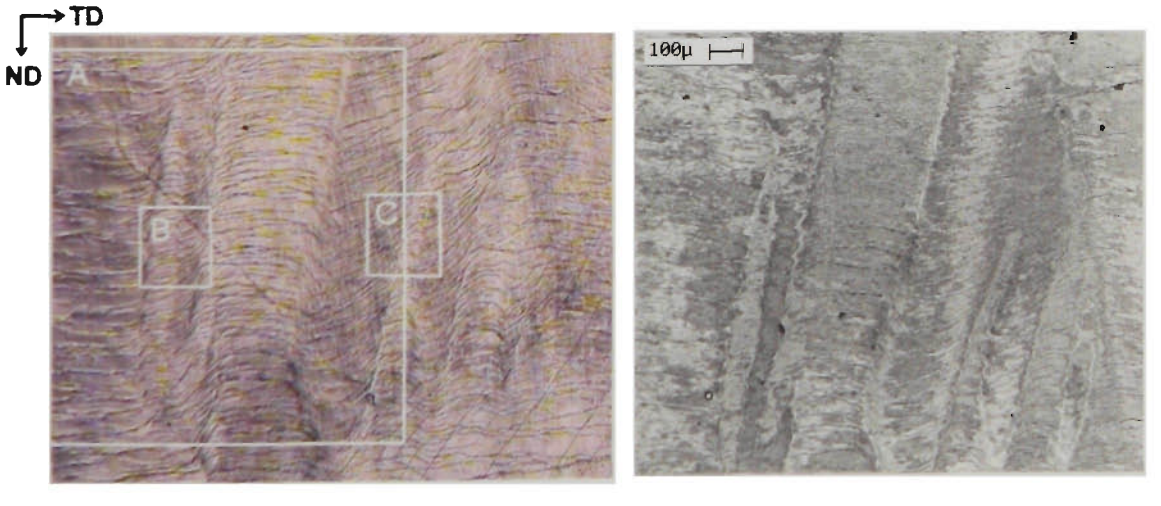

(a) (b)

Figure 7.8 (a) Optical micrograph and (b) SEM ECC of the ND-TD face of a Cube oriented single crystal deformed to a strain of 0.7.

Figure 7.8 shows a low magnification optical micrograph of the ND-TD face of a Cube crystal deformed to a strain of 0.7. The same region was imaged using ECC (Fig. 7.8b) and the crystallographic rotation between bands is clear even at such low magnification. Regions that were analysed more closely are boxed in white in Fig. 7.8a, and labelled A, B. and C. Region A was further investigated using EBSD, and Regions B and C were analysed using AFM. ECC and EBSD.

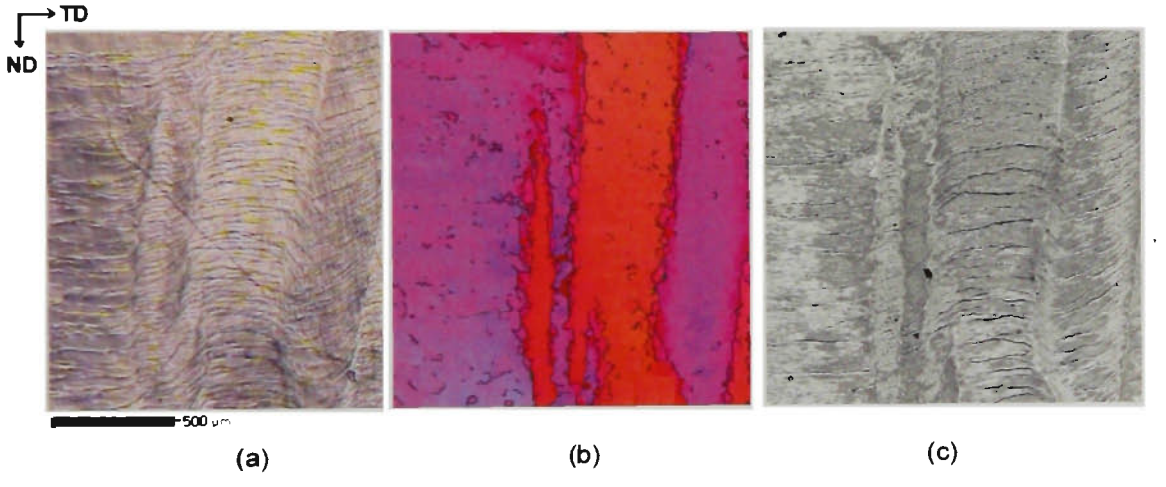

Figure 7.9 (a) Optical, (b) all Euler orientation, and (c) ECC micrographs of Region A in Fig. 7.8.

In Region A, an excellent correlation between visible slip lines and crystallographic orientation has been found using a combination of optical, electron microscopy and EBSD (Fig. 7.9). Alternate deformation bands can be seen to have the same crystallographic orientation through EBSD, and deformation in these bands produces similar slip line traces. The sharp transition band regions can be seen using ECC to exist between regions of different slip pattern.

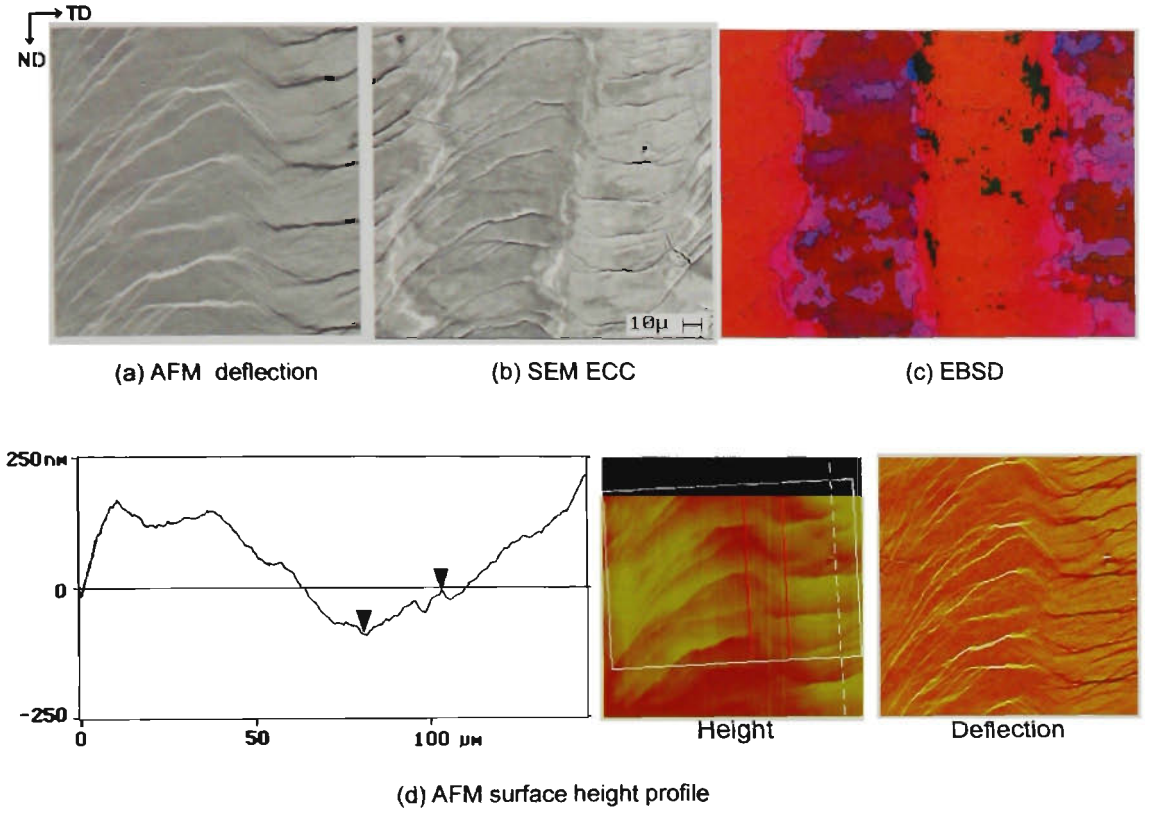

Figure 7.10 (a) Deflection AFM, (b) ECC, (c) EBSD all-Euler orientation mapping, and (d) surface height profile from Region B in Fig. 7.8

Region B is detailed in Fig. 7.10. The ECC image shows clearly those regions of high rotation which correspond to transition bands, and these are also clear in the EBSD orientation map. There is an equal crystallographic rotation on either side of the deformation band, as indicated by the orientation map (Fig. 7.9c).

The surface height cross-section shows the average surface level drop across the transition bands. The lowest trough corresponds to the transition band shown as a white band in the ECC micrograph. Crystallographically, this trough lies in the centre of a transition band which has an almost constant orientation gradient. Also apparent in the surface height cross-section is the beginning of a surface level drop associated with the adjacent deformation band, seen on the left side of the ECC and EBSD microstructures.

The trough and peak lie 80 μm apart, which is the approximate distance between transition bands in both the ECC and EBSD micrographs.

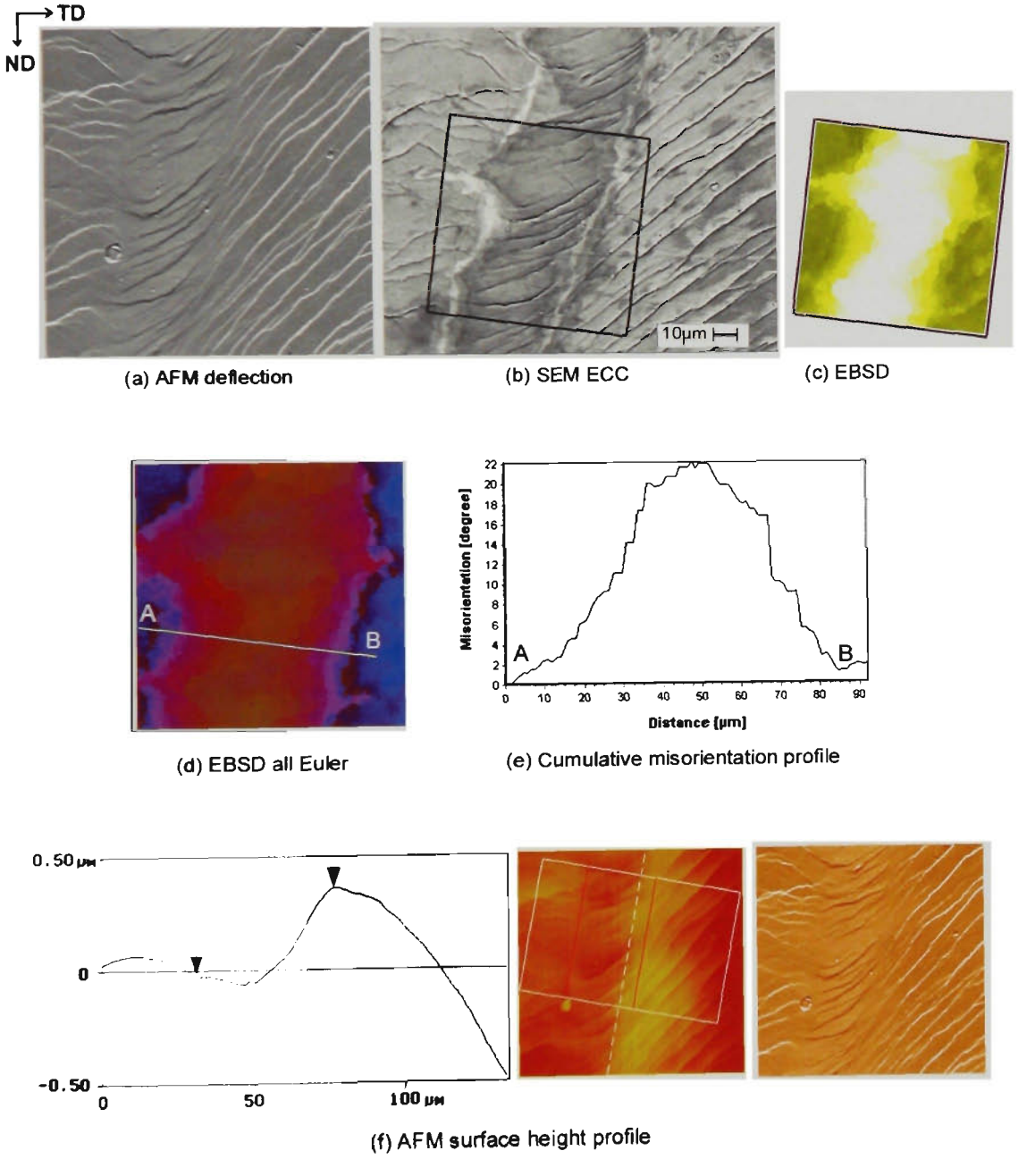

Figure 7.11 (a) Deflection AFM: (b) ECC; (c) EBSD all-Euler orientation map; (d,e) all Euler orientation map and misorientation profile; and (f) AFM surface height profile for Region C in Fig. 7.8.

The sensitivity of the ECC technique has been highlighted in the analysis of Region C (Fig. 7.11) where small orientation changes are visible, and correspond well to the crystallographic rotations in Fig. 7.11c.

The surface level change is consistent along the length of the band, and has a magnitude of 0.4 μm from peak to trough. The peak corresponds to the transition band indicated, and the trough to the adjacent transition band. The crystallographic rotation about the two transition bands are almost identical (25° in Fig. 7.11e), whereas the surface level changes are markedly different. ECC the two transition bands are microstructurally distinct also, the band on the right side to be thinner, and the left band to be wider and more curved. Despite being crystallographically similar, the two adjacent deformation bands exhibit markedly different surface topography and microstructure.

The transition bands have been measured to be 45 μm apart by ECC and EBSD micrographs, and this corresponds to the arrows in the surface height profile shown. Although the second transition band does not lie at a trough, it corresponds to a small deviation in height from the trend. These small deviations at the point of a transition band have been found to occur in other samples also.

Another example of the surface relief effects at transition bands is shown in Fig. 7.12, where the transition bands 1 and 2 correspond to a peak and trough respectively.

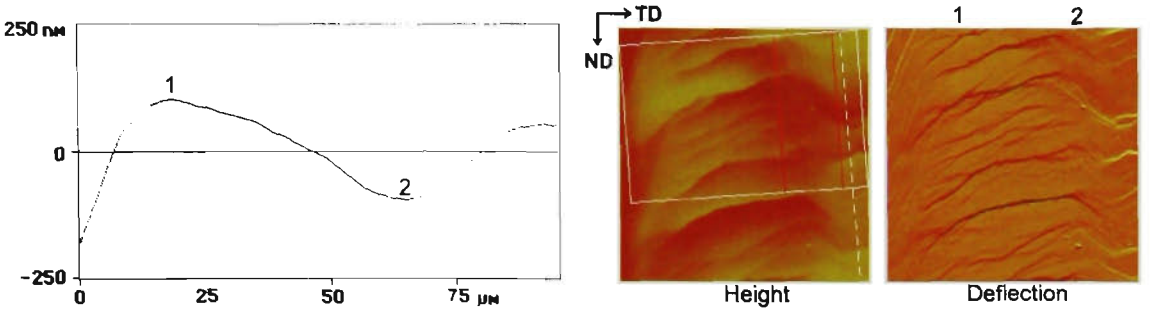

Figure 7.12 Average surface level changes across adjacent transition bands

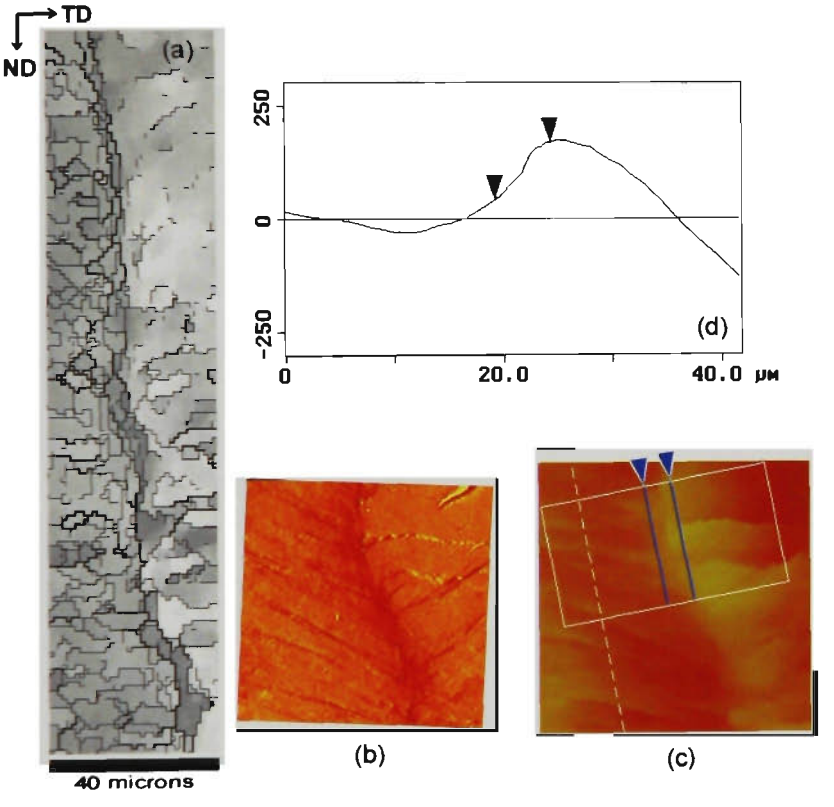

Figure 7.13 (a) EBSD Euler 3 map; (b) AFM deflection image; (c) AFM height image; and (d) averaged surface height profile for one region on a Cube oriented crystal deformed to a strain of 1.2.

The surface drop across the transition band is reasonably consistent throughout the region that has been analysed. For example, Fig. 7.13 shows a change in surface level of ~210nm from peak to trough, and there is also a sudden and distinct drop in surface height at the transition band which has an approximate magnitude of 80nm. The crystallographic rotation is also fairly consistent, it varies between 40 and 45°. The

region from peak to trough corresponds to what has been measured by EBSD to be the transition band, and has a width of ~7 μm. At high strains, most transition bands exhibited a rapid drop in surface level, with the peak to trough horizontal distance being slightly larger than the width of the transition band.

To conclude, with the aid of EBSD and ECC the exact position of transition bands can be found on AFM micrographs. This analysis has highlighted the inhomogenous nature of deformation and transition bands. Transition bands not only lie at the peak or trough in the surface profile, but are also characterised by a rapid and localised change in surface gradient.

7.5 High Temperature Deformation

7.5.1 Static or Dynamic Recrystallisation?

The rate of quench produced by the deformation equipment is very high, with complete quenching from 500°C taking less than 15 seconds, with a constant cooling rate of ~35°s^{-1} (Fig. 7.14).

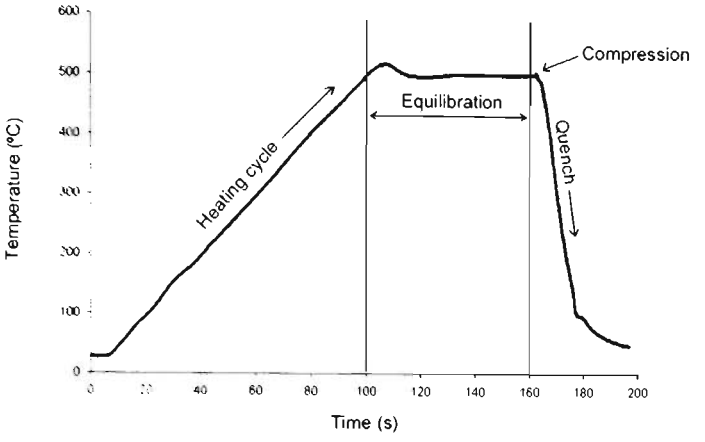

Figure 7.14 Temperature profile for sample deformed at 500°C at a strain rate of $0.5s^{-1}$

Hot deformed samples examined in the as-deformed state were found to have partial or fully recrystallised microstructures. High purity polycrystalline aluminium is known to deform by dynamic *recovery*, the high SFE and absence of second phase particles allows development of a well defined substructure, and deformation occurs with a steady state flow stress. The operation of dynamic *recrystallisation* is evident by two main indicators. Firstly, the retention of substructure within recrystallised grains, and secondly a significant drop in flow stress after initiation of dynamic recrystallisation. Extensive analysis using ECC and EBSD techniques produced no evidence of substructure in large recrystallised grains. ECC allows resolution of small orientation changes , less than 1°, and any rotation within large grains would be evident with this technique. Use of flow curves for analysis of dynamic processes was found to be inappropriate because of high strain rate, increasing sample to die friction with elongation, and die friction due to loosening of deformation dies during the heating cycle.

Dynamic recrystallisation of high purity Al has been reported to occur under unique circumstances. Huang and Humphreys[101] have described "transient" dynamic

recrystallisation in a high purity polycrystalline alloy that was subjected to high temperature straining, followed by sudden change in strain rate. In this experiment, as in dynamic recrystallisation of low SFE metals, the grain boundaries played an important role in the nucleation of recrystallisation. In the case of monocrystalline aluminium, dynamic recrystallisation has been reported[102] to occur in Al-Si alloys at temperatures as low as 220°C. In this instance the authors attribute the behaviour to the high purity of the aluminium. At 2 ppm Si, dynamic recrystallisation produces large grains with some substructure, whilst at 25 ppm this behaviour can be completely inhibited through grain boundary pinning by solute segregation. The alloy used in the current experiments far exceeds these super high purity conditions required for dynamic recrystallisation. For these reasons it is not considered likely that dynamic recrystallisation has occurred.

However, the kinetics of the formation of statically recrystallised grains must be considered. Within a quench cycle of 8-12 seconds significant recrystallisation had occurred in some samples. Post-deformation static annealing showed that long annealing times were required to continue recrystallisation, inferring that the rapid recrystallisation found in the as-deformed state is linked to the deformation. Rapid static annealing with no apparent incubation period has been observed before, and is referred to as metadynamic recrystallisation. Metadynamic recrystallisation is known to be promoted by high strain rates[103] and requires a smaller critical nucleus size than dynamic recrystallisation[104]. It is usually associated with dynamically recrystallising structures containing small nuclei which, at the cessation of deformation, immediately grow into recrystallised grains. In the case of aluminium, perhaps the well developed substructure is analogous to small dynamically formed nuclei, these are too small or too

low in energy to recrystallise dynamically, but can recrystallise metadynamically after deformation, either prior to or during the quench cycle.

7.6 Cube Stability

7.6.1 Effect of Strain and Temperature

The effect of strain on the stability of the Cube orientation at room temperature was found to be significant (Fig. 7.15). At low strains the Cube orientation is stable, but the stability rapidly drops at strains greater than 0.3.

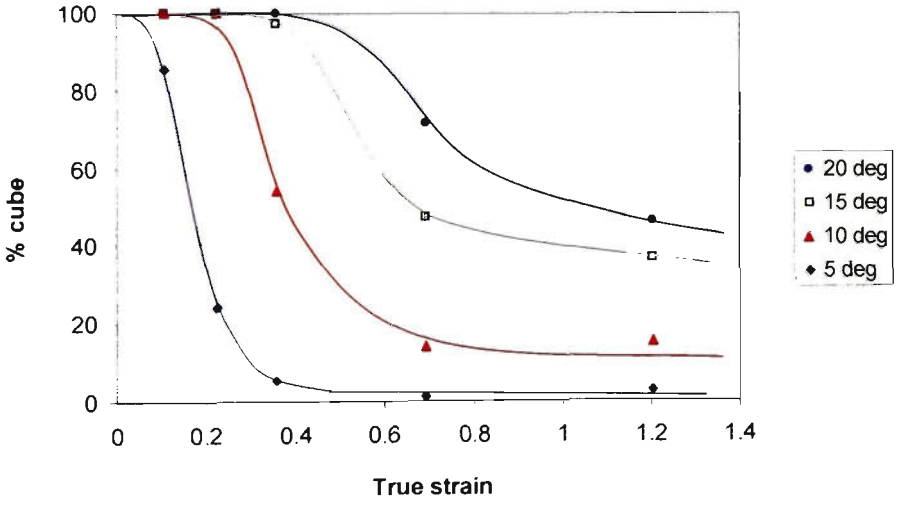

Figure 7.15 Stability of the Cube orientation deformed at 25°C. Each line represents the percentage of Cube within 5, 10, 15 or 20° of ideal Cube orientation.

Maurice and Driver[18] hot deformed Al Cube crystals over a range of strains, and although not stated in the text, low strain crystals (below a true strain of 0.5) were all found to be stable, regardless of the deformation temperature or strain rate.

Huang *et al.* [39] investigated the high temperature (300 - 500°C) stability of Cube crystals to a strain of 1.4, whilst the current high temperature experiments were carried out to a true strain of 1.0. Figure 7.16 shows both sets of results of the percentage of Cube measured by EBSD techniques, and these have been plotted as a function of deformation temperature to compare the effect of strain on high temperature deformation. All data points were obtained at a strain rate of 50 s^{-1}.

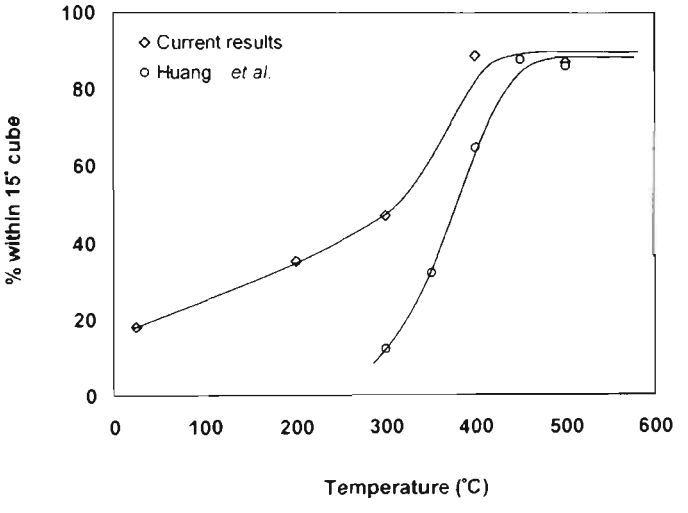

Figure 7.16 Temperature dependence of the Cube stability for strain rate of 50 s^{-1} for the current experiments and those of Huang *et al.*[39].

From Fig. 7.16 it is clear that the trend established for cold deformation is true also for high temperature deformation. The stability is decreased with increasing strain. This confirms the work on polycrystalline aluminium by Vatne *et al.*[36, 38] who also conclude that strain reduces the retained Cube texture during hot deformation.

7.6.2 Measured Cube Stability

Having established that the Cube stability is highly strain sensitive (Figs. 7.15 and 7.16), Fig. 7.17 summarises the extensive experimental work on Cube crystals over a range of strains, strain rates and temperatures. Clearly visible is a regime of low strain in which the Cube orientation is stable. Also apparent is its stability at high strains above ~350°C. The Zener-Hollomon parameter (Z) has also been used to summarise this behaviour with respect to strain because it combines the effects of strain rate and temperature into a single parameter.

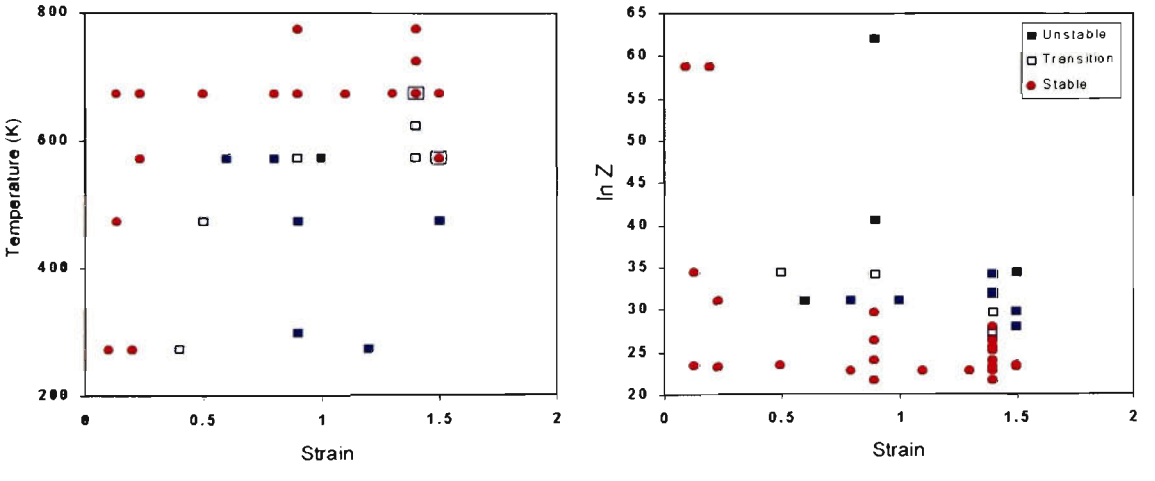

Figure 7.17 Effect of strain and temperature on Cube stability after[18, 39] and the current results.

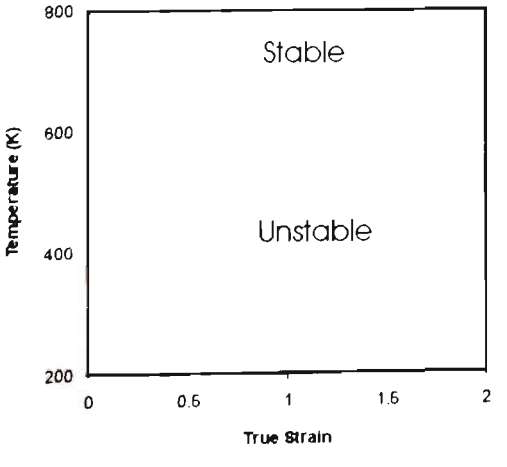

Figure 7.18 Schematic illustration of the regions of stability and instability of the Cube orientation in plane strain compression.

8 Discussion –Deformation of the (011)[01 $\bar{1}$] Orientation

8.1 Cold Deformed Texture

At room temperature, the active slip systems for the (011)[01 $\bar{1}$] orientation have been calculated by Wrobel *et al.*[79], and are shown schematically in Fig. 8.1.

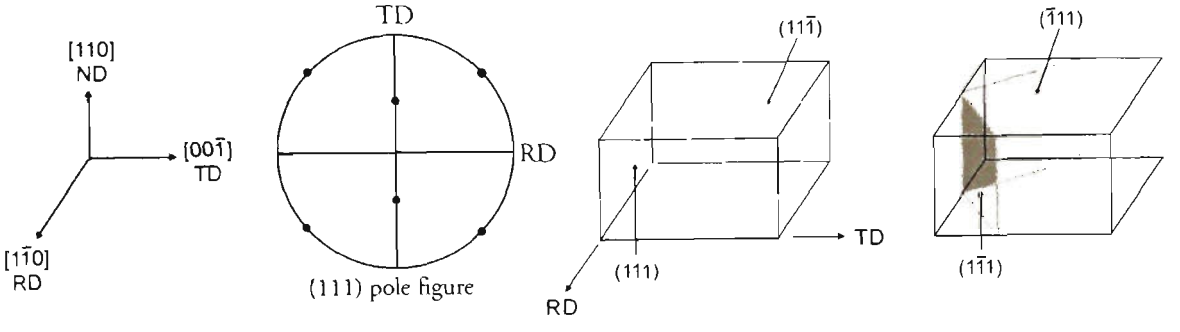

Figure 8.1 Schematic illustration of the active slip systems in the (011)[01 $\bar{1}$] orientation after[79].

The deformation texture produced by plane strain compression of the (011)[01 $\bar{1}$] orientation is complex, and there are conflicting reports concerning both the texture and microstructure produced by deformation. Most texture data has been measured using XRD, which does not allow correlation of microstructure and orientation. The only EBSD study other than the current work is that of Akef and Driver[85], whose report focussed on the recrystallisation behaviour of the orientation.

There are two main deformation textures reported to occur in Al and Cu crystals of this orientation. In three separate publications, Butler *et al.*[81], Wrobel *et al.*[79] and Blicharski *et al.*[83] reported that this orientation rotates exclusively about the ND, retaining all orientations in close proximity. In all three studies the crystals were found

to rotate in one direction only, creating no symmetrical component of the opposite rotation (Fig. 8.2a). Butler *et al.*[81] did not begin with an ideal orientation, but with a 4° ND rotation, with deformation inducing crystal rotation in this same direction of offset.

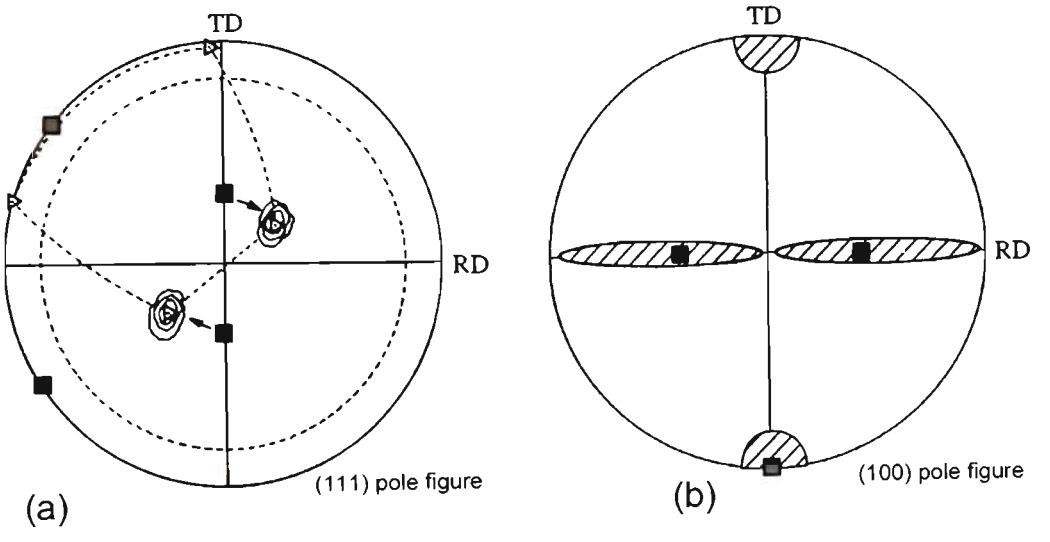

Figure 8.2 Deformation texture of cold deformed crystals of the $(011)[01\bar{1}]$ orientation measured by (a) Blicharski *et al.*[83] and (b) Akef and Driver[85].

The effect of strain on the rotation about the ND is marked. Butler and Hu[81] found that the rotation about ND increased rapidly with strain to reach 50° at 90% reduction (true strain of 2.3), whilst Wrobel *et al.*[79] observed 35° rotation at 65% reduction (true strain of 1.05). The pole figures of the published data on both Al and Cu have been analysed and the ND rotation estimated for each one. These have been plotted as a function of true strain in Fig. 8.3. It is clear from the graph that ND rotations occur rapidly with strain. Those workers who describe exclusive ND rotation on deformation generally describe a "stable" end point to the rotations, but each report provides a different end orientation corresponding to a different strain.

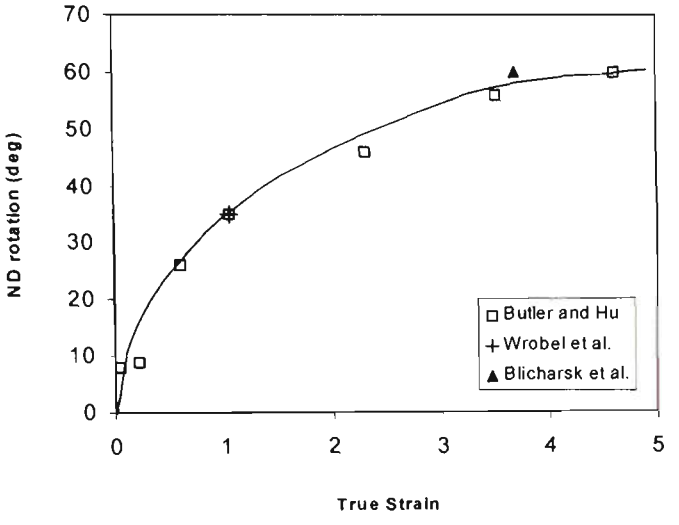

Figure 8.3 ND rotations as a function of strain after Butler and Hu[81], Wrobel *et al.*[79], and Blicharski *et al.*[83].

It is clear from Fig. 8.3 that a crystal that deviates from ideal $(011)[01\bar{1}]$ about the ND by just a few degrees will continue to rotate in that direction when deformed, and this is probably the origin of the conflicting data which exist on the topic. This rapid ND rotation appears to be the reason for this orientation having such a high sensitivity to small offsets from ideal symmetric $(011)[01\bar{1}]$. Any small deviation about the ND from perfect symmetry will rotate the crystal rapidly about this same direction of offset with strain.

In contrast, experiments by Lee *et al.*[72], Akef and Driver[85] and Verbraak[84] show deformation textures consisting of extensive TD rotation, along with some ND rotation (Fig. 8.2b). Akef and Driver[85] describe the texture as a "near fibre texture" which rotates between $(012)[02\bar{1}]$ and $(021)[01\bar{2}]$, and these 3 reports all show that the texture is composed of complementary orientations which are descriptive of the copper type rolling texture. The current work on the deformation texture of $(011)[01\bar{1}]$ indicates that the changes in orientation across a sample are macroscopic, and that

sectioning a sample down the centre before texture analysis may eliminate an entire family of complementary orientations, and this may complicate any comparison with other experimental data.

The current study has shown that at low strains the crystal is quite stable (Fig. 6.1a of the Results section), and it does not exhibit rapid ND rotation, which supports the crystal orientation being close to the exact (011)[01 $\bar{1}$] orientation. At a strain of 0.5 the intensity maximum remains on the starting orientation, with 90% remaining within 8.5°. At a strain of 1.0 the intensity maximum is also on the staring orientation, and is spread about the TD by ~20° (Fig. 6.1b). These results are consistent with the work of Akef and Driver[85] who showed that at a strain of 1.0 the TD rotation is 18.4°.

8.2 Hot Deformed Texture

8.2.1 Microstructural Stability

The most striking result from hot deformation of the (011)[01 $\bar{1}$] orientation is that increasing the deformation temperature appears, at strains of 0.5 and 1.0, to decrease the stability of the orientation. At 200°C the crystals have rotated more from ideal than at room temperature, and at 300°C complementary layers of bands are produced which further spread the deformation texture. This behaviour has been characterised using EBSD on both the ND-TD and ND-RD faces, and also using XRD. The texture of these samples has been determined using pole figures and orientation maps. Fig. 8.4 shows the evolution of the deformation texture in 3-D Euler space. After a strain of 0.5 the

ideal starting orientation has spread about all 3 axes, and after a strain of 1.0 a distinctive deformation texture has evolved.

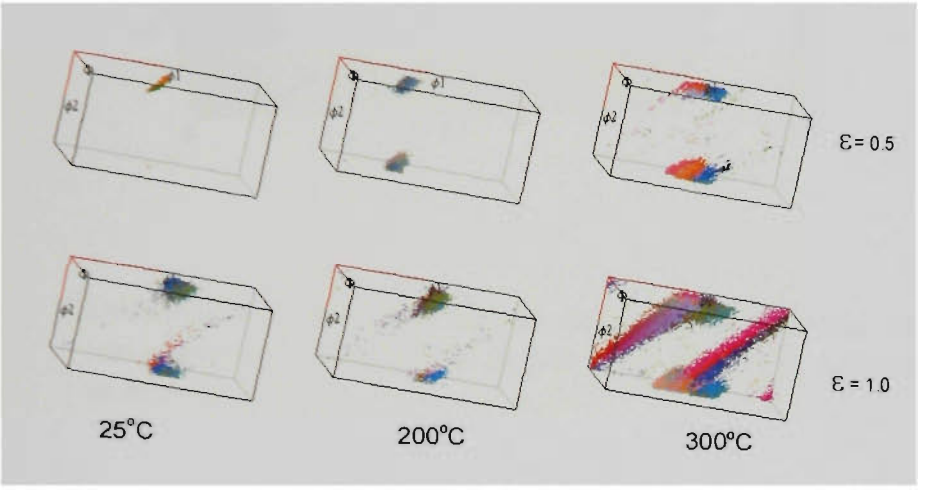

Figure 8.4 Deformation texture of deformed $(011)[01\bar{1}]$ crystals displayed in 3-D Euler space.

The evolution of a tube of orientations in Euler space is evident after a strain of 1.0 at 300°C. This tube does not correspond to those traditionally found after deformation of high SFE metals, ie. the β fibre, nor does it correspond to the α, τ or γ fibres. An intensity plot in 3-D Euler space is shown in Fig. 8.5, where the Euler angle range has been rotated to show the tube more clearly.

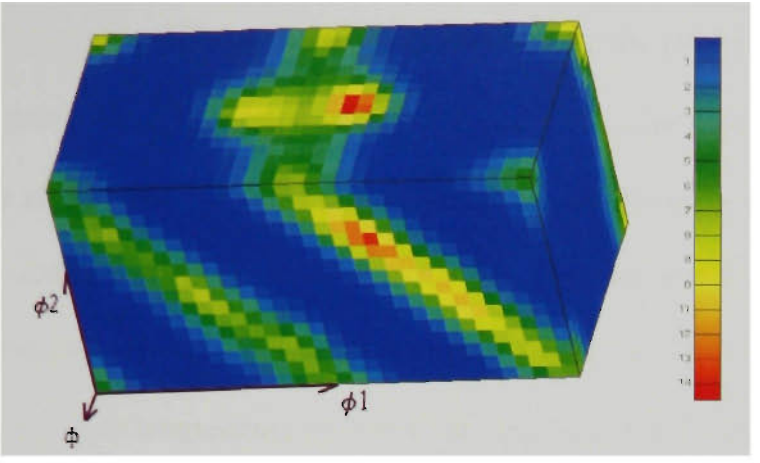

Figure 8.5 Deformation texture for sample deformed to a strain of 1.0 at a temperature of 300°C shown in 3-D Euler space with intensity contours as shown.

The significant decrease in microstructural stability is most evident after a strain of 1.0, and this is described quantitatively in the orientation distribution functions (ODF) in Fig. 8.6. At 25°C the beginning of the deformation fibre is evident, and at 300°C it is pronounced.

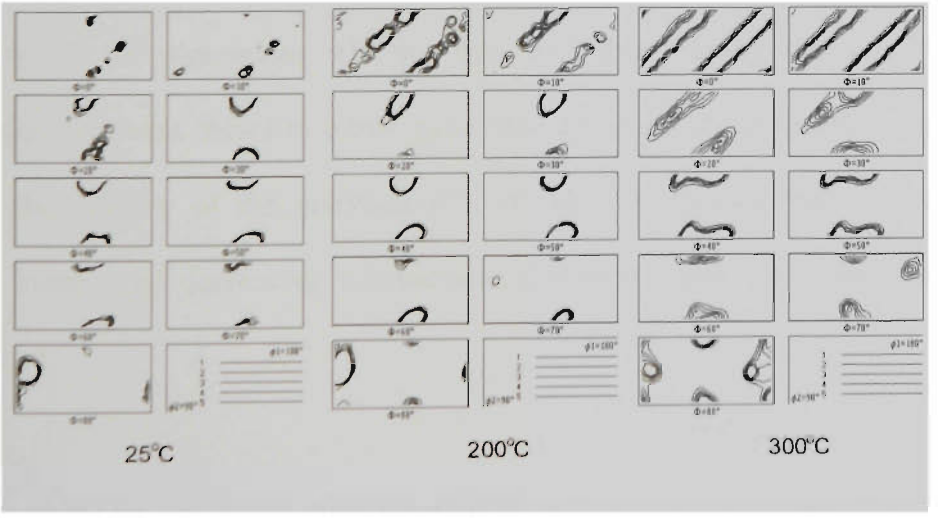

Figure 8.6 ODF of the deformation texture produced after deforming crystals of the $(011)[01\bar{1}]$ orientation at various temperatures.

When deformed to a strain of 0.5 or 1.0 at room temperature, the $(011)[01\bar{1}]$ orientation did not exhibit deformation banding in this study, and none were reported to occur by Akef and Driver after a strain of 1.0[85]. However, Ferry and Humphreys[100] observed a herring-bone structure after a strain of 1.4. This suggests that the critical strain required for formation of these herring-bone bands is between 1.0 and 1.4 at room temperature. At a higher temperature of 300°C, herring-bone bands were observed at a strain of 1.0. A possible precursor to their formation was observed at a strain of 0.5, in the form of the large parallel bands shown in Fig. 6.7. At 300°C, the strain required to form the herring-bone bands is between 0.5 and 1.0. This evidence suggests that formation of a herring-bone deformation structure is a behaviour exhibited by this orientation at high strains, and that increasing the temperature of deformation reduces the strain required to form these bands. This behaviour appears to be the origin of the decreasing stability of this orientation at higher deformation temperatures.

There is little information in the literature concerning the high temperature behaviour of single crystals of aluminium. Of the data available, raising the temperature of deformation has been found to either have little effect on the deformation texture, or increase the stability of the orientation[73, 76, 105]. It appears that this is the first reported instance of decreasing microstructural stability with increasing deformation temperature.

Theyssier *et al.*[73] found that after hot deforming a number of crystal orientations, the substructure produced in the ND-RD plane was highly dependant on the deformation geometry. Deformation produced non-octahedral slip traces on a diagonal to the ND, and these traces were consistently symmetrical about the ND. Although the current

study did not investigate slip traces on the surface of these particular samples, the evolution of high angle boundaries or dense dislocation walls at ~45° to the compression plane seems to be consistent with the findings of Theyssier *et al.*[73]. Although slip planes do not correspond to the angles of these boundaries, it is likely that slip did occur along or perpendicular to them. It therefore appears a consistent behaviour in deformed single crystals that slip at ~45° to the ND occurs in various orientations when hot deformed in plane strain compression.

8.2.2 Strain Homogeneity

Extensive EBSD scanning of samples hot deformed to a strain of 0.5 showed that over long distances there was a stored energy or strain gradient in the ND (Fig. 8.7). The phenomenon was measured parallel to the ND on both the ND-TD and ND-RD planes. It was evident due to a reduction in the number of well defined sub-boundaries and also a reduction in the magnitude of their misorientations. The effect was observed to become more pronounced after annealing, where regions of highest stored energy were always adjacent to a recrystallised cluster. Traversing along the ND away from the recrystallised region corresponded to a reduction in the stored energy.

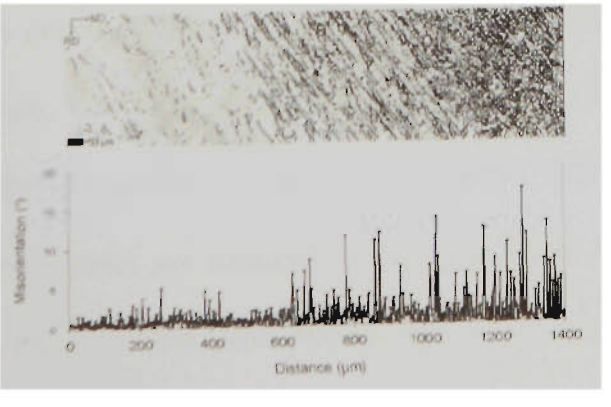

Figure 8.7 EBSD Euler 3 orientation map and misorientation profile for sample deformed to a strain of 0.5 at 300°C.

In some instances, the structure had recovered to an extent that there were no sub-boundaries present in the structure above 2° misorientation. Since the region was so well recovered, the EBSD solution rate in these areas was as high as 97%, and is therefore not considered an aberration of the technique. Figure 8.8 displays the microstructural differences in these regions using ECC. The microstructures were taken at the same magnification, probe current, contrast settings etc., and show that some regions maintain a well defined substructure, whilst others have recovered into a more diffuse structure.

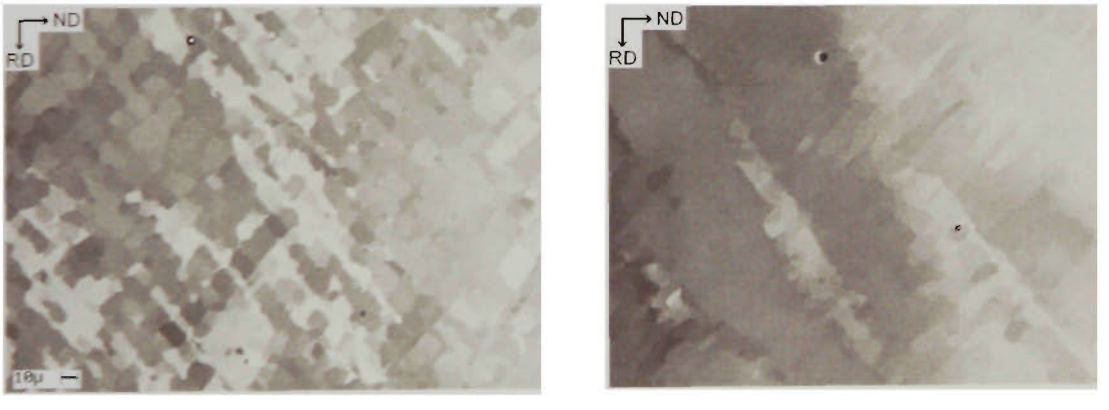

Figure 8.8 SEM ECC micrographs taken at the same magnification and microscope settings, separated by a distance of ~2mm in the ND.

The origin of these strain gradients is thought to be the result of shear banding. When these sheared volumes intersect there is a region of high strain, and between them there is a region of low strain. This is shown schematically in Fig. 8.9. This shear banding behaviour produces the 45° sub-boundaries observed in the ND-RD section (see Fig. 6.5), and these sub-boundaries are arrowed in Fig. 8.9. These boundaries, or dense dislocation walls, correspond to the (100) planes, suggesting deformation has occurred on non-octahedral systems. Since lateral spread is restricted in plane strain compression it seems likely that slip has occurred on the (100) planes in the <001> directions

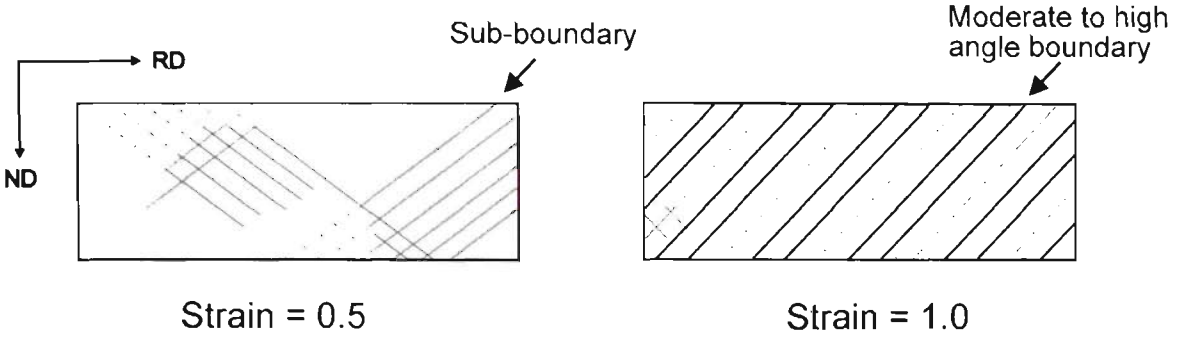

Figure 8.9 Schematic illustration of deformed microstructure at strains of 0.5 and 1.0 in the $(011)[01\bar{1}]$ orientation.

Strain gradients were not detected at high strains, and this may be due to further deformation occurring in those regions that have undergone little deformation previously, ie, in low energy regions. At high strains, one shear direction appears to dominate. Rotation of the crystal may make one system more favourable than another, where as all 4 systems were equally stressed at the beginning of deformation due to sample symmetry.

For clarity, it should be pointed out that the shear bands described here are quite diffuse, they could also be described as a cluster of slipped planes, or a cluster of parallel sub-boundaries. The misorientation of sub-boundaries in these regions gradually decreases away from the band, as was shown in Fig. 8.7. The shear bands found here are not surrounded by a sharp boundary, and are microstructurally different to the non-crystallographic shear bands observed in the Copper orientation[80].

9 Discussion - Annealing of Deformed Single Crystals

The details of the heat treatments used to anneal samples have been described in Tables 5.4 and 6.2 in the Results sections. In general, samples were annealed at 300°C. This is a high temperature treatment for aluminium, but is not so high that recrystallisation is complete within seconds. However, some crystals resisted recrystallisation at 300°C, and certain samples were selected for annealing at 400°C. To compare the recovery and recrystallisation behaviour of samples annealed at different temperatures, where appropriate the annealing time has been temperature compensated using an Arrhenius relationship of the form:

$$t = t_o \exp\left(\frac{-Q}{RT}\right) \tag{9.1}$$

where the normalised time (t) increases exponentially with temperature (T). The activation energy, Q, has been assumed in these calculations to be 147 kJ/mol, which is the activation energy for grain boundary mobility measured by Huang *et al.*[54] on the same alloy system, and is also close to the activation energy of self diffusion in aluminium. Where indicated, kinetic data in this chapter is plotted using temperature compensated time.

9.1 Recovery

The misorientation between subgrains was measured by EBSD. A subgrain boundary has been defined in this study as any boundary with a misorientation between 2° and 12°. Each of these boundaries can be measured, and the average misorientation between subgrains determined. This analysis is most accurate when used for metals deformed at high temperatures that develop well defined substructure.

Low strain microstructures do not produce well defined boundaries, and the misorientation across subgrain boundaries is difficult to measure. An alternate analysis that has been used in low strain samples is the "correlated misorientation" measurement, in which each adjacent pixel in the EBSD orientation map is measured for its misorientation, and the average misorientation determined. Another method to examine the misorientation changes is the "uncorrelated misorientation" which measures the misorientation between randomly chosen points in the EBSD map. Both these techniques require identical mapping parameters, the same grid size and step size, to be comparable. These methods allow measurement to include diffuse boundaries such as those found in the Cube orientation. The change of each of these parameters has been measured with annealing time.

9.1.1 Recovery in the Cube Orientation

Since low strain Cube crystals have little substructure, the correlated and uncorrelated misorientations have been measured for different annealing times and temperatures, and

these are shown graphically in Fig. 9.1. For those samples that contain transition bands, measurements were taken that avoided the large rotations which exist in transition bands.

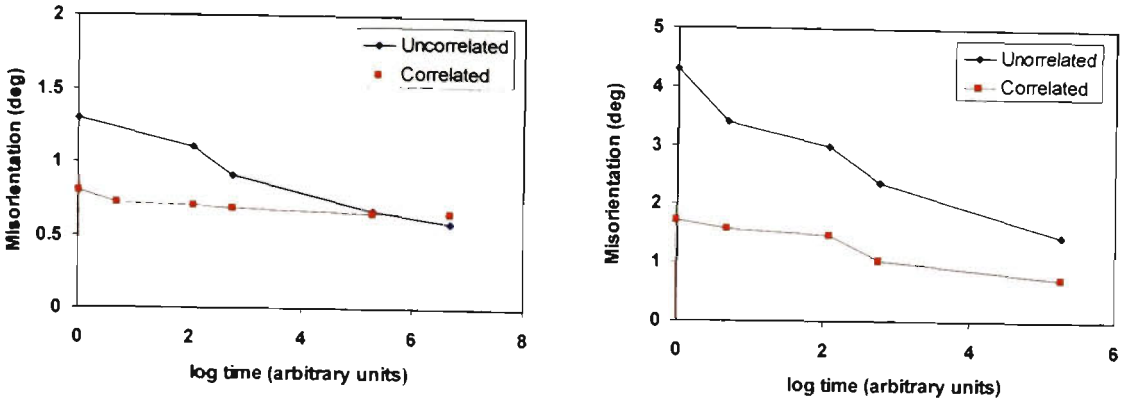

(a) (b)

Figure 9.1 Effect of annealing on the subgrain misorientation of Cube oriented crystals cold deformed to strains of (a) 0.1 and (b) 0.7. Note that the time has been temperature normalised using Equation 9.1 and plotted using arbitrary units.

Analysis of both the correlated and uncorrelated misorientations indicates that the misorientation over small distances drops slightly with annealing, due to the development of a better defined substructure on annealing which produces regions within these cells that are very low in both dislocation density and orientation gradient. A significant drop in uncorrelated misorientations was also found.

The reduction in misorientation with annealing implies that recovery evens out the inconsistencies of the deformed state, and is consistent with the definition of recovery which describes the process as one in which the materials properties are partially returned to their original state[11]. Misorientation profiles for cold deformed samples before and after annealing are shown in Fig. 9.2. It can be seen that the misorientation

changes become less sharp with annealing, reducing the misorientation spread as shown in Fig. 2.2 of the literature review.

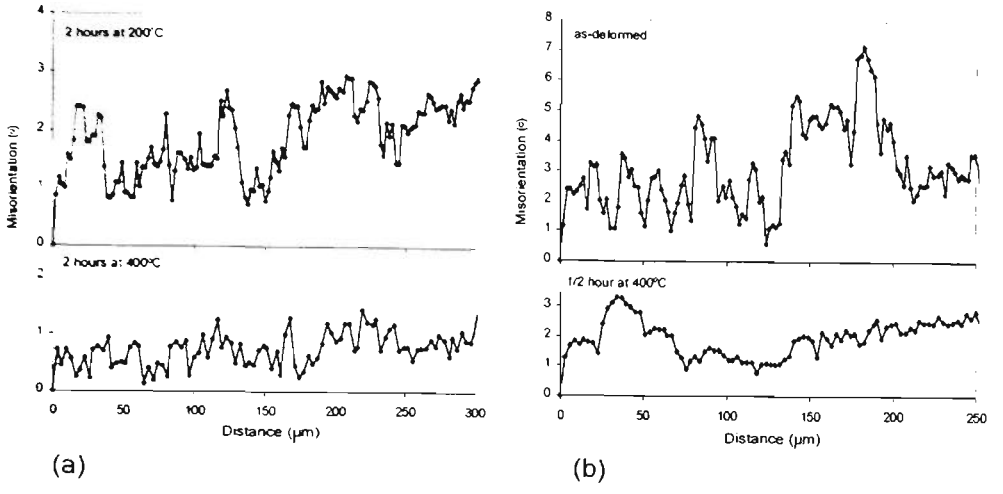

Figure 9.2 Cumulative misorientation profiles for the Cube orientation deformed to strains of (a) 0.1 and (b) 0.7. Heat treatments as shown in the figure.

9.2 Kinetics of Recrystallisation

9.2.1 Kinetics of Recrystallisation for $(011)[01\bar{1}]$ *Orientation*

The kinetics of recrystallisation are shown in Fig. 9.3. At a strain of 0.5, the kinetics of recrystallisation follow the usual rules of faster kinetics after deformation at lower temperatures. After a strain of 1.0, the kinetics of recrystallisation are similar after deformation at 25 and 200°C, but significantly lower after deformation at 300°C.

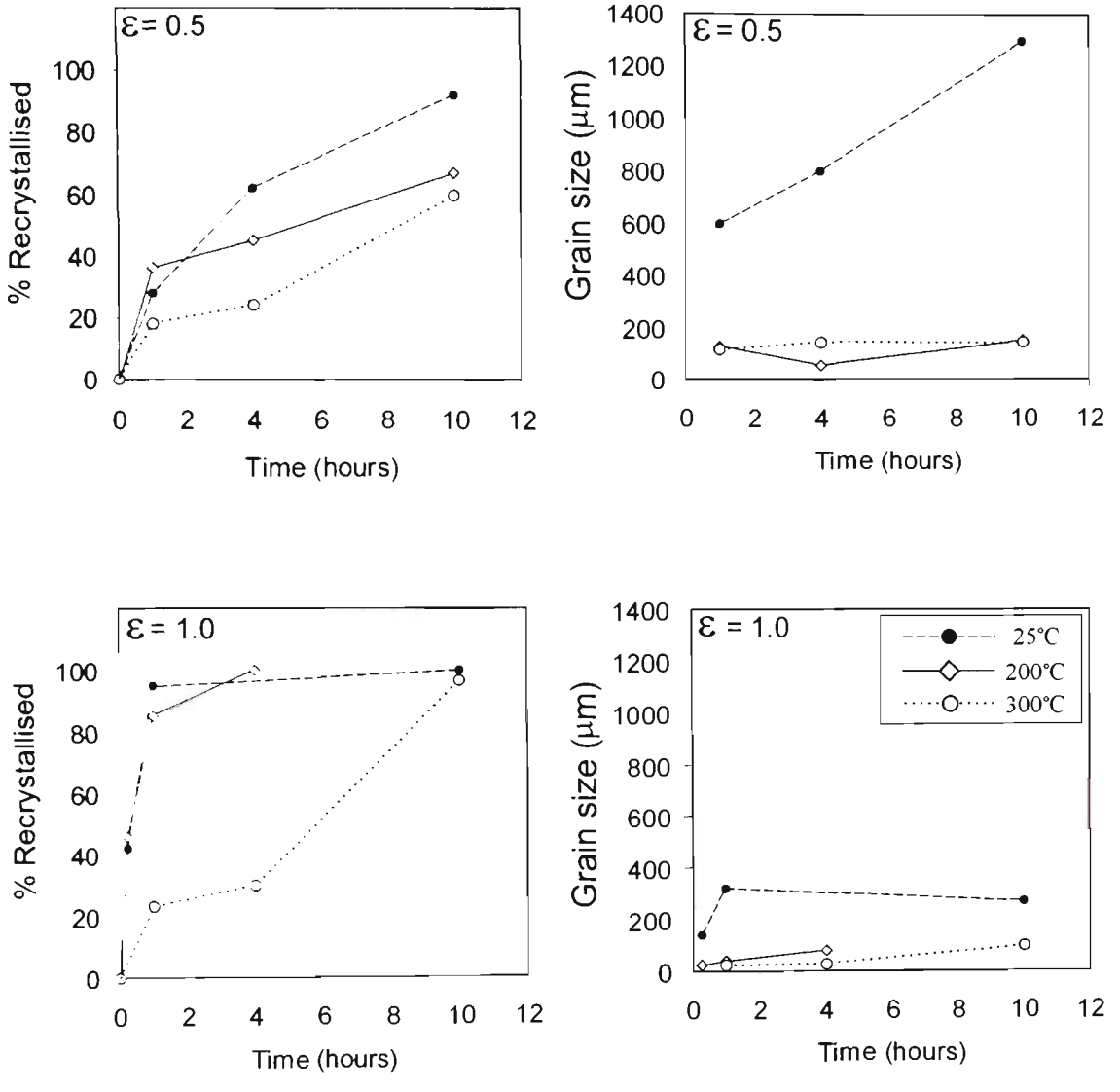

Figure 9.3 Recrystallisation kinetics and grain size for the $(011)[01\bar{1}]$ orientation after deformation to the strains indicated and annealed at 300°C.

Investigation of the recrystallised grain size with annealing shows cold deformed crystals to have much larger grains. The grain sizes in the hot deformed crystals are quite similar, suggesting a similar growth propensity for these samples at strains of both 0.5 and 1.0.

9.2.2 Kinetics of Recrystallisation for the Cube Orientation

The kinetics of recrystallisation for cold deformed Cube crystals over a range of strains is shown in Fig. 9.4. After high strains (ε = 1.2) recrystallisation is complete after 1 hour at 300°C, and exhibits a relatively small grain size, probably due to a large number of nuclei which compete for size. Crystals deformed to lower strains require longer to recrystallise.

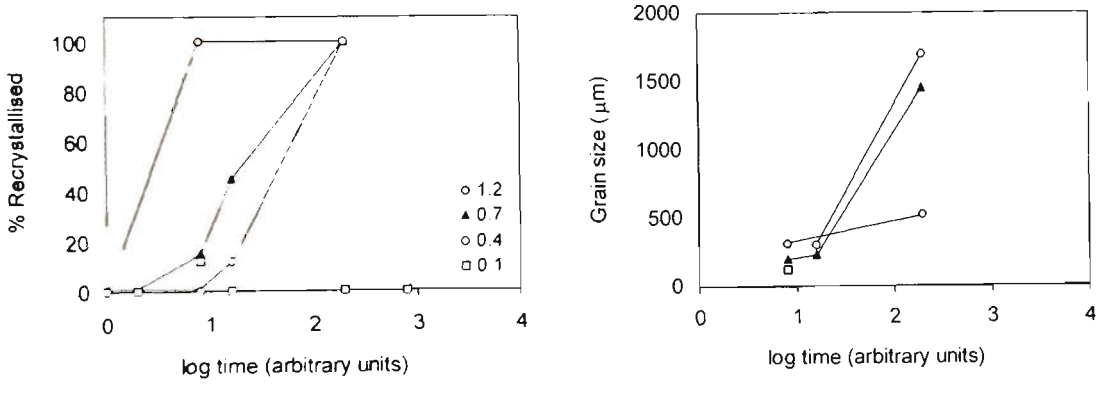

(a) (b)

Figure 9.4 Recrystallisation kinetics for cold deformed Cube crystals for strains of 0.1 to 1.2. Note that the time has been temperature compensated using Equation 9.1.

The recrystallisation kinetics of the hot deformed Cube oriented crystals is complicated by post-deformation recrystallisation. In the Results (section 5.3) it was pointed out that during the quench cycle of between 8 and 12 seconds, a significant amount of recrystallisation occurred in some samples. With the notable exception of the 300°C treatment, the higher the deformation temperature the more recrystallisation occurred during the quench cycle. Although the stored energy after high temperature deformation is lower than after cold deformation, quenching from a much higher temperature allows more recrystallisation to occur. The only significant deviation from this trend was that

the sample deformed at 300°C did not exhibit any recrystallisation. At 200°C the stored energy of deformation may be high enough to cause recrystallisation, but at 300 °C it is not sufficient. Deformation at 400°C provides enough thermal energy to recrystallise, but again is not sufficient at 300°C. The much higher recrystallisation kinetics observed during the quench cycle (compared to post-deformation annealing) are probably the result of metadynamic recrystallisation, in which no incubation period is required. This is exacerbated by the effects of recovery during post-deformation annealing which retard recrystallisation also.

The recrystallisation kinetics for post-deformation annealing of a Cube crystal deformed and annealed at 300°C are shown in Fig. 9.5.

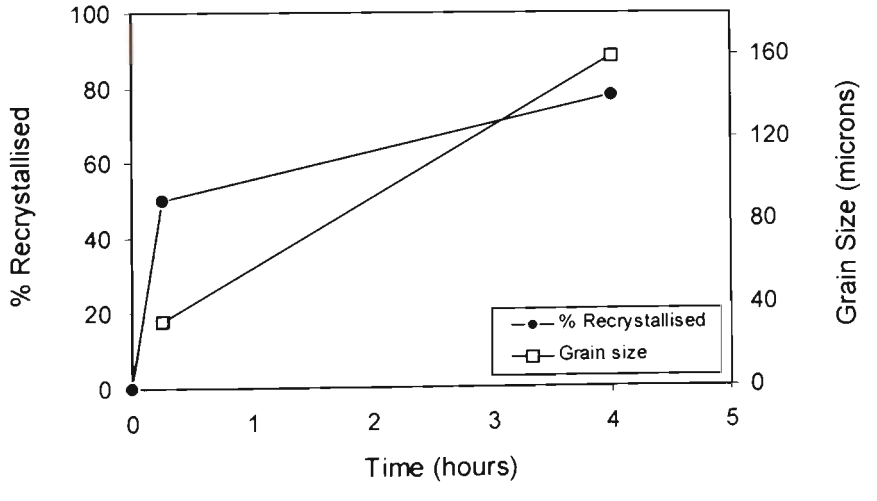

Figure 9.5 Recrystallisation kinetics and grain size measurement for a Cube oriented crystal deformed to a strain of 1.0 and annealed at 300°C.

At high temperatures, the Cube orientation produces a well defined substructure of large equiaxed subgrains. In terms of mobility, this structure is not likely to recrystallise quickly due to the orientation pinning which results from the high temperature microstructural stability. The rapid growth of a subgrain is difficult both due to the low

angle boundaries as well as the low energy of the system imparted by the large subgrain size.

9.3 Recrystallisation Textures

9.3.1 Cold Deformed Crystals

After deformation to a strain of 0.5 and annealing at 300°C of the $(011)[01\bar{1}]$ orientation, the recrystallised grains had a virtually random texture (see Fig. 6.13 of the Results section). Similar to the recrystallisation Cube crystals deformed to high strains, there were only a few grains present, and these rapidly grew very large. After deformation to a strain of 1.0, the largest recrystallised grains in the $(011)[01\bar{1}]$ crystal were also far from the deformation texture, however, colonies of smaller grains with a high preferred orientation were produced, presumably by subgrain growth. These clusters were not centred on the starting orientation, but offset by rotation about the TD corresponding to the periphery of the deformation texture.

In addition to the current work, two other studies have reported on the cold deformation and annealing of the $(011)[01\bar{1}]$ orientation. Akef and Driver[85] reported that cold deforming and annealing of this orientation produces recrystallised grains that differ from the as-deformed state by 15-30° rotations. However, in this case the nuclei are not random, they are contained in a band surrounding the deformation texture but not within it (Fig. 9.6a). A similar recrystallisation behaviour was reported by Blicharski *et al.*[83], who showed the orientation of nuclei to be clustered, and offset from the deformation

texture by a similar deviation. However, the fully recrystallised texture appears to be dominated by only a few grains in this case (Fig. 9.6b).

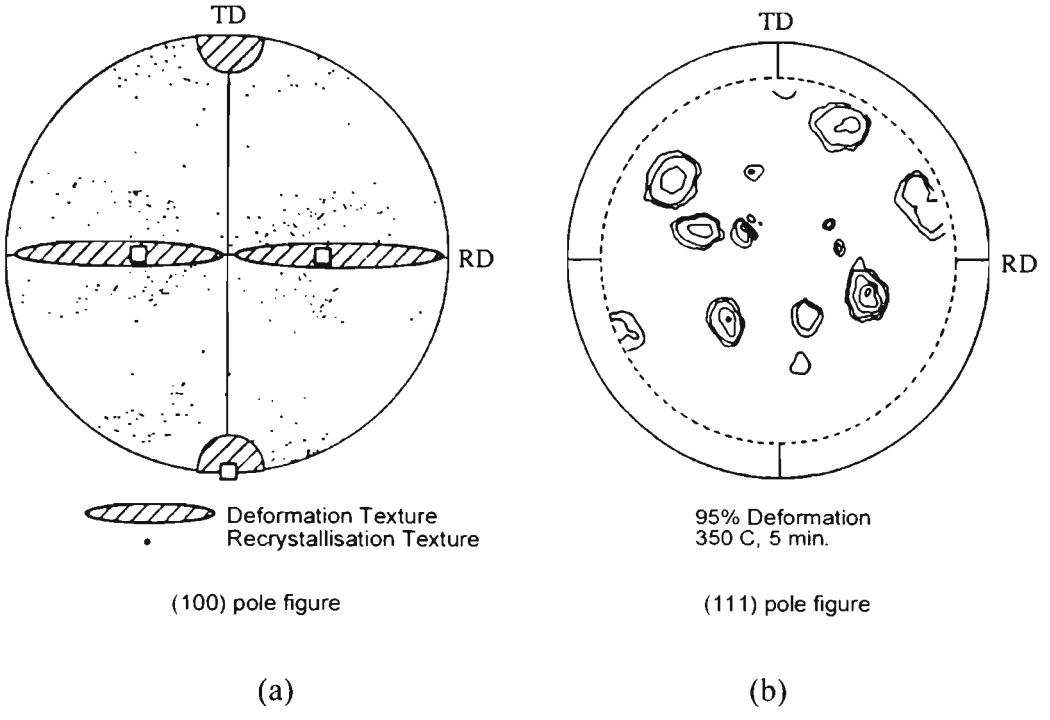

Figure 9.6 Recrystallisation textures of cold deformed and annealed crystals of the (0 1 1)[0 1 $\bar{1}$] orientation (a) Akef and Driver[85] (b) Blicharski *et al.*[83].

Previous experiments on deformed and annealed single crystals of various orientations have reported a number of differing results. Kamijo *et al.*[86, 87, 106] have found that in both Al and Cu crystals of variants of the S orientation, cold rolling and recrystallisation produces the classic Cube recrystallisation texture found in polycrystals. A small number of large grains nucleate from shear bands in the rolling plane and consume the entire sample to produce almost 100% Cube texture in most cases.

Engler and Nes[88] have annealed single phase Al crystals of Goss, Brass, Copper and Cube orientations after cold reductions of 90% (true strains of 2.3). Of these orientations, only the Cube orientation retained some of the deformation texture in the

recrystallised state. The Goss and Brass orientations were found by Engler and Nes to have virtually random recrystallisation textures. In the current study, annealing of *cold deformed* Cube oriented crystals has shown the recrystallisation texture to be virtually random, with a small number of large grains with a large misorientation between them dominating the recrystallisation texture. These findings support the previously published data on the subject.

Cold deformed *Cube crystals* from strains of 0.1 to 1.2 all exhibit an essentially random recrystallisation texture, despite having remarkably different deformation textures. Cube crystals deformed to low strains of <0.4 show very little orientation spread from Cube, but have recrystallised grains with an essentially random texture. Highly deformed crystals, which have a rolling texture spread after deformation, exhibit a similarly random recrystallisation texture. There is no apparent correlation between strain and recrystallisation texture. Similarly, there is no apparent correlation between deformation texture and recrystallisation texture.

The annealing behaviour of deformed Cube oriented crystals is interesting for a number of reasons. Take, for example, a Cube crystal deformed to strain of 0.7. It contains transition bands every 50 μm with rotations of ±25°. If transition band nucleation were to be operating, entire planes of Cube nuclei would sprout, and could grow 50 μm before impinging an adjacent band with the same orientation. This mechanism was not observed to occur, suggesting that the nucleation of Cube oriented grains relies on the presence of other orientations not present in deformed Cube oriented crystals.

The origin of Cube recrystallisation texture in polycrystalline Al has been well studied. Cube nuclei have been shown to grow from regions surrounded by both Copper and S orientation components in highly cold rolled Al and Cu ($\varepsilon > 2.3$) [25, 107]. This is confirmed by deformed S crystals producing a remarkably sharp Cube texture[87], since any Cube volume produced during deformation is surrounded by S components. This requirement may explain to some degree the higher propensity for Cube recrystallisation texture at high cold reductions[52], since the S component is commonly produced after high strain deformation.

Since the Copper and S components are highly misoriented from Cube, it is inevitable that the mobility of the boundary between these components dominates discussion on the origin of Cube texture. However, given this high mobility boundary, no one has satisfactorily described why it is that Cube regions consume S and yet S does not readily consume Cube. One explanation is the size advantage that Cube oriented subgrains have in transition bands compared to the bulk of the grain[36-38]. This is essentially a stored energy difference, one which may further enhance the recrystallisation texture at higher strains, since further deformation may increase the differential between stored energy in regions of different orientation.

To conclude, the reason that deformation and recrystallisation of Cube oriented crystals does not yield a high Cube recrystallisation texture is that Cube nucleation at transition bands requires an adjacent portion of S or Copper orientation which is not present in Cube crystals at the strains studied here.

9.3.2 Hot Deformation

The recrystallisation texture of hot deformed and annealed Cube crystals retains a significant portion of the starting orientation. The sample deformed at 600°C, although fully recrystallised after the quench cycle, has a recrystallisation texture which lies completely within 20° of the starting Cube orientation. After deformation at an intermediate temperature of 300°C, subsequent annealing produces both large grains highly misoriented from Cube, as well as colonies of smaller equiaxed grains that lie within the deformation texture.

Hot deformation imparts the crystal with a number of features. Most importantly, the high temperature eliminates many microstructural inhomogeneities, for example deformation bands in the Cube orientation. It also produces well defined subgrains which have a largely dislocation free interior, and are considerably larger than those formed after cold deformation[11].

Being single crystals, and having eliminated microstructural inhomogeneities, the two most common forms of nucleation, grain boundary nucleation and deformation band nucleation are unable to operate. This slows the recrystallisation kinetics, allows recovery to increase the subgrain size, and promotes nucleation by subgrain growth. Since these subgrains are present in the bulk of the microstructure, their growth allows retention of the as-deformed texture in the recrystallisation texture. Nucleation at grain boundaries or inhomogeneities produces grains that have orientations far from the bulk of the deformation texture.

Comparison of hot and cold deformation behaviour

Cold deformed crystals of $(0\,1\,1)[0\,1\,\bar{1}]$ orientation do not contain intense localised crystal rotations, such as those that occur at transition bands. This allows them to recrystallise by the growth of subgrains that lie at the edge of the main deformation texture.

This behaviour is not exhibited in cold deformed crystals of other orientations, for example, the Cube orientation, for a number of reasons. Regions of intense deformation are more common after cold deformation, and produce volumes of material that are highly misoriented from the sample bulk. These volumes have a high mobility, and exist within regions of high stored energy. In regions such as these, a nucleus once formed grows quickly through the crystal, producing a fully recrystallised microstructure comprising a large grain size and random texture. The nature of these nuclei also prevents the retention of regions of as-deformed state, since they do not suffer orientation pinning, nor do cold deformed samples generally contain regions of low stored energy which prefer recovery to recrystallisation.

Those orientations which are stable, such as Goss, $(0\,1\,1)[0\,1\,\bar{1}]$, and hot deformed Cube recrystallise by growth of subgrains within the bulk, and retain the deformation texture when recrystallised. Unstable orientations such as cold deformed Cube, or those which produce intense sheared volumes when deformed, such as Copper or S, recrystallise to produce annealing textures very different to their deformation textures.

9.4 Recrystallisation Microstructures

Those microstructures formed after deformation and annealing of single crystals with a starting orientation of $(011)[01\bar{1}]$ have been detailed in the Results section. These microstructures show a distinctive periodicity of nucleation, and subsequent retention of banded structures in the fully recrystallised state.

These unique microstructures (see Fig. 6.18 – 6.22) are a result of a periodicity of nucleation, and the origin of this behaviour lies in the as-deformed state. Specifically, shearing on non-octahedral planes which is evident on the ND-RD face produces a matrix of low energy regions separated by high energy sheared planes. The intersection of these sheared planes with one another produce strings of material that are high in energy, and when heated, produce columns of subgrains that are able to nucleate and grow into these high energy regions. This mechanism of periodic nucleation is shown schematically in Fig. 9.7.

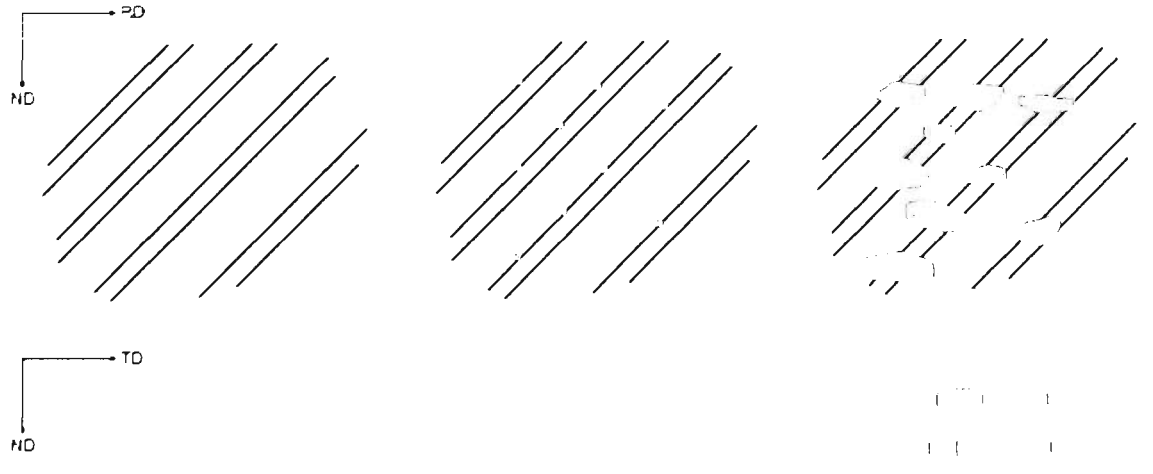

(a) (b) (c)

Figure 9.7 Schematic illustration of (a) as-deformed state created by hot deformation, (b) nucleation, and (c) growth of recrystallised grains.

In Fig. 9.7, subgrains which are situated within the cusp of the intersecting shear bands are able to grow into these high energy regions. A similar nucleation mechanism has been observed by Berger *et al.*[108] after tensile deformation of a <110> oriented Al single crystal. These workers observed a banded deformation structure (similar to a herring-bone structure) which produced a number of stepped high angle boundaries. The ledges or cusps in these boundaries were observed by Berger *et al.* to be exclusive sites for the nucleation of recrystallisation during *in situ* annealing experiments.

The microstructures which support such a hypothesis have been analysed using EBSD, in which it was found that sharp boundaries >10° misorientation are present in the as-deformed state. and examples are shown in Fig. 9.8. In the figure, boundaries greater than 10° misorientation are shown as bold black lines, and those greater than 3° shown as thin black lines.

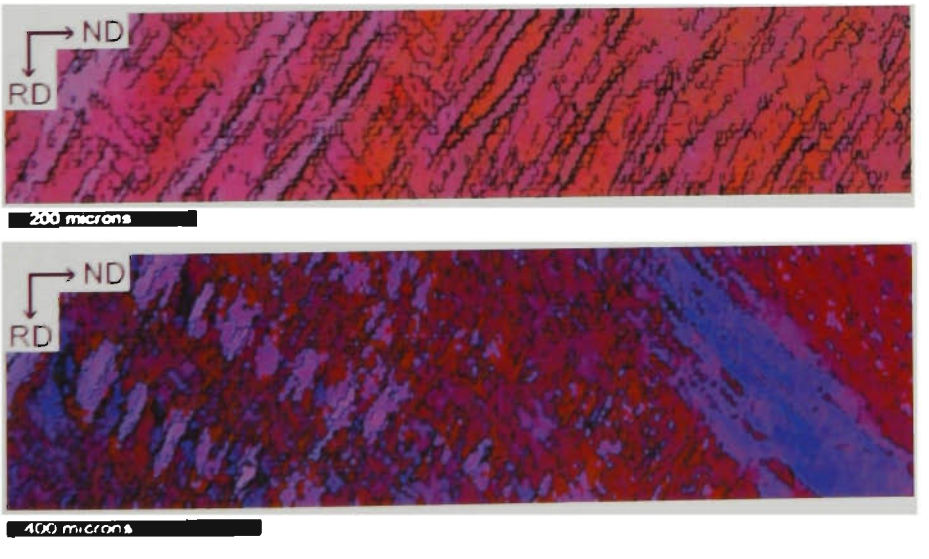

Figure 9.8 EBSD orientation mapping of (a) parallel boundaries on non-octahedral planes, and (b) array of differing orientations, after deformation to 0.5 at 200°C.

An example of recrystallisation along well defined bands is shown in Fig. 9.9. Recrystallisation has occurred in distinct bands, and nucleation is absent between these regions. Above the two recrystallised bands (C and E) there is a region which, through repetition, should be recrystallised also (region A). Instead, this region appears to lack the stored energy for recrystallisation, so only a few large grains grow. Within band A, the subgrain size is clearly larger than within the unrecrystallised zones B and D. The junction between the small subgrains of region B, and large subgrains in region A is as distinctive as the boundary between adjacent bands of subgrains and recrystallised grains (eg. between B and C).

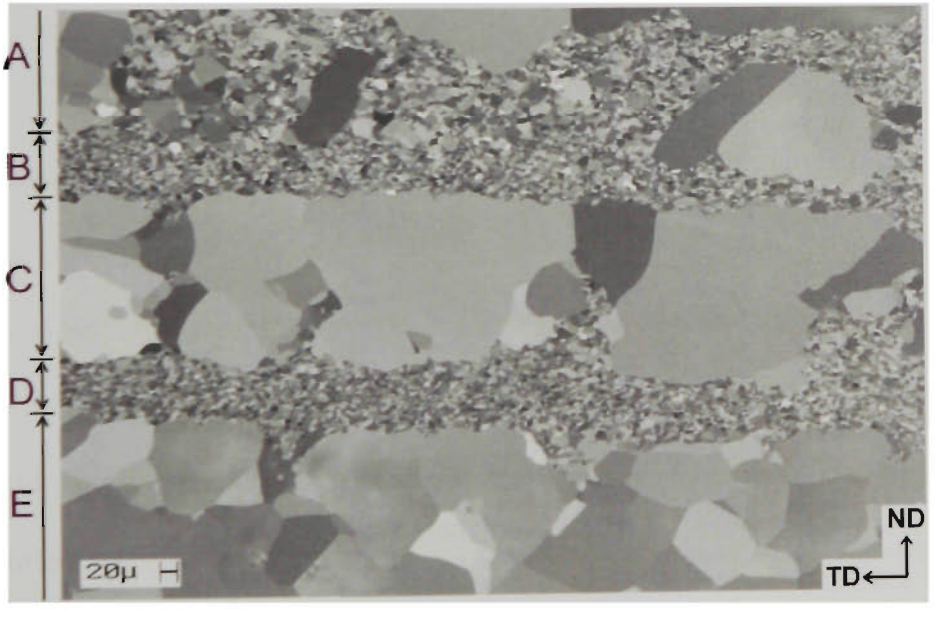

Figure 9.9 SEM micrograph of $(011)[01\bar{1}]$ oriented crystal deformed to a strain of 0.5 at 200°C and annealed for 10hrs at 300°C. See text for details.

In those regions where a fully recrystallised microstructure is realised, the strings of recrystallised grains grow to impingement, and their growth is inhibited significantly enough to retain a banded microstructure in the fully recrystallised state. Where grains are able to grow, there is an anisotropy to their shape, being elongated in the RD, and

this may be explained through the tilt or twist character of the boundary. Tilt boundaries are known to have much higher mobilities than twist boundaries[11], and this has been theorised to cause anisotropy of grain shape in other deformed and annealed single crystals[109]. However, due to the large orientation spread in the deformation and recrystallisation textures this is not considered to be a significant effect, since an orientation relationship between recrystallised grain and deformed matrix is difficult to maintain over large distances. It is most likely that recrystallised grain boundaries have a mixed character of both tilt and twist. These banded microstructures are more likely to be intimately related to the deformation geometry, since the bands are consistently parallel to the TD, and are largely unaffected by the deformation texture or microstructure.

The inhibition of growth in the ND, or stated another way, the grain boundary pinning, may be due to a number of factors. The most obvious type of pinning which may occur in a single phase deformed single crystal is orientation pinning, which is based on the low mobility of boundaries which have a low misorientation[55]. However, bands of recrystallised grains that span many thousands of microns were measured to have very different orientations to their neighbours, up to 30° difference. If one grain was pinned by this orientation effect, a neighbouring recrystallised grain that was differently oriented from the first could not be pinned by the same anomaly. Furthermore, along the length of a large recrystallised grain there may be many hundreds of subgrains which all have different orientations, and this border of differently oriented subgrains is incapable of producing the almost flat boundaries which were observed. Some large recrystallised grains were observed to contain pockets of untransformed material within them, surrounded by the classic 40° <111> rotation. Specifically, the islands of as-deformed

material within the two large grains in Fig. 6.19 of the Results section are surrounded by this high mobility boundary, yet these small rods are not consumed by their surroundings. This confirms that the boundary velocity is not in this case reduced by orientation effects alone. For these reasons, orientation pinning is not thought to be a major contributor to production of these banded microstructures.

It has also been suggested[110] that the velocity of grain growth may be affected by the nature of the dislocation arrangement, that growth parallel to long flat boundaries or dislocation walls is easier than growth across such a boundary. Since subgrains elongate in the rolling direction, grain growth may become retarded in the ND due to this morphological effect. A spherical grain growing among elongated subgrains grows perpendicular to many flat boundaries in the ND, but grows parallel to many triple junctions and grain boundaries in the RD. This may account for the grain shape anisotropy found, specifically the elongation in the RD.

There are other reasons why boundary migration may be halted. For example, when two recrystallised grains meet, their growth is inhibited due to the low energy state associated with recrystallisation, producing a flat boundary. This inhibition of growth is due to stored energy, and may be termed *stored energy pinning*. Mathematically, when a recrystallised grain encounters a low energy region such as another recrystallised grain, the driving pressure P in the mobility equation, (Eq. 2.3 in the Literature Review) v=MP, is significantly reduced. The velocity of the boundary, v, may be reduced to zero if either the mobility or the driving pressure approach zero.

To analyse the stability of these rods of recovered subgrains within a recrystallised grain, a simple energy calculation was carried out. An unrecrystallised cylinder with diameter D_c resists shrinkage due to the increase in grain boundary area per unit volume:

$$E_S = \gamma \frac{dA}{dV} = \frac{2\gamma}{D_c} \qquad (9.1)$$

where dA/dV is the change in grain boundary area per unit volume and γ is the grain boundary energy, taken as 0.324 J/m^2[54].

The stored energy per unit volume (E_D) within the cylinder due to the recovered subgrains with measured diameter L and misorientation θ has been calculated to be[49]:

$$E_D = \frac{2\gamma R}{L} \qquad (9.2)$$

where $R = \frac{\theta}{\theta_m}\left(1 - \ln\frac{\theta}{\theta_m}\right)$ and θ_m is the misorientation at which the boundary becomes high angle (=15°).

Combining Equations 9.1 and 9.2, the cylinder will shrink if:

$$D_c \geq \frac{L}{R} \qquad (9.3)$$

For a sample deformed to a strain of 0.5 at 300°C, and annealed for 4 hours, the subgrain size and misorientation within a column have been measured by EBSD to be 9.8 μm and 4.7° respectively. The driving force ($\Delta E = E_S - E_D$) for growth of a surrounding grain into the cylinder has been estimated for these conditions and is shown as a function of cylinder diameter in Fig. 9.10. When $\Delta E > 0$ the cylinder is stable, and when $\Delta E < 0$ it is energetically favourable for the cylinder to shrink. Figure 9.10 shows the cylinder to be stable below a diameter of 14.5 μm, which is far smaller than the measured diameter of 122 μm. It is unclear if these cylinders will shrink after extended annealing times above those used in the current study. The discrepancy between the measured and calculated values may be the result of inaccurate stored energy calculation, or may be due to kinetic constraints. During recrystallisation the untransformed regions continue to recover, reducing the stored energy within the rods. Once one of these cylinders is formed its consumption is inhibited by this recovery process.

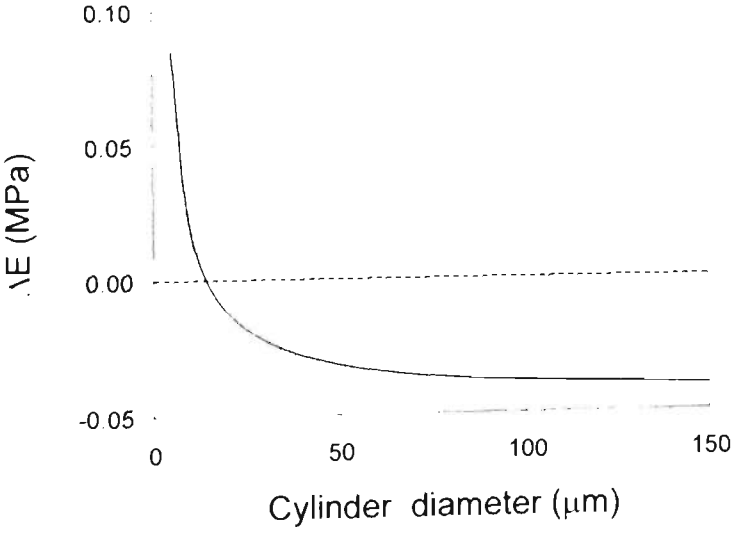

Figure 9.10 Stability of a cylinder of recovered subgrains within a recrystallised matrix calculated using Equations 9.1 and 9.2.

Higher magnification scanning electron microscopy of the remnant cylinders of as-deformed material showed that they were often bordered by subgrains which were larger than those in the centre of the band (Fig. 9.11). EBSD analysis (Fig. 9.12) showed that not only are these bordering subgrains larger, 50% larger after a strain of 0.5, and 58% larger after a strain of 1.0, but they also have higher average misorientations, 38% and 92% respectively. Formation of larger subgrains may have a pinning effect on recrystallised boundaries. These large subgrains are a stable structure, they are surrounded by a moderately high angle boundary and contain a low internal dislocation density. They may act like pinning points on a recrystallising grain boundary, similar to Zener pinning by second phase particles. A pinning contribution such as this may account for the difference between the calculated and observed cylinder radii.

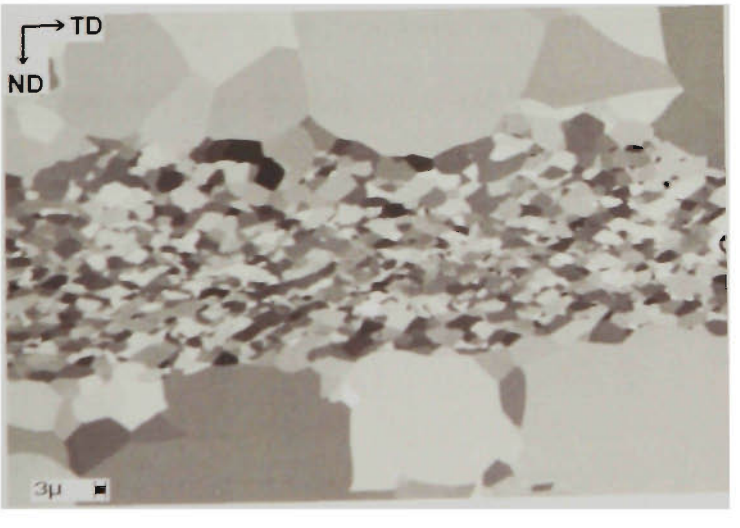

Figure 9.11 SEM micrograph of sample deformed to a strain of 1.0 at 200°C and annealed for 1 hour at 300°C. The unrecrystallised interlayer is a section along the axis of a rod parallel to the TD with an elliptical cross section as shown in Fig. 6.22 of the Results section.

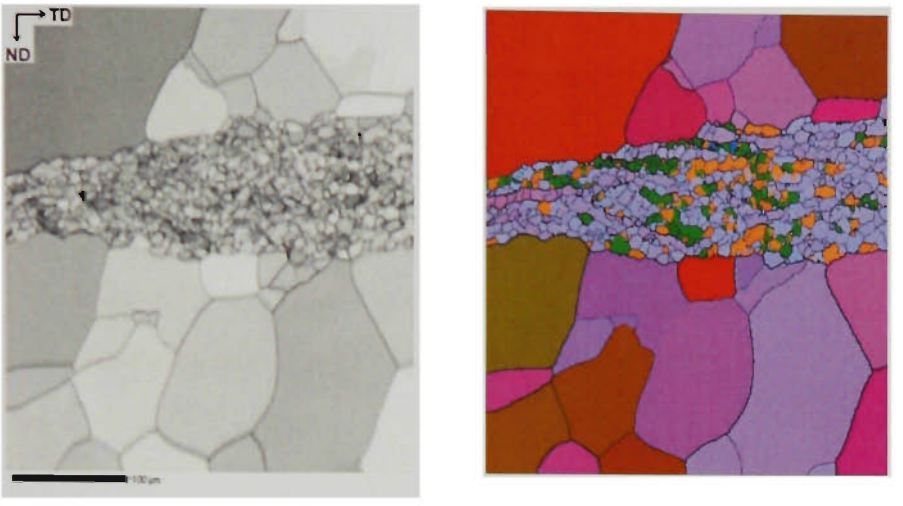

(a) (b)

Figure 9.12 EBSD mapping of the as-deformed material between recrystallised bands shown as (a) band contrast map and (b) all Euler orientation map.

It seems that the abrupt reduction in grain boundary mobility at these banded interfaces is the result of changes in the stored energy of the system. The deformation mechanisms that operate in this orientation are able to produce regions of both high and low stored energy. The intersection of high angle boundaries on non-octahedral planes produces periodic nucleation. Between these planes cylindrical volumes of low stored energy are retained which resist recrystallisation when annealed at 300°C. A schematic illustration of how non-octahedral shearing produces both periodic nucleation of recrystallisation and retention of bands of unrecrystallised material is shown in Fig. 9.13.

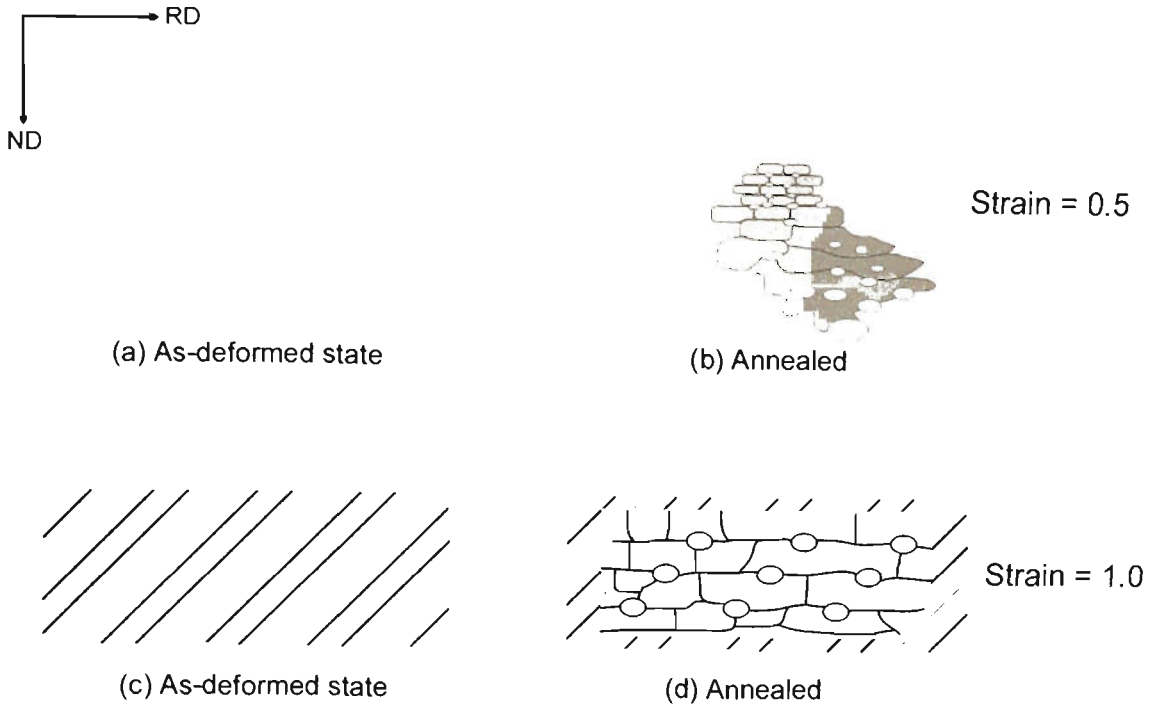

Figure 9.13 (a) Schematic of the as-deformed state and (b) recrystallisation behaviour for $(011)[01\bar{1}]$ oriented crystal deformed to a strain of 0.5. (c) Schematic of the as-deformed state and (d) recrystallisation behaviour for $(011)[01\bar{1}]$ oriented crystal deformed to a strain of 1.0.

Although the structure of the recrystallised grains are of interest here, it is prudent now to discuss the opposite: the morphology of the retained as-deformed structures after extensive annealing. The regions of as-deformed material that remain after annealing are not random. In general, isolated recrystallised grains outside the recrystallised zones were not observed. However, the partially recrystallised regions that lie at the periphery of the recrystallised cluster contain rods of unrecrystallised material which run through many recrystallised grains. One single large grain may be traversed by 10 or more rods of this nature, appearing like "swiss cheese" when sectioned. These rods are regularly spaced, and aligned along the non-octahedral planes identified in the as-deformed state. It is a matter of symmetry that when sectioned in the ND-TD plane these rods line up to produce the microstructures shown in Figs. 6.18-6.22 of the Results section.

After deformation of the $(011)[01\bar{1}]$ orientation at room temperature to a strain of 0.5, annealing produced grains with the characteristic banded structure found after high temperature deformation. However, after a strain of 1.0, these bands were not observed. This may be due to the high stored energy associated with cold rolling. It is possible that this high strain does not allow the development of low energy zones, thus eliminating the banded microstructures formed after different deformation conditions.

10 Discussion - Orientation Effects

At 300°C, the two orientations studied in this work deform quite differently. The Cube orientation spreads slightly about the TD, but does not exhibit extensive deformation banding at this temperature. It is microstructurally quite stable at 300°C. Also, subgrains have not developed sufficiently at this strain (ε=1) to be clearly identifiable using ECC or EBSD techniques (Fig. 10.1). This is consistent with the results of Ferry *et al.*[111] who found that deformation of Cube oriented crystals at 300°C and strain rates of 0.5 and 50 s^{-1} did not produce clearly defined subgrains. It is also consistent with the cold deformation behaviour described in section 5.1, where cold deformation of Cube oriented crystals to high strains did not produce clearly defined subgrains.

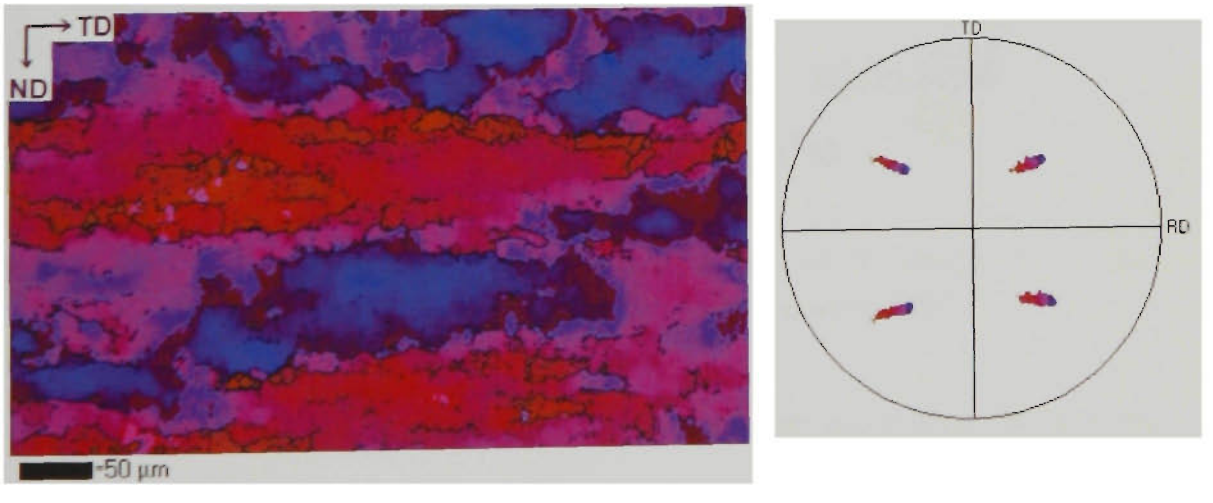

Figure 10.1 Deformation texture and microstructure of a Cube oriented crystal deformed at 300°C to a strain of 1.0 measured using EBSD.

However, deformation of the (011)[01 $\bar{1}$] orientation at 300°C produces a significantly different microstructure. Firstly, the subgrains are well developed and have a high misorientation between them, with an average of 10.8°. The deformation texture is markedly spread about the TD and ND. This corresponds to the formation of alternating

layers of bands that form the herring-bone structure shown in Fig. 6.11 of the Results section. The transition region between bands in the herring-bone structure comprise continuous orientation gradients whose magnitude is much smaller than those formed after cold deformation of the Cube orientation. The subgrains in the $(011)[01\bar{1}]$ orientation are well developed, they are generally elongated in the TD, but may be aligned at an angle to the rolling plane in certain regions (arrowed in Fig. 10.2).

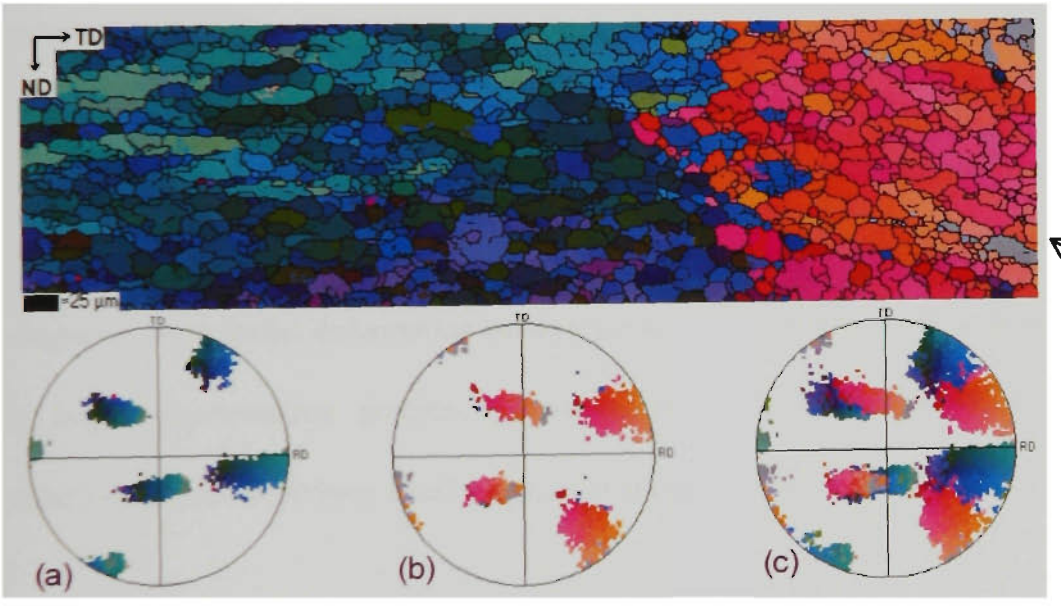

Figure 10.2 Deformation texture and microstructure of a $(011)[01\bar{1}]$ crystal deformed at 300°C to a strain of 1.0 measured using EBSD

The recrystallisation kinetics after deformation at 300°C are much higher in the Cube orientation, probably because they were deformed at a higher strain rate. After 4 hours annealing at 300°C the Cube orientation was 78% recrystallised, but the $(011)[01\bar{1}]$ orientation was only 30% recrystallised. Large clusters of equiaxed grains of a similar size were observed in both samples, and in both cases were ~100 µm in diameter. However, the largest grain measured in the $(011)[01\bar{1}]$ orientation was 400 µm, but only 250 µm in the Cube orientation. It was common to observe a bimodal grain size

distribution in annealed single crystals, with clusters of similarly sized equiaxed grains often bordered by a few much larger grains.

Recrystallisation after deformation at 300°C was inhomogenous in both orientations, both exhibited large areas of as-deformed material remaining after annealing. In recrystallised regions the $(011)[01\bar{1}]$ orientation displayed the unique banded structure that has already been described, but no such regularity of the nucleation process occurred in the Cube orientation.

Cold deformation of the two orientations to a similar strain also showed a remarkably different deformation texture and microstructure. The highly unstable Cube orientation degraded into parallel deformation bands separated by a transition region that contained a large misorientation gradient. However, the $(011)[01\bar{1}]$ orientation remained relatively stable, exhibiting small rotations about the ND and TD (Fig. 10.3).

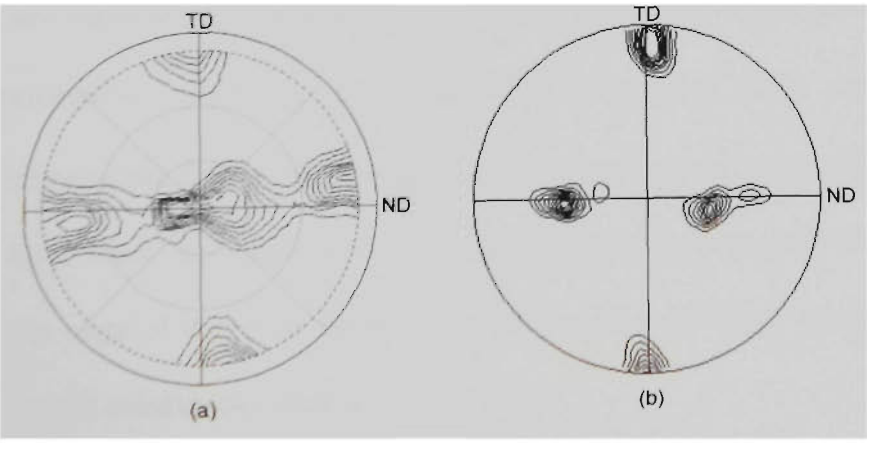

Figure 10.3 (200) pole figures of the deformation texture at a strain of 1.0 of cold deformed crystals of (a) Cube orientation and (b) $(011)[01\bar{1}]$ orientation.

Annealing of cold deformed Cube oriented crystals produced randomly oriented grains of fairly uniform size. The fully recrystallised state contained equiaxed grains, and full recrystallisation occurred after 2 hours at 300°C.

Annealing of cold deformed $(011)[01\bar{1}]$ crystal showed similar recrystallisation kinetics at 300°C, being 95% recrystallised after 1 hour. The recrystallised grains were not uniform in size, and they exhibited an unusual microstructure at grain boundaries (see Fig. 6.14). The recrystallisation texture was clustered in the $(011)[01\bar{1}]$ orientation, and this is probably the source of the unusual grain shapes produced due to grain boundary pinning effects.

The recrystallisation nuclei in cold deformed crystals of the Cube and rotated Cube crystals clearly originate in different microstructural features. The Cube orientation contains regions of intense crystallographic rotation within transition bands. AFM analysis has shown these regions to act like high angle grain boundaries during deformation, and these are the most likely volumes for nucleation of recrystallisation in the Cube orientation. However, the $(011)[01\bar{1}]$ orientation does not contain deformation inhomogeneities. Its deformation texture spread is very small even at large strains. The most likely nucleation process in this orientation is growth of subgrains which lie at the edge of the main deformation texture (Fig. 10.4), as occurs in other stable single crystal orientations such as Goss[77].

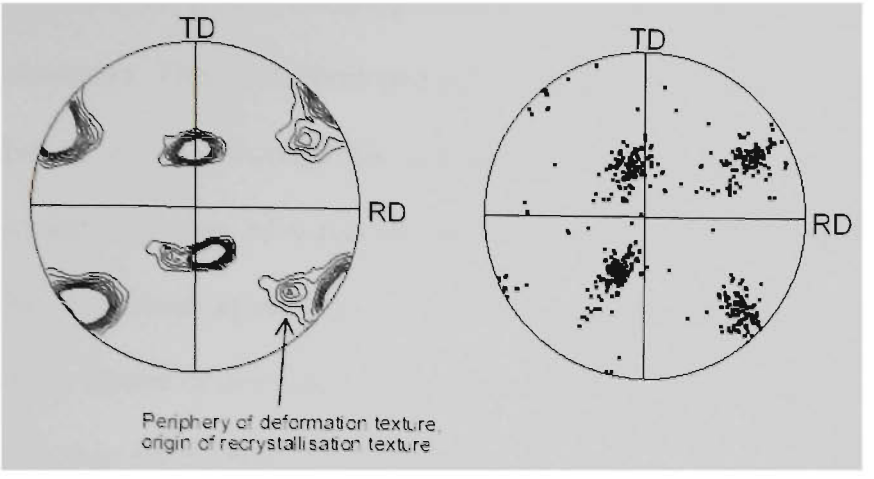

(a) Deformation texture (b) Recrystallisation texture

Figure 10.4 (111) pole figures of (a) the deformation texture of a (011)[01 $\bar{1}$] oriented single crystal cold deformed to a strain of 1.0, and (b) the recrystallisation texture after annealing for 1 hour at 300°C.

The annealing behaviour of deformed single crystals may be summarised as follows: Cold deformation of unstable orientations such as the Cube and Copper[80] orientations produce recrystallisation nuclei far in orientation from the deformation texture, and these originate in regions of high local strain. These nuclei are highly misoriented from the deformation texture, and grow to consume it. The deformation texture does not dominate the recrystallisation texture in this case, and usually results in a large recrystallised grain size. Those cold deformed crystals that are microstructurally stable such as the (011)[01 $\bar{1}$] orientation do not contain significant regions of intense crystal rotation. They produce a clustered recrystallisation texture similar to the deformation texture due to growth of subgrains that lie at the periphery of the main deformation texture.

Hot deformation produces a well defined substructure, and is more homogenous than cold deformation. Thermally activated non-octahedral slip and dynamic recovery

eliminate many microstructural inhomogeneities, for example, the deformation bands in the Cube orientation. This well developed substructure is the origin of recrystallisation in hot deformed crystals through discontinuous growth of selected subgrains. Hot deformed crystals therefore have recrystallisation textures similar to their deformation textures. This behaviour appears to be unaffected by microstructural stability. The recrystallisation texture of deformed single crystals is more sensitive to the temperature of deformation than the microstructural stability.

11 Conclusions

A detailed comparison has been made of the deformation and annealing response of two crystal orientations, the Cube orientation, and a 45° rotated Cube orientation. The major findings are summarised below.

Cold deformation

- When deformed in plane strain compression at room temperature, the Cube orientation is microstructurally stable at true strains below ~0.3.

- At strains above ~0.3 the Cube orientation is not stable, and the development of deformation bands produces a large spread in the deformation texture. These deformation bands lie in the ND-RD plane, and with increasing strain become thinner and rotate further from the starting Cube orientation.

- The inhomogeneity of coarse slip lines in the very early stages of cold deformation of the Cube orientation has been clearly identified by AFM. The coupling of EBSD, SEM and AFM techniques has shown the localised nature of deformation at high strains, particularly in regions of high crystallographic rotation, the transition bands.

- When deformed in plane strain compression at room temperature, the rotated Cube orientation, $(011)[01\bar{1}]$, exhibits a steady state flow stress. This orientation is microstructurally stable on deformation at room temperature, showing very little orientation spread after strains of 0.5 or 1.0.

- The $(011)[01\bar{1}]$ orientation does not produce deformation bands when deformed at room temperature in plane strain compression.

Hot deformation

- The Cube orientation is microstructurally stable at high temperatures, and the prevalence of deformation bands decreased with increasing temperature.

- After high temperature, high strain rate deformation, the Cube orientation showed some recrystallisation in the as-deformed state, probably due to metadynamic recrystallisation.

- The $(011)[01\bar{1}]$ orientation was found to exhibit a lower microstructural stability at higher deformation temperatures. This is the first reported observation of such behaviour in aluminium single crystals. The decreasing microstructural stability at higher deformation temperatures corresponds to the formation of a herring-bone deformation structure for deformation at 300°C to a strain of 1.0.

- Microstructurally, deformation of the $(011)[01\bar{1}]$ orientation produced a well defined substructure, and this structure is aligned to produce high angle boundaries at ~45° to the ND on the ND-RD face.

Cold deformation and annealing

- Annealing of the $(011)[01\bar{1}]$ orientation after room temperature deformation to a strain of 0.5 resulted in a very coarse recrystallised grain structure. These grains had a unique banded appearance and were randomly oriented.

- Annealing of the $(011)[01\bar{1}]$ orientation after cold deformation to a strain of 1.0 resulted in rapid recrystallisation. Clusters of small grains exhibited a preferred orientation, which was offset from the starting orientation, corresponding to the periphery of the deformation texture.

- Annealing of cold deformed Cube oriented crystals produced, at all strains, an essentially random recrystallisation texture.

- Cold deformation of unstable orientations such as the Cube orientation produces, on annealing, nuclei far in orientation from the deformation texture in regions of high local strain. The deformation texture does not dominate the recrystallisation texture in this case, and usually results in a large recrystallised grain size.

- Transition band nucleation was not found to be prevalent in cold deformed Cube crystals, and when observed it was not associated with the nucleation of Cube oriented grains.

- The cold deformation and recrystallisation of Cube oriented crystals does not yield a high Cube recrystallisation texture because Cube nucleation at transition bands

requires an adjacent portion of S or Cu orientation which is not present in deformed Cube crystals at the strains studied here.

Hot deformation and annealing

- The recrystallisation textures of both the Cube orientation and $(011)[01\bar{1}]$ orientation after hot deformation were found to be close to the deformation texture.

- Hot deformation of both Cube and rotated Cube crystals resulted in a relatively homogenous recovered subgrain structure. This well developed substructure is the origin of recrystallisation nuclei in annealed hot deformed crystals through rapid subgrain growth. Hot deformed crystals therefore show a close similarity in their deformation and recrystallisation textures, irrespective of microstructural stability.

- Annealing of hot deformed $(011)[01\bar{1}]$ crystals produced a uniquely banded recrystallised microstructure. Parallel bands of recrystallised grains were separated from one another by cylinders of recovered subgrains whose spacing decreased with increasing strain. These cylinders were arranged regularly into an array when viewed in the ND-RD plane. Fully recrystallised regions retained grains within well-defined bands producing successive grain boundaries parallel to the TD.

- It is proposed that this banded recrystallised microstructure is the result of periodic nucleation of recrystallisation and growth of bands of recrystallised grains with restricted growth in the ND. This inhibition of grain growth is considered to be due

to stored energy differentials resulting from microstructural features in the as-deformed state.

References

1. R.W.K. Honeycombe, *The Plastic Deformation of Metals*, **Edward Arnold** (1984).

2. W. Hosford, *The Mechanics of Crystals and Textured Polycrystals*, **Oxford Science Publications** (1993).

3. C.N. Reid, *Deformation Geometry for Materials Scientists*, **Pergamon Press** (1973).

4. G.I. Taylor, *Journal of the Institute of Metals*, **1**, 307 (1938).

5. J. Bishop and R. Hill, *Philosophical Magazine*, 414 (1951).

6. J. Bishop, *Philosophical Magazine*, 51 (1953).

7. I.L. Dillamore, E. Butler & D. Green, *Metal Science Journal*, 161 (1968).

8. T. Leffers, in *RISØ 2*, eds. N.Hansen, *et al.*, 55 (1981).

9. E. Sachs, *Z. Ver. dt. Ing*, 734 (1928).

10. J. Hirsch and K. Lucke, *Acta Metallurgica*, **11**, 2883 (1988).

11. F.J. Humphreys and M. Hatherley, *Recrystallization and Related Annealing Phenomena*, **Pergamon Press** (1996).

12. U.F. Kocks and G.R. Canova, in *RISØ 2*, eds. N.Hansen, *et al.*, 35 (1981).

13. C. Barrett, *Trans. AIME.*, 296 (1939).

14. G.Y. Chin and B. Wonsiewicz, *Trans. AIME*, 871 (1969).

15. H. Ahlborn, in *Recrystallisation, Grain Growth and Textures*, (1965).

16. C. Barrett and T. Massalski, *Structure of Metals*, **Pergamon** (1980).

17. D. Kuhlmann-Wilsdorf, *Acta Materialia*, **6**, 1697 (1999).

18. C. Maurice and J.H. Driver, *Acta Metallurgica et. Materialia*, **6**, 1653 (1993).

19. R. Smallman and C. Lee, *Materials Science and Engineering*, 97 (1994).

20. C. Lee and B. Duggan, *Acta Metallurgica et Materialia*, **9**, 2691 (1993).

21. S. Kulkarni, E. Starke & D. Kuhlmann-Wilsdorf, *Acta Materialia*, **15**, 5283 (1998).

22. Q. Liu, *et al.*, *Metallurgical and Materials Transactions A*, 2333 (1998).

23. I. Dillamore and H. Katoh, *Metal Science*, 73 (1974).

24. J. Walter and E. Koch, *Acta Metallurgica*, 1059 (1962).

25. J. Hjelen, R. Orsund & E. Nes, *Acta Metallurgica*, **7**, 1377 (1991).

26. A. Ridha and B. Hutchinson, *Acta Metallurgica*, 1929 (1982).

27. A. Malin and M. Hatherly, *Metal Science*, 463 (1979).

28. J. Hirsch, K. Lucke & M. Hatherly, *Acta Metallurgica*, **11**, 2905 (1988).

29. I. Dillamore, J. Roberts & A. Bush, *Metal Science*, 73 (1979).

30. K. Brown, *Journal of the Institute of Metals*, 341 (1973).

31. G.E. Deiter, *Mechanical Metallurgy*, **McGraw Hill** (1988).

32. U. Knocks, C. Tome & H. Wenk, *Texture and Anisotropy*, **Cambridge University Press** (1998).

33. J. Hirsch and K. Lucke, *Acta Metallurgica*, **11**, 2863 (1988).

34. H. Bunge, *Texture Analysis in Materials Science*, **Butterworth &Co** (1982).

35. C. Maurice and J. Driver, *Acta Metallurgica*, **11**, 4627 (1997).

36. H.E. Vatne, T. Furu & E. Nes, *Materials Science and Technology*, 201 (1996).

37. O. Daaland and E. Nes, *Acta Materialia*, **4**, 1413 (1996).

38. H. Vatne, R. Shahani & E. Nes, *Acta Materialia*, **11**, 4447 (1996).

39. Y. Huang, F. Humphreys & M. Ferry, *Acta Materialia*, 2543 (2000).

40. P. Anongba, J. Bonneville & J. Martin, *Acta Metallurgica et Materialia*, **10**, 2907 (1993).

41. R. LeHazif, P. Dorizzi & J. Poirier, *Acta Metallurgica*, 903 (1973).

42. R. LeHazif and J. Poirier, *Acta Metallurgica*, 865 (1975).

43. W. Yeng, *Acta Metallurgica et Materialia*, **6**, 1109 (1990).

44. J. Martin and D. Caillard, *Zeitscrift fur Metallkund*, 867 (1993).

45. P. Cotterill and P. Mould, *Recrystallisation and Grain Growth in Metals*, **Surrey University Press** (1976).

46. E. Nes and J. Saeter, in *RISØ 16*, eds. N. Hansen, *et al.*, (1995).

47. E. Nes, *Acta Metallurgica et Materialia*, **6**, 2189 (1995).

48. F. Humphreys, *Acta Materialia*, **10**, 4231 (1997).

49. Y. Huang and F. Humphreys, *Acta Materialia*, 2017 (2000).

50. R. Cahn, *Recovery and Recrystallisation*, in *Physical Metallurgy*, 3rd Edition, eds. R. Cahn, *et al.*, **Elseiver Science**, 1595 (1983).

51. R. Doherty, *et al.*, *Materials Science and Engineering*, 219 (1997).

52. Doherty, *et al.*, in *RISØ 16*, eds. N. Hansen, *et al.*, 1 (1995).

53. C. Sellars, in *RISØ 7*, eds. N. Hansen, *et al.*, 167 (1986).

54. Y. Huang and F. Humphreys, *Acta Materialia*, **7**, 2259 (1999).

55. D.J. Jensen, in *RISØ 16*, eds. N. Hansen, *et al.*, 119 (1995).

56. Vatne, Saeter & Nes, *Script Materialia*, **7**, 937 (1998).

57. P.A. Beck, P.R. Sperry & H. Hu, *Journal of Applied Physics*, 420 (1950).

58. K. Lucke, R. Rixen & M. Senna, *Acta Metallurgica*, 103 (1976).

59. G. Kohlohoff, *et al.*, in *ICOTOM 6*, eds. S. Nagashima, 489 (1981).

60. R. Doherty, *et al.*, in *ICOTOM 8*, eds. J. Kallend, *et al.*, 563 (1988).

61. W. Hutchinson and H. Ekstrom, *Materials Science and Technology*, 1103 (1990).

62. W. Hutchinson, A. Oscarsson & A. Karlsson, *Materials Science and Technology*, 1118 (1989).

63. J. Hirsch, in *Recrystallization '90*, eds. T. Chandra, 759 (1990).

64. K. Virnich and K. Lucke, in *ICOTOM 5*, eds. G. Gottstein, *et al.*, 397 (1978).

65. A. Dons and E. Nes, *Materials Science and Technology*, 8 (1986).

66. O. Daaland and E. Nes, *Acta Materialia*, **4**, 1389 (1996).

67. A. Akef and J. Driver, *Materials Science and Engineering*, 245 (1991).

68. J. Wert, Q. Liu & N. Hansen, *Acta Materialia*, **6**, 2565 (1997).

69. Q. Liu and N. Hansen, *Proceedings of the Royal Society of London A - Mathematical, Physical & Engineering Sciences*, **1978**, 2555 (1998).

70. J. Driver, D.J. Jensen & N. Hansen, *Acta Metallurgica et Materialia*, **9**, 3105 (1994).

71. A. Godfrey, D.J. Jensen & N. Hansen, *Acta Materialia*, **3**, 835 (1998).

72. K. Lee, Y. Zeng & C. Lee, *Scripta Materialia*, **2**, 197 (1999).

73. M. Theyssier, *et al.*, *Physica Status Solidi*, 367 (1995).

74. M. Wroble, *et al.*, *Zeitschrift fur Metallkund*, **6**, 415 (1994).

75. J. Szymanski and J. Karp, *Archiwum Hutnictwa*, **2**, (1976).

76. A. Mecif, B. Bacroix & P. Franciois, *Acta Materialia*, **1**, 371 (1997).

77. M. Ferry and F. Humphreys, *Acta Materialia*, **4**, 1293 (1996).

78. M. Ferry and F. Humphreys, in *RISØ 16*, eds. N. Hansen, *et al.*, 359 (1995).

79. M. Wroble, S. Dynek & M. Blicharski, *Scripta Materialia*, **3**, 417 (1996).

80. A. Godfrey, D.J. Jensen & N. Hansen, in *RISØ 16*, eds. N. Hansen, *et al.*, 365 (1995).

81. J. Butler and H. Hu, *Materials Science and Engineering*, **A114**, L29 (1989).

82. O. Engler, X. Kong & K. Lucke, *Scripta Materialia*, **5**, 493 (1999).

83. M. Blicharski, J. Liu & H. Hu, *Materials Science Forum*, 109 (1993).

84. C. Verbraak, *Acta Metallurgica*, 580 (1958).

85. A. Akef and J. Driver, *Materials Science Forum*, 103 (1993).

86. T. Kamijo, *et al.*, *Acta Metallurgica et Materialia*, **4**, 693 (1992).

87. T. Kamijo, S. Kataoka & H. Inagaki, *Acta Metallurgica et Materialia*, **6**, 1713 (1993).

88. O. Engler, X. Kong & K. Lucke, *Acta Materialia*, 1701 (2001).

89. F. Basson and J. Driver, *Acta Materialia*, 2101 (2000).

90. A. Brinck, *et al.*, *Materials Science and Engineering A*, 180 (1997).

91. A. Brinck, C. Engelke & H. Neuhauser, *Materials Science and Engineering A*, 37 (1998).

92. C. Coupeau, *Scripta Materialia*, **9**, 945 (1999).

93. A. Brinck, *et al.*, in *Proceedings of the International Seminar on Quantitative Microscopy*, 136 (1995).

94. C. Coupeau, *et al.*, *Philosophical Magazine A*, **6**, 1139 (1997).

95. M. Small and C. Coupeau, *Scripta Materialia*, **10**, 1573 (1995).

96. W. Oele, J. Kerssemakers & J.D. Hosson, *Rev. Sci. Instrum.*, **12**, 4492 (1997).

97. G. Binning and H. Rohrer, *Rev. Mod. Phys.*, 615 (1987).

98. G. Binning, *et al.*, *Europhysics Letters*, 1281 (1987).

99. J. Falk, B. Bay & N. Hansen, in *RISØ 16*, eds. N. Hansen, *et al.*, 351 (1995).

100. M. Ferry and F. Humphreys, *Materials Science Forum*, **1**, 493 (1996).

101. Y. Huang and F. Humphreys, *Acta Materialia*, **11**, 4491 (1997).

102. K. Tanaka, M. Otsuka & H. Yamagata, *Materials Transactions JIM*, **3**, 242 (1999).

103. L. Karjalainen and J. Perttula, *ISIJ International*, **6**, 729 (1996).

104. F. Gao, *et al.*, *Materials Science and Engineering A*, **1-2**, 33 (2000).

105. A. Orlova, *Physica Status Solidi*, 247 (1995).

106. T. Kamijo, *et al.*, *Acta Metallurgica et Materialia*, **8**, 1947 (1991).

107. B. Duggan, *et al.*, *Acta Metallurgica et Materialia*, **6**, 1921 (1993).

108. A. Berger, P. Wilbrandt & P. Haasen, *Acta Metallurgica*, **9**, 1433 (1983).

109. X. Huang, *et al.*, in *First Joint International Conference on Recrystallization and Grain Growth*, eds. G. Gottstein, *et al.*, 773 (2001).

110. A. Godfrey, D.J. Jensen & N. Hansen, *Acta Materialia*, 2429 (2001).

111. M. Ferry, *Personal Communication* (1999).

Appendix A - Gleeble deformation code

```
// F:\QUIKSIM\NIKKI\GOSS_HT.GSL -- hot deformation simulation

// Setup:
// Jaw tempco set to 0.8000um/C, specimen tempco set to 30.0000nm/mm/C
set rampterm to 70000pct
set ramiterm to 0pct
set ramdterm to 2500pct
// stress/strain setup...
set strainmode to 3
set strainsrc to chJaw
set strainX0 to 9.00mm
set strArea to 8.0mm*11.6mm
set planeA to 0.866
set planeB to 0.866
// end of stress/strain setup.
acquire Force Jaw Stroke TC3 wedge
set TC3 to 0C
set tempmode to TC3.control
set h0 to 9.0000mm
set stroke to 0cm
set wedge to 0cm
zero stroke
zero wedge
set pump to on
set heat to on
delay 500msec
set mechanical to on
delay 500msec
set setuprun to on
//set hypress to on
delay 10.0000sec  // <hiPressDelay>
// Zero out stroke under full load...
ramp stroke to -5cm in 2sec
delay 1sec
zero stroke
delay 100msec
set airtc to on
set airram to on
while force>-100.0000kgf  // <heatForce>
   set wedgezero to wedgezero+0.0300mm  // <heatInc>
   delay 100msec
end
ramp stroke to 2.5mm in 1sec
ramp wedge to -1mm in 1sec
// energize load solenoid and grab specimen
set specload to on
```

```
delay 500msec
set specload to off
zero Jaw
set thermal to on

// Pre-deformation:
set lastruntime to systime
sample at 1.0000Hz
ramp wedge to -0.7036mm in 60.0000sec &
ramp TC3 to 300.0000C in 60.0000sec
delay 60.0000sec
zero Jaw
delay 2sec
set enow to 0

// Hit 1:
set stroke to 4.7636mm  // back up=1.6006mm (+) deltaH=3.1630mm
delay 10.0000msec  // <strokeLag>
// finalH=5.8370mm (-) h0=9.0000mm (+) TX=0.2964mm (-) compliance=0.6000mm
{specH=9.0000mm, T=300.0000C}
ramp wedge to -3.4666mm in 100.0000msec  // <wedgePosDuration>
sample at 1.0000Hz
delay 15.0000msec  // <wedgeSettle>
sample at 50.0000Hz
delay 15.0000msec  // <wedgeSettle>
ramp stroke to 3.1630mm in 20.5367sec
ramp TC3 to 300.0000C in 50000.0000msec &
ramp stroke to 2.9702mm in 2500.0000msec &
ramp stroke to 2.7816mm in 2500.0000msec &
ramp stroke to 2.5970mm in 2500.0000msec &
ramp stroke to 2.4163mm in 2500.0000msec &
ramp stroke to 2.2396mm in 2500.0000msec &
ramp stroke to 2.0666mm in 2500.0000msec &
ramp stroke to 1.8973mm in 2500.0000msec &
ramp stroke to 1.7317mm in 2500.0000msec &
ramp stroke to 1.5696mm in 2500.0000msec &
ramp stroke to 1.4109mm in 2500.0000msec &
ramp stroke to 1.2557mm in 2500.0000msec &
ramp stroke to 1.1038mm in 2500.0000msec &
ramp stroke to 0.9552mm in 2500.0000msec &
ramp stroke to 0.8097mm in 2500.0000msec &
ramp stroke to 0.6673mm in 2500.0000msec &
ramp stroke to 0.5280mm in 2500.0000msec &
ramp stroke to 0.3917mm in 2500.0000msec &
ramp stroke to 0.2583mm in 2500.0000msec &
ramp stroke to 0.1277mm in 2500.0000msec &
ramp stroke to 0mm in 2500.0000msec &
ramp stroke to -0.0010mm in 20.0000msec  // <maxOverprogramTime>
```

```
// Post-deformation:
ramp stroke to 12.0000mm in 100msec
ramp wedge to -5.1630mm in 300msec
sample at 1.0000Hz
set thermal to off
set quench1 to on
set quench2 to on
delay 30sec
set quench1 to off
set quench2 to off
// Shut down...
//set thermal to off
set tc1 to 0C
set setuprun to off
//set hypress to off
set mechanical to off
delay 2sec
set pump to off
set heat to off
set temptrim to 0C
delay 2sec
set stroke to 0cm
set wedge to 0mm
set wedgezero to wedgezero-1mm
```

Appendix B - Slip statistics calculation

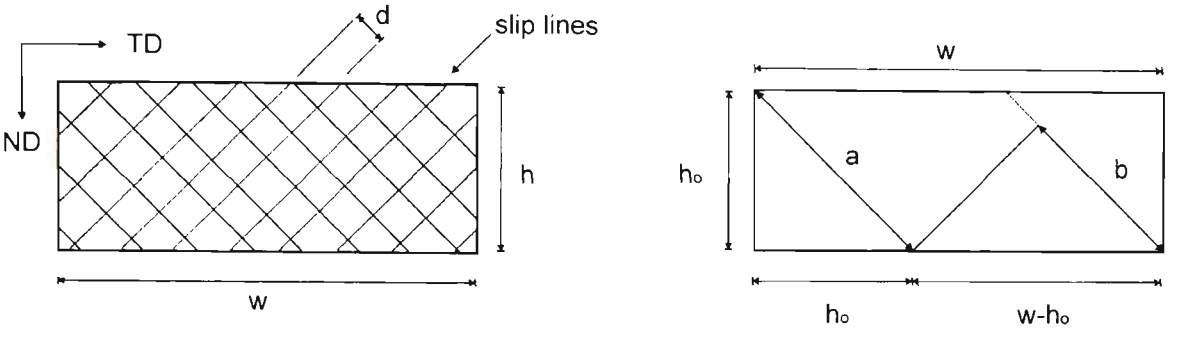

d = perpendicular slip line spacing

w = sample width

h_o = initial sample height

h_f = final sample height

r = total slip step height / total slip spacing

H = sample elongation in rolling direction due to measured slip lines

ε_{slip} = strain induced by measured slip line height and spacing

s = slip height

$$a = \sqrt{2}h_o, \qquad b = \frac{(w - h_o)}{\sqrt{2}}$$

$$\text{Number of slip steps} = n = \frac{a+b}{\bar{d}} = \frac{\left(\sqrt{2}h_o\right)+\left(w - h_o/\sqrt{2}\right)}{\bar{d}} = \frac{w + h_o}{\sqrt{2}\bar{d}}$$

$$\text{Average slip height per } \mu m = r_x = \frac{\Sigma s_x}{\Sigma d_x}$$

$$H_{Total} = 2n \times \left(r_{45} + r_{45}\right) = \frac{\sqrt{2}(w + h_o)(r_{45} + r_{45})}{\bar{d}}$$

$$\varepsilon_{slip} = \frac{\Delta h}{h_o} = \frac{H_{Total}}{h_f}$$

Appendix C - Flow curves for deformed Cube oriented crystals

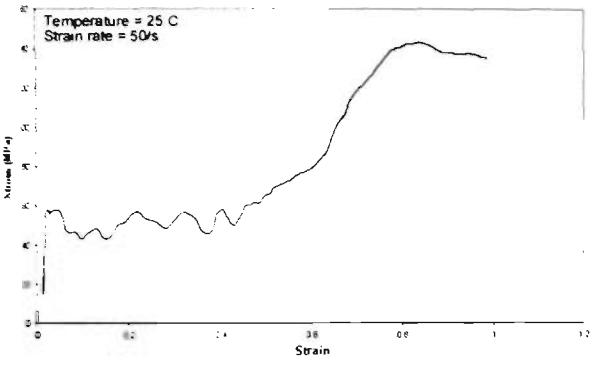

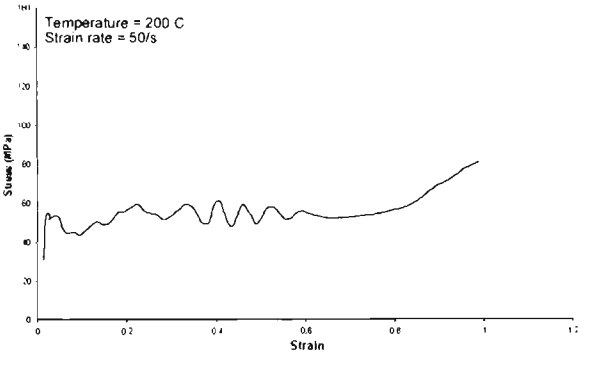

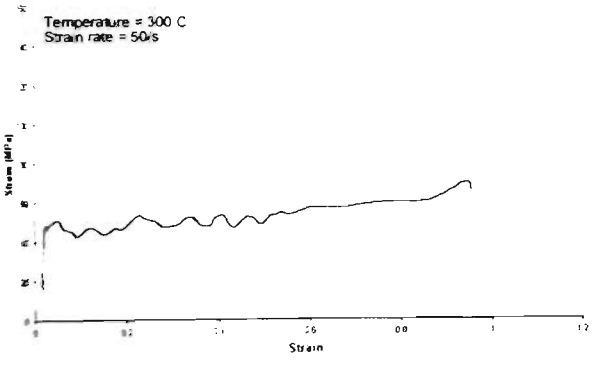

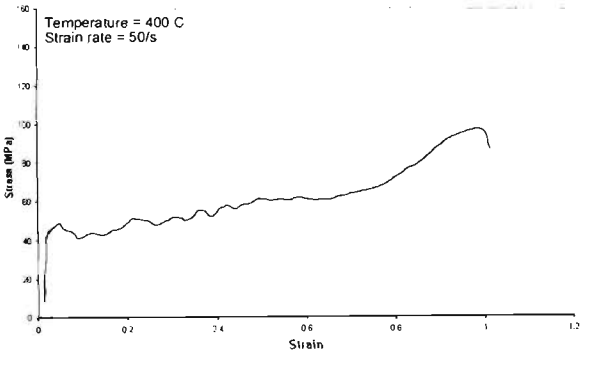

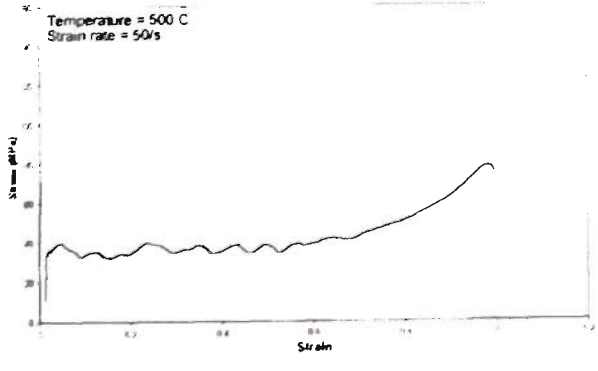

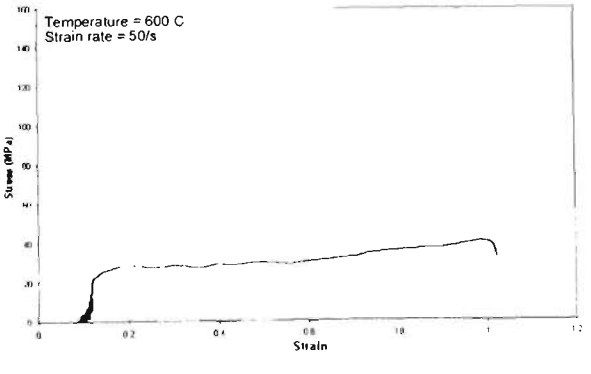

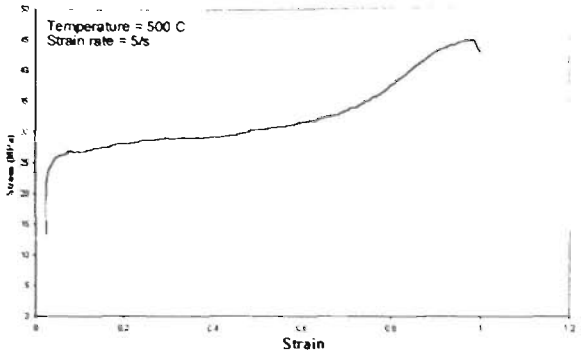
Temperature = 500 C
Strain rate = 5/s
Strain

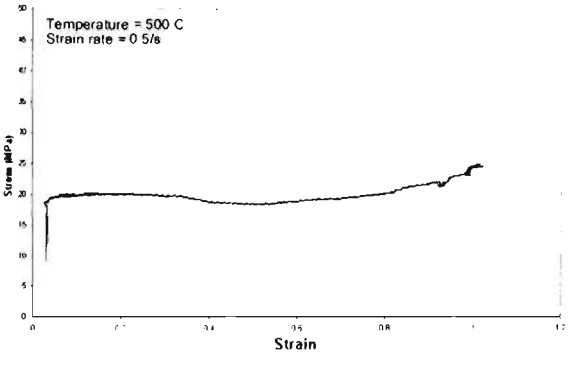
Temperature = 500 C
Strain rate = 0 5/s
Strain

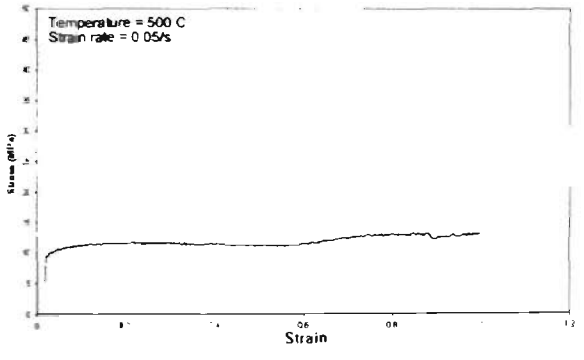
Temperature = 500 C
Strain rate = 0 05/s
Strain

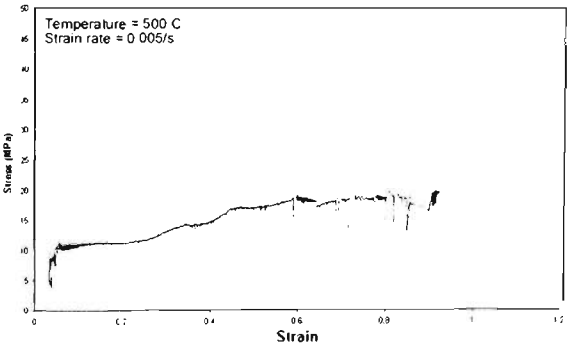
Temperature = 500 C
Strain rate = 0 005/s
Strain

Appendix D - Flow curves for deformed $(011)[01\bar{1}]$ oriented crystals

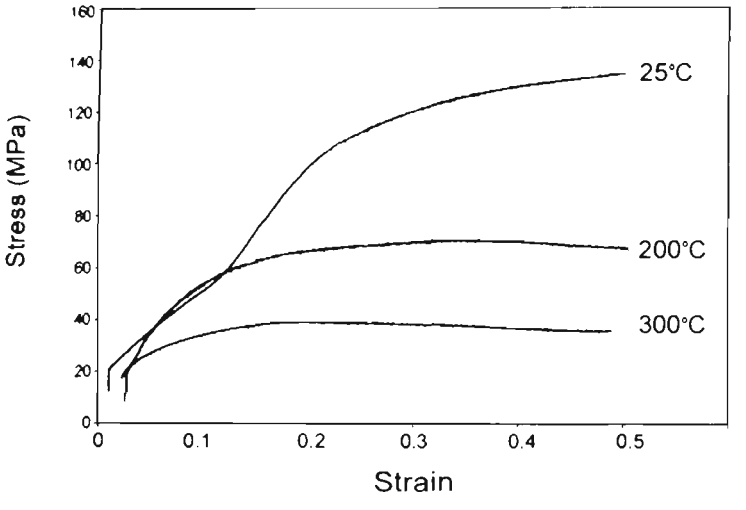

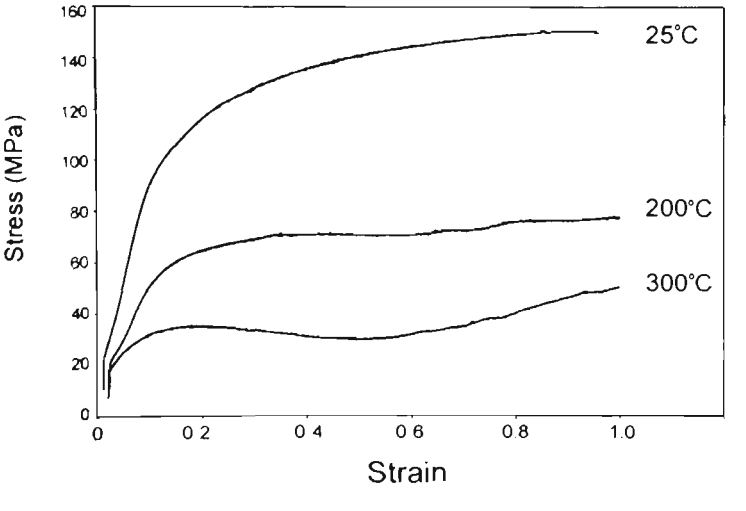

List of Publications

1. N. Stanford and M. Ferry, "Particle Stimulated Nucleation Following Deformation at High Strain Rate and Temperature", in *Recrystallization '99*, eds. T. Sakai and H.G. Suzuki, JIM, 179 (1999).

2. N. Stanford and M. Ferry, "Critical Criterion for Particle Stimulated Nucleation Following Hot Deformation Of An Al-Si Alloy", in *RISØ 21*, eds. N. Hansen *et al.*, 581 (2000).

3. N. Stanford and M. Ferry, "Observations using Atomic Force Microscopy of Surface-Relief Associated with Deformation in Cube-Oriented Single Crystals", *Scripta Materialia*, **44**, 941 (2000).

4. N. Stanford, D. Dunne and M. Ferry, "Periodic Nucleation of Recrystallisation in Deformed and Annealed Al Single Crystals", in *The First Joint International Conference on Recrystallization and Grain Growth*, eds. G. Gottstein and D.A. Molodov, 861 (2001).

5. N. Stanford, D. Dunne and M. Ferry, "Deformation and Annealing of (011)[01$\bar{1}$] Oriented Al Single Crystals", submitted to *Acta Materialia*.

6. N. Stanford, D. Dunne and M. Ferry, "Effect of Microstructural Stability on Recrystallisation Textures in Deformed Al Single Crystals", submitted to *Materials Science and Engineering A*.